



HAL
open science

Modelling of spintronic devices: from basic operation mechanisms toward optimization

Liliana D. Buda-Prejbeanu

► **To cite this version:**

Liliana D. Buda-Prejbeanu. Modelling of spintronic devices: from basic operation mechanisms toward optimization . Physique [physics]. Communauté Université Grenoble Alpes, 2017. tel-01677475

HAL Id: tel-01677475

<https://cea.hal.science/tel-01677475v1>

Submitted on 8 Jan 2018

HAL is a multi-disciplinary open access archive for the deposit and dissemination of scientific research documents, whether they are published or not. The documents may come from teaching and research institutions in France or abroad, or from public or private research centers.

L'archive ouverte pluridisciplinaire **HAL**, est destinée au dépôt et à la diffusion de documents scientifiques de niveau recherche, publiés ou non, émanant des établissements d'enseignement et de recherche français ou étrangers, des laboratoires publics ou privés.

MEMOIRE

Pour obtenir le diplôme d'

HABILITATION à DIRIGER des RECHERCHES

Spécialité : **Physique**

Arrêté ministériel du 23 novembre 1988

Présenté par

Liliana D. BUDA-PREJBEANU

préparée au sein du **Laboratoire SPINTEC UMR 8191**
(CEA/CNRS/Univ. Grenoble Alpes) au **CEA-Grenoble / INAC**,
et de l'**Ecole Doctorale de Physique de Grenoble**

Modelling of spintronic devices: from basic operation mechanisms toward optimization

Mémoire soutenu publiquement le **6 octobre 2017**,
devant le jury composé de :

Mr. Vincent CROS

Directeur de Recherche – UMR CNRS/Thales, Rapporteur

Mr. Michel HEHN

Professeur - Université de Lorraine / IJL, Rapporteur

Mr. Nicolas VUKADINOVIC

Ingénieur à Dassault Aviation, Rapporteur

Mr. Mairbeck CHSHIEV

Professeur - UGA / Ecole Doctorale de Physique, Examineur

Mr. Dafiné RAVELOSONA

Directeur de Recherche – CNRS / IEF, Examineur

Mme. Ursula EBELS

Ingénieure-chercheure - CEA/INAC, Invitée

Mr. Bernard DIENY

Ingénieur-chercheur – CEA /INAC, Invité



Contents

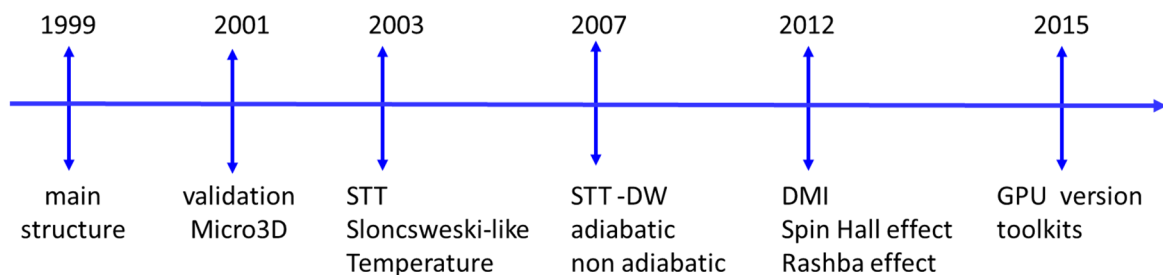
Introduction.....	4
Chapter I: Models overview and implementation.....	6
1.1 Gibbs free energy.....	7
1.2 Magnetic stable state and equilibrium equations.....	11
1.3 Equations of magnetization motion.....	12
1.4 Length scales in micromagnetism.....	13
1.5 Modification related to spin polarized current.....	13
1.6 Thermal fluctuations.....	14
1.7 Numerical micromagnetism.....	15
Chapter II: Magnetic domain walls.....	17
2.1 Domain wall in thin films.....	17
2.2 Domain wall motion assisted by spin transfer torque.....	19
2.3 Chiral magnetic domain wall	22
Chapter III: Spin-torque nano-oscillators.....	29
3.1 STNO with perpendicular polarizer	31
3.2 STNO with planar polarizer	34
3.3 Synchronization of STNO with planar polarizer	37
3.4 Modulation of STNO with planar polarizer	43
3.4.1 Modulation under current.....	43
3.4.2 Modulation under field.....	45
3.5. Coupling phenomena in STNO.....	48
3.5.1 Influence of interlayer coupling on the spin-torque-driven excitations.....	48
3.5.2 Non-linear auto-oscillator model for coupled layers	49
Chapter IV: Magnetic random access memories	52
4.1 Planar spin transfer torque MRAMs	53
4.2 Precessional switching for MRAMs.....	55
4.3 Perpendicular spin transfer torque MRAMs	57
4.4 Spin-orbit torque MRAMs	61
Chapter V: Prospective activities.....	67
5.1 Magnetic random access memories: push further the limits.....	67
5.2 Exploring new STNO concepts.....	70
5.3 STNO for intra- and inter-chip communication.....	70
5.4 Multifunctional standardized stack.....	72
5.5 Memristive magnetic memories for spintronic synapses.....	73
5.6 Modelling tools	74
References.....	76

Introduction

This document is meant to be an overview of my research activity dedicated to the magnetization dynamics of ferromagnetic systems commonly called *micromagnetic modelling*. My initiation to the micromagnetism have begun with the PhD period in January 1999. I had spent three years developing a micromagnetic code Micro3D (single processor version and MPI version). It was really the beginning of numerical micromagnetism, at that time, only few codes were available in the world most of them homemade and without free access. The Micro3D solver was benchmarked successfully against the standard problems proposed at that time by the micromagnetic community [μ MAG]. The numerical schema implemented proved to be accurate, robust and flexible. The code was used for several static studies for 2D and 3D systems. The topics addressed by the modelling were inspired by the experimental studies carried on by my colleagues at IPCMS at Strasbourg or collaborators such as LPN or Siemens-Erlangen. Three topics have been addressed depending on the shape of the systems:

- 1) periodic stripe structures in Co continuous thin films with perpendicular magnetocrystalline anisotropy [Ebels2001], domain wall structure in epitaxial Co layers with in-plane uniaxial anisotropy [Prejbeanu2000].
- 2) magnetic stable states in circular dots and rings [Li2001, Buda2002, Natali2002, Ebels2003]
- 3) domain wall structures in rectangular cross-section nanowires with magnetocrystalline anisotropy parallel or perpendicular to the axis of the wire [Prejbeanu2002].

In February 2002, I joined Spintec from the very beginning as a post-doc working on the modelling of multitrack magnetoresistive reading-heads in collaboration with J.Ch. Toussaint from Institute Néel in the framework of the PhD thesis of Ioana Firastrau [FirastrauPhD]. This was my first contact with the spintronic world though the magnetic field sensors. My activity turned towards the manipulation of the magnetization by the spin transfer torque as shown on the evolution chart below listing the stages of evolution of the Micro3D micromagnetic solver.



Progressively different terms were phenomenologically included in the Landau-Lifshitz-Gilbert equation in the Micro3D solver following very closely the trends from the most recent publications. It was thus possible to study the impact of the spin transfer torques (adiabatic, non-adiabatic) on the depinning and propagation of magnetic domain walls in nano-stripes perpendicularly magnetized [Burrows2010, Garcia2010, Mihai2011]. The interface related phenomena such as Rashba effect was addressed looking for the mechanism responsible of very large magnetic domain wall velocities [Moore2011]. This topic evolved very fast with the introduction of spin-orbit torques and chiral exchange (Dzyaloshinskii-Moriya interaction, structural inversion asymmetry) allowing to enlighten plenty of phenomena in HM/FM/Ox (heavy metal/ ferromagnet / oxide) trilayer structures [Bouille2013, Pizzini2014, Safer2015].

Simultaneously, macrospin based solvers were implemented for one isolated layer or several layers including thermal fluctuations and multiples couplings between layers. The

strength of the macrospin approach consists in providing rapidly results but only applicable for some particular conditions. Cross-checking between micromagnetism and macrospin allows to set the precise limit of the validity of the macrospin approximation [Houssameddine2007, Firastrau2008]. The macrospin tools were extensively applied to study the spin-torque transfer nano-oscillators (STNO), this activity being coordinated at Spintec by Ursula Ebels in the framework of several French and European grants. The extraction of the linewidth corresponding to a steady-state or the noise analyses requests long time traces (few tens of μs), in these conditions even the macrospin simulations start to be very time consuming. One alternative for the numerical studies is the development of simplified analytical models based on spin-waves theory (*c*-model [Slavin2009]) which allow to preserve the main physical phenomena and provide a straightforward interpretation of the observed behavior. For in-plane magnetized layer, the *c*-model was adapted for analyzing the synchronization of a STNO by an RF current [DieudonnéPhD]. This extended model was successfully applied also for the modulation of the STNO by an externally applied RF magnetic field [Purbawati2016]. The *c*-model was further extended to two layers coupled by RKKY interaction and by mutual spin transfer torque allowing to identify the main reason behind the unusual blueshift behavior observed experimentally in such STT oscillators [Romera2016].

The concepts developed for STNO stand also for the magnetic random access memories (MRAM). The focus is in that case on stabilizing at least two well identified stable states at rest and being able to commute between them fast, deterministic and with low power consumption. The precessional MRAM study was part of Adrien Vaysset's PhD thesis initiated in collaboration with Bernard Dieny. The micromagnetic simulations were supporting the experimental observations and confirmed that avoiding the dipolar coupling is reducing the magnetization switching stochasticity and the magnetization reversal is occurring in sub-ns regime [Vaysset2011]. The structural inversion asymmetry (SIA) offers a promising opportunity to build memories based on SOT in a three terminals geometry of interested for cache memories. In collaboration with the spin-orbitronics team coordinated by Gilles Gaudin. Modelling of such cell was performed showing thus the magnetization reversal is driven by deterministic DW nucleation even for pulses of 200ps [Mikuszeit2015]. The macrospin tools served also as base to the implementation of compact model for Cadence tools for the design of SOT-MRAM [Jabeur2014].

The modelling at SPINTEC is a transverse activity supporting the experimental investigations, helping to find new routes to explore in developing/optimizing devices and concepts, understanding the measurements. My collaborators provide plenty of challenges and open questions requesting evolution of the solvers, implementation of new techniques, and development of models. Running micromagnetic simulations is like performing experiments: the interpretation of the results need more than one nice picture or animation. The results must be checked and rechecked, looking for well-founded arguments to be sure at the end that the predictions are faithful. My research activity looks like a puzzle, you need many individual pieces to build at the end a realistic frame; sometimes a piece is missing but inspired by the others, the interconnections are activated and the concrete scenario is finally written. My final purpose is not to have the most sophisticated software but to have one robust, flexible and used it to explore new paths, looking for practical solutions by transposing ideas from one topic to another.

A synthesis over my activity will be provided starting with an overview of the models and their implantation in the chapter 1. The static and dynamic studies carried on the magnetic domain walls are presented in the chapter 2. The work done for the spin-torque nano-oscillators (STNO) is reported in chapter 3. The writing of a memory cell by spin-transfer torque (STT) and spin-orbit torque (SOT) are summarized in chapter 4. The last chapter is listing several topics for my future activity.

Chapter I: Models overview and implementation

This chapter summarizes the basic concepts of micromagnetic theory, used extensively for modelling ferromagnetic nanostructured systems, including thin films, wires, and nanopillars. In the first section, the assumptions used in micromagnetism are listed and the ingredients needed for the general equations governing the magnetically stable state and the magnetization dynamics (interactions, energies, fields) are introduced.

Micromagnetism is a continuum description of ferromagnetic materials that exhibit a spontaneous magnetization M_s below a critical temperature T_C . A ferromagnetic system is rarely uniformly magnetized. In most of the cases, it consists of several regions with uniform magnetization vector \mathbf{M} (magnetic domains) separated by transition regions (magnetic domain walls), inside of which the orientation of the magnetization changes with position. To describe such entities, several concepts were developed by Weiss [Weiss1907] and Landau and Lifshitz [Landau1935] but it was Brown who unified all of them in a unitary theory known as *micromagnetism* [Brown1957].

Magnetic moments and magnetic order have quantum mechanical origin, but such an atomistic description is replaced in micromagnetism by continuous functions, which thus limits the smallest scale of applicability to few nanometers. In a ferromagnet the individual magnetic moments are strongly coupled through exchange interactions that tend to align neighboring moments parallel, thus creating a local magnetization \mathbf{M} (a net magnetic moment per unit volume) with a uniform magnitude M_s . The magnetization $\mathbf{M}(\mathbf{r},t)$ is a continuous function that depends on space and time, related to the unit vector $\mathbf{m}(\mathbf{r},t)$:

$$\begin{cases} \mathbf{M}(\mathbf{r},t) = M_s \mathbf{m}(\mathbf{r},t) \\ |\mathbf{m}(\mathbf{r},t)| = 1 \end{cases} \quad (1.1)$$

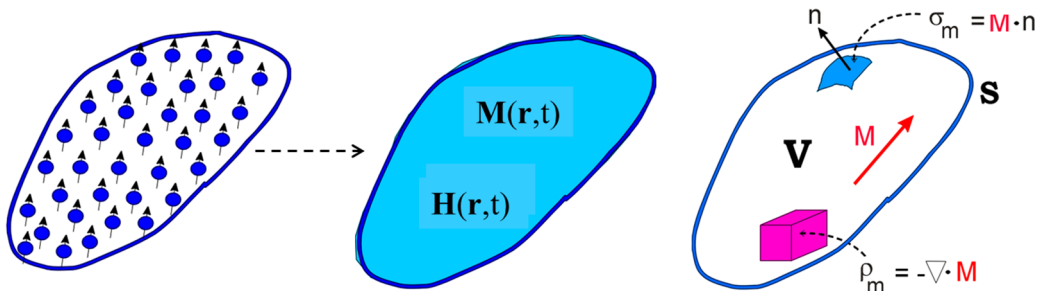


Fig.1.1 Continuous representation of a ferromagnetic system in micromagnetism. The sample has a volume V and a free surface S of normal vector \mathbf{n} . The distribution of individual spins is replaced by a continuous magnetization and magnetic charges.

The magnitude of the magnetization M_s is a temperature-dependent material parameter. However the orientation of the magnetization $\mathbf{m}(\mathbf{r},t)$ cannot be determined based only on the exchange coupling. The sources of non-uniform magnetization distribution are forces due to coupling with the crystalline structure, dipolar forces arising from magnetostatic charges, and forces due to external magnetic fields. These forces perturb the parallel alignment imposed by the exchange coupling, yielding variations in the orientation of the magnetization vector. In micromagnetism, the magnetization is assumed to vary gradually in space. Particular cases such magnetization discontinuities must be addressed with precaution. Depending on the forces, external and internal, acting upon a magnetic system, different equilibrium magnetization

configurations are foreseeable. Micromagnetic theory enables one to predict the spatial orientation of the magnetization under a set of conditions. A magnetic state corresponds to a local minimum of the total energy of the system. The temperature is assumed to be uniform in the material and for an isothermal process, the appropriate energy functional is the Gibbs free energy [Brown1963].

1.1 Gibbs free energy

The free energy of a ferromagnetic system of volume V and under the influence of an external magnetic field contains several terms: exchange energy, magnetocrystalline anisotropy energy, demagnetizing energy, and Zeeman energy:

$$E_{tot} = \int_V \epsilon_{tot} dV = E_{ex} + E_{anis} + E_{dem} + E_{app} \quad (1.2)$$

The exchange interaction is a interaction coupling two neighboring spins. It arises from the quantum mechanical principle of exchange symmetry, which states that no observable physical quantity should change after exchanging two indistinguishable particles. The Hamiltonian of the exchange interaction can be written as [Buschow2013]:

$$\mathcal{H}_{ex} = -2 \sum_{\langle i,j \rangle} J_{ij} \mathbf{S}_i \cdot \mathbf{S}_j \quad (1.3)$$

where J_{ij} is the Heisenberg exchange integral. Since it is a short-range interaction, one can consider the sum being over the nearest neighbors only. The sign of J_{ij} determines whether the material is ferromagnetic (parallel alignment is favored) or antiferromagnetic (antiparallel alignment). For a constant modulus of the spins $|\mathbf{S}_i| = |\mathbf{S}_j| = S$, and small misalignment between neighboring spins, the scalar product $\mathbf{S}_i \cdot \mathbf{S}_j$ can be expressed as:

$$\mathbf{S}_i \cdot \mathbf{S}_j = S^2 \left\{ 1 - \frac{1}{2} [(\mathbf{r}_{ij} \cdot \nabla) \mathbf{m}(\mathbf{r}_i)]^2 \right\}, \quad (1.4)$$

where \mathbf{r}_{ij} is the distance between the two neighboring spins. If we shift from a discrete to a continuous description and consider an isotropic exchange interaction ($J_{ij}=J$), the following Hamiltonian may be derived:

$$\mathcal{H}_{ex} = JS^2 \sum_i \left\{ [\Delta \mathbf{r}_i \cdot \nabla m_x(\mathbf{r}_i)]^2 + [\Delta \mathbf{r}_i \cdot \nabla m_y(\mathbf{r}_i)]^2 + [\Delta \mathbf{r}_i \cdot \nabla m_z(\mathbf{r}_i)]^2 \right\} + C \quad (1.5)$$

Dropping the additive constant C and summing over all the spins leads to the expression of the exchange energy:

$$E_{ex} = \int_V A_{ex} \left\{ [\nabla m_x(\mathbf{r})]^2 + [\nabla m_y(\mathbf{r})]^2 + [\nabla m_z(\mathbf{r})]^2 \right\} d\mathbf{r} \quad (1.6)$$

where A_{ex} is the exchange stiffness constant, having the dimensions of energy per unit length. Typical values of A_{ex} are on the order of 10^{-11} J/m. In the case of a simple cubic lattice with lattice parameter a , $A_{ex} = JS^2 / a$.

The environment of a magnetic moment acts on its orientation to favor certain directions in space. The charge distribution of the ions that form the crystal lattice generate an anisotropic electrostatic field that influences the orbital angular momentum of the electrons. Due to the spin-orbit coupling, this in turn generates preferred orientations of the spins and therefore of the magnetization along particular directions in space (called the easy axis of magnetization). This coupling between magnetization and crystal properties is quantified by the magnetocrystalline anisotropy energy. Its expression depends on the symmetry of the crystalline structure [Hubert1998]. For instance, one can define uniaxial, cubic, or hexagonal

magnetocrystalline anisotropy. The most common case is that of uniaxial anisotropy for which the corresponding energy has the expression,

$$E_{anis} = \int_V K_u \{1 - [\mathbf{u}_k \cdot \mathbf{m}(\mathbf{r})]^2\} d\mathbf{r} , \quad (1.7)$$

where \mathbf{u}_k is a unit vector along the direction of the easy axis and K_u is the temperature dependent anisotropy constant, expressed in J/m³. In thin films and multilayers, other anisotropy terms of surface or interfacial origin can have a major influence. This surface anisotropy arises from surface or interfacial phenomena such as electronic hybridization, stress, or symmetry breaking. An effective anisotropy constant K_{eff} is then expressed as the sum of the bulk and surface anisotropies: $K_{eff} = K_u + (K_{s1} + K_{s2})/t$, where K_{s1} and K_{s2} are the surface anisotropy constants that correspond to the top and bottom interfaces of the magnetic layer and t is the layer thickness.

A ferromagnetic material contains several magnetic domains pointing in different directions. The exchange interaction yields alignment of the magnetic moments inside a domain, but it does not explain why domain walls are formed. In fact, a long-range interaction, the magnetostatic interaction, accounts for the domain structure. Each magnetic moment in the ferromagnet is a dipole that produces a field experienced by other magnetic moments. Thus, a pair of dipoles driven only by the magnetostatic interaction will minimize its energy by pointing in opposite directions. Thus, in a ferromagnet, exchange and magnetostatic interactions are in competition, the former aligning the moments in the same direction, and the latter creating oppositely aligned domains over long distances. It follows that the typical size of the domains results from the relative strengths of these two interactions. Unlike the exchange interaction, which is local, the magnetostatic field at a given point is a sum over the contributions of all the magnetic moments in the whole magnetic volume. Subsequently, the numerical computation of this field is much more time-consuming than that of other fields.

In absence of any electrical current, the expression of the magnetostatic field \mathbf{H}_m can be derived from three fundamental equations: the relationship between \mathbf{H}_m and \mathbf{M} given by

$$\mathbf{B} = \mu_0 (\mathbf{H}_m + \mathbf{M}) \quad (1.8)$$

and the two Maxwell equations,

$$\begin{cases} \nabla \cdot \mathbf{B} = 0 \\ \nabla \times \mathbf{H}_m = 0 \end{cases} \quad (1.9)$$

Here $\mu_0 = 4\pi \times 10^{-7}$ H/m is the vacuum permeability. The dipolar field is irrotational, which means that \mathbf{H}_m is a conservative vector field. Therefore, there exists a scalar potential ϕ_m (magnetic scalar potential) such that $\mathbf{H}_m = -\nabla \phi_m$. The magnetostatic problem is reduced to Poisson's equation,

$$\nabla^2 \phi_m = -\nabla \cdot \mathbf{M}, \quad (1.10)$$

complemented by the radiation condition at infinity, $\mathbf{H}_m(\mathbf{r} \rightarrow \infty) \rightarrow 0$. At the interface between two regions of the space (e.g., 1 and 2), the magnetic scalar potential ϕ_m is a continuous function but its normal derivative is discontinuous,

$$\begin{cases} \phi_{m,1} = \phi_{m,2} \\ \frac{\partial \phi_{m,1}}{\partial \mathbf{n}} - \frac{\partial \phi_{m,2}}{\partial \mathbf{n}} = -(\mathbf{M}_1 - \mathbf{M}_2) \cdot \mathbf{n} \end{cases}, \quad (1.11)$$

where \mathbf{n} is the normal vector pointing from region 1 to region 2. By analogy with electrostatics, $\rho_m = \nabla \cdot \mathbf{M}$ represents the volume magnetic charge density and $\sigma_m = -\mathbf{M} \cdot \mathbf{n}$ represents the surface magnetic charge density, respectively. The magnetostatic Eqs. (1.10) and (1.11) may

be solved by Green's method. The magnetic scalar potential for a three-dimensional sample is given by the integral expression,

$$\phi_m(\mathbf{r}) = \int_V G(\mathbf{r} - \mathbf{r}') \rho_m(\mathbf{r}') d\mathbf{r}' + \int_S G(\mathbf{r} - \mathbf{r}') \sigma_m(\mathbf{r}') d\mathbf{r}', \quad (1.12)$$

where $G(\mathbf{r} - \mathbf{r}') = \frac{1}{4\pi|\mathbf{r} - \mathbf{r}'|}$ is the associated Green's function. The magnetostatic field evaluation is straightforward:

$$\begin{aligned} \mathbf{H}_m(\mathbf{r}) &= -\int_V \nabla G(\mathbf{r} - \mathbf{r}') \rho_m(\mathbf{r}') d\mathbf{r}' - \int_S \nabla G(\mathbf{r} - \mathbf{r}') \sigma_m(\mathbf{r}') d\mathbf{r}' \\ &= -[\nabla G * \rho_m](\mathbf{r}) - [\nabla G * \sigma_m](\mathbf{r}) \end{aligned}, \quad (1.13)$$

where $*$ is the convolution product. Various names are given to the magnetostatic field. For the sake of clarity, it will be called stray field $\mathbf{H}_{\text{stray}}$ outside the material and demagnetizing field \mathbf{H}_d inside. The demagnetizing energy that quantifies the interaction of the magnetization with the magnetostatic field created by itself, is given by the integral

$$E_{dem} = -\frac{1}{2} \mu_0 \int_V M_s \mathbf{m}(\mathbf{r}) \cdot \mathbf{H}_d(\mathbf{r}) d\mathbf{r}. \quad (1.14)$$

Following the pole-avoidance principle [Brown1963] the demagnetizing energy is minimized if the magnetic charges are minimized. This occurs when the magnetization follows closed paths as illustrated on Fig.1.2. The formation of domains leads to a reduced magnetostatic energy at the expense of increased exchange energy. Since surface magnetic charges are located at the boundaries, the magnetization tends to align along the edge. The so-called shape anisotropy is therefore ascribed to the magnetostatic interaction.

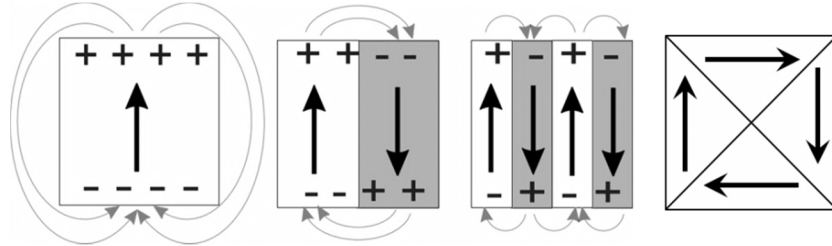


Fig.1.2 Magnetostatic field generated by a ferromagnetic sample. From left to right: single-domain configuration, two-domain configuration, four domain configuration, and flux closure domains. The magnetostatic energy is decreased by dividing the sample into several magnetic domains. The surface magnetic charges (+, -) disappear for the flux-closure case, but volume magnetic charges form at the domain walls. The black arrows represent the magnetization within each domain.

Generally the demagnetizing field is non-uniform even if the magnetization is uniform. However, in the particular case of a body whose surface is of second degree, a uniform magnetization implies a uniform demagnetizing field. For Cartesian coordinates along the principal axes of the system, the equation of the surface boundary is $\left(\frac{x}{a}\right)^2 + \left(\frac{y}{b}\right)^2 + \left(\frac{z}{c}\right)^2 = 1$,

where a , b , and c are the semi-axis lengths. If $c \rightarrow \infty$, the surface is an infinite cylinder of elliptical cross-section. If a , b , and c all take finite values, the body is an ellipsoid. For a uniformly magnetized ellipsoid with only surface magnetic charges, the demagnetizing field is also uniform. One can define a demagnetizing tensor \mathbf{N} such that

$$\mathbf{H}_d = -\mathbf{N} \cdot \mathbf{M}. \quad (1.15)$$

The demagnetizing field does not require heavy computation for uniform magnetization, contrary to the general case of non-uniform magnetization, since the tensor \mathbf{N} is diagonal if expressed in the basis of the principal axes:

$$\mathbf{N} = \begin{pmatrix} N_{xx} & 0 & 0 \\ 0 & N_{yy} & 0 \\ 0 & 0 & N_{zz} \end{pmatrix}. \quad (1.16)$$

The demagnetizing coefficients N_{xx} , N_{yy} and N_{zz} are positive, since the field H_d demagnetizes the sample. Moreover, the trace of \mathbf{N} is equal to 1, i.e., $N_{xx} + N_{yy} + N_{zz} = 1$. The analytical expressions of the demagnetizing coefficients are well-known for the three types of ellipsoids of revolution: (1) sphere $a = b = c$, (2) oblate spheroid $a = b > c$, (3) prolate spheroid $a = b < c$. The case of the sphere is the most simple, with $N_{xx} = N_{yy} = N_{zz} = 1/3$, due to the symmetry. The formulas in the two other cases can be found in Osborn. In the limit of $a, b \gg c$ one obtains the case of a continuous thin film $N_{xx} = N_{yy} = 0$ and $N_{zz} = 1$.

If a magnetic field \mathbf{H}_{app} is applied, the magnetization \mathbf{M} experiences a torque, which tends to align it parallel to the applied field direction. Due to the misalignment between \mathbf{H}_{app} and \mathbf{M} , a supplementary contribution has to be included in the total energy,

$$E_{app} = -\mu_0 \int_V M_S \mathbf{m}(\mathbf{r}, t) \cdot \mathbf{H}_{app}(\mathbf{r}, t) d\mathbf{r}, \quad (1.17)$$

The externally applied field can be time dependent and non-uniform in space. Most studies consider the basic case of an applied magnetic field, regardless of its source. However, two cases are of particular interest: a magnetic field generated by an external magnet and a magnetic field generated by an electrical current.

Case 1) The first case is typical in magnetic nanopillars composed of several ferromagnetic layers coupled through magnetostatic interactions. Using the formalism of the previous paragraph one might evaluate the stray field $\mathbf{H}_{stray}(\mathbf{r})$ acting on a particular layer generated by the external magnets (e.g., the other magnetic layers of the stack).

Case 2) In the second case, an electrical current distribution surrounding the magnetic sample, or even flowing through it, generates the commonly called Oersted or Ampère magnetic field. This situation is common in MRAM where the write field is generated by electric current pulses $\mathbf{J}_{app}(\mathbf{r}, t)$ injected in the write lines.

The Oersted field $\mathbf{H}_{Oe}(\mathbf{r})$ is the solution of the Maxwell equation,

$$\nabla \times \mathbf{H}_{Oe}(\mathbf{r}, t) = \mathbf{J}_{app}(\mathbf{r}, t). \quad (1.18)$$

Integration over a contour C yields Ampère's circuital law,

$$\oint_C \mathbf{H}_{Oe} \cdot d\ell = I_{enclosed}, \quad (1.19)$$

where $I_{enclosed}$ is the current flowing through loop C .

In the very particular case of an infinite cylinder of circular cross-section traversed by a rotationally-symmetric current (e.g., uniform current), the Oersted field is directed along \mathbf{u}_θ . Then, for a circular contour C centered about the cylinder axis, the amplitude of the Oersted field is

$$H_{Oe}(r) = \frac{I_{enclosed}}{2\pi r}, \quad (1.20)$$

where r is the radius of C . If r is larger than the cylinder radius R , then the Oersted field decreases as $1/r$.

For a uniform current density J_{app} inside the cylinder, $H_{Oe}(r) = J_{app}r/2$ when $r < R$. The Oersted field is maximum at the edge of the cylinder, equal to $J_{app}R/2$. Therefore, for a given current density, the maximum intensity of the Oersted field inside a nanopillar depends on its lateral size (see Fig. 1.3). For the general case (specific shape of the conductor, nonuniform current distribution) one has to use the formalism based on the magnetic vector potential \mathbf{A} from which the Oersted field is

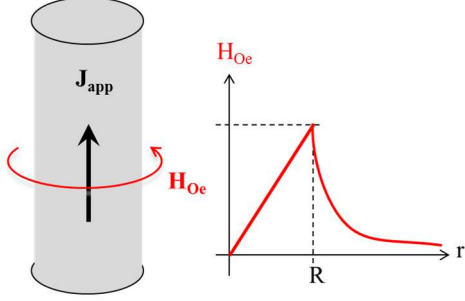


Fig.1.3 An electric current J_{app} flowing through an infinite cylindrical conductor generates the Oersted field H_{Oe} with characteristic space dependence. R is the radius of the cylinder, r the radial coordinate.

derived: $\mathbf{H}_{Oe} = \frac{1}{\mu_0} \nabla \times \mathbf{A}$. This requires a solution of Poisson's equation for the magnetic vector potential \mathbf{A} ,

$$\nabla^2 \mathbf{A} = -\mu_0 \mathbf{J}_{app} \quad , \quad (1.21)$$

complemented by the radiation condition at infinity $H_{Oe}(\mathbf{r} \rightarrow \infty) \rightarrow 0$. This equation must be solved numerically for non-uniform current distributions.

The list of the energies presented here is not exhaustive; other contributions might be included in the free energy functional depending on the additional interactions exhibited by the sample (e.g., coupling with an antiferromagnet, Ruderman-Kittel-Kasuya-Yosida (RKKY) exchange interactions, chiral exchange,...).

1.2 Magnetic stable state and equilibrium equations

The free energy functional might have several local minima; each of them is corresponding to a possible magnetically stable state. According to the variational principle, at equilibrium, the magnetization distribution inside the sample $\{\mathbf{m}(\mathbf{r}, t) | \mathbf{r} \in V, |\mathbf{m}(\mathbf{r}, t)| = 1\}$ satisfies simultaneously

$$\text{the following conditions: } \begin{cases} \delta E_{tot}(\mathbf{m}) = 0 \\ \delta^2 E_{tot}(\mathbf{m}) > 0 \end{cases} \quad (1.22)$$

where $\delta E_{tot}(\mathbf{m}) = E_{tot}(\mathbf{m} + \delta \mathbf{m}) - E_{tot}(\mathbf{m})$ is representing an infinitesimal variation of the energy induced by a small change in the magnetization $\delta \mathbf{m}$. One might show that the energy variation for a sample with uniaxial magnetocrystalline anisotropy takes the following relation:

$$\begin{aligned} \delta E_{tot}(\mathbf{m}) = \mu_0 \int_V M_s \left[\frac{2A_{ex}}{\mu_0 M_s} \nabla^2 \mathbf{m} + \frac{2K_u}{\mu_0 M_s} (\mathbf{u}_k \cdot \mathbf{m}) \mathbf{u}_k + \mathbf{H}_{app} + \mathbf{H}_d \right] \cdot \delta \mathbf{m} dV \\ + \oint_S 2A_{ex} \left(\mathbf{m} \times \frac{\partial \mathbf{m}}{\partial n} \right) dS \end{aligned} \quad (1.23)$$

The quantity between the brackets from the first term represents an effective field,

$$\mathbf{H}_{eff} = \frac{2A_{ex}}{\mu_0 M_s} \nabla^2 \mathbf{m} + \frac{2K_u}{\mu_0 M_s} (\mathbf{u}_k \cdot \mathbf{m}) \mathbf{u}_k + \mathbf{H}_{app} + \mathbf{H}_d \quad , \quad (1.24)$$

defined in general case as the variational derivative of the free energy density ε_{tot}

$E_{tot} = \int_V \varepsilon_{tot} dV$ with respect to the magnetization,

$$\mathbf{H}_{eff} = -\frac{1}{\mu_0 M_s} \frac{\delta \varepsilon_{tot}}{\delta \mathbf{m}} \quad (1.25)$$

To obtain the equilibrium condition, both the surface and volume integrals from (1.23) must vanish. This is possible only if simultaneously two conditions are fulfilled:

$$\begin{cases} \frac{\partial \mathbf{m}}{\partial n} = 0 & \forall \mathbf{r} \in S \\ \mathbf{m}(\mathbf{r}, t) \times \mathbf{H}_{\text{eff}}(\mathbf{r}, t) = 0 & \forall \mathbf{r} \in V \end{cases} . \quad (1.26)$$

These conditions were deduced by Brown and therefore are called the Brown equations. Their solution specifies the equilibrium state. The first one is a Neumann boundary condition, which forces the magnetization to be stationary near the sample surface S . The second equation states that for a magnetization distribution to be at equilibrium, the torque acting on \mathbf{m} due to the effective field must be zero everywhere (the magnetization is aligned with the effective field).

1.3 Equations of magnetization motion

The Brown equations are completely defining the equilibrium state of a magnetic system, but they do not specify how the system reaches this state. The magnetization dynamics can be accessed through the Landau-Lifshitz-Gilbert equation. The starting point is represented by the well-known equation of Larmor,

$$\frac{\partial \mathbf{m}}{\partial t} = -\gamma(\mathbf{m} \times \mu_0 \mathbf{H}) \quad , \quad (1.27)$$

Which describes the magnetization's gyrotropic reaction in the presence of the magnetic field \mathbf{H} . Here γ is the gyromagnetic ratio of the free electron ($1.76 \times 10^{11} \text{ s}^{-1}\text{T}^{-1}$). The Larmor equation is conservative. Its solution corresponds to a magnetization which precesses endlessly, with constant precession angle and energy. However, in real ferromagnetic materials, dissipation processes cause the system to minimize its energy and to reach, after certain time, a stable state ($\partial \mathbf{m} / \partial t = 0$). In order to take account of dissipation, a term has to be added to Eq. (1.27), allowing the magnetization to reach static equilibrium. Gilbert [Gilbert1955, Gilbert2004] suggested introducing magnetic damping as a viscous force proportional to the time-derivative of the magnetization according to the Rayleigh dissipation functional. The Gilbert equation of motion includes precession and relaxation:

$$\frac{\partial \mathbf{m}}{\partial t} = -\gamma_0(\mathbf{m} \times \mathbf{H}_{\text{eff}}) + \alpha \left(\mathbf{m} \times \frac{\partial \mathbf{m}}{\partial t} \right) . \quad (1.28)$$

The damping α is a dimensionless phenomenological constant, arising from all dissipation processes (e.g., magnon-magnon scattering, magnon-phonon scattering, Eddy currents) and $\gamma_0 = \mu_0 \gamma$. The meaning and the measurement of α is an intricate matter, since its value depends not only on the material, but also on experimental conditions. For most common ferromagnetic materials α is a scalar ranging from 5×10^{-4} to 0.1.

Since magnetization magnitude is conserved during the motion, if $\alpha \ll 1$, the Gilbert equation can be transformed in an equivalent form, previously introduced by Landau and Lifshitz

$$\frac{\partial \mathbf{m}}{\partial t} = -\gamma_L(\mathbf{m} \times \mathbf{H}_{\text{eff}}) + \lambda \mathbf{m} \times (\mathbf{m} \times \mathbf{H}_{\text{eff}}) \quad (1.29)$$

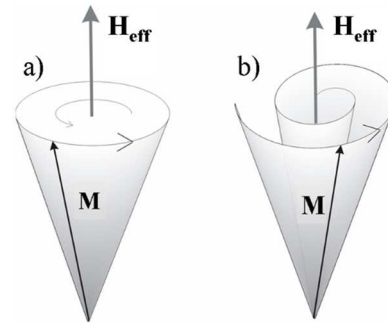


Fig.1.4 Precession of the magnetization vector \mathbf{M} about the field \mathbf{H}_{eff} : (a) without damping and (b) with a damped motion ($\alpha > 0$).

here, $\gamma_L = \frac{\gamma_0}{1 + \alpha^2}$ and $\lambda = \frac{\gamma_0 \alpha}{1 + \alpha^2}$. The Landau-Lifshitz equation is of great interest for numerical resolution since the time derivative of \mathbf{m} is directly expressed as function of \mathbf{m} and \mathbf{H}_{eff} . The magnetization motion is illustrated on *Fig. 1.4*.

1.4 Length scales in micromagnetism

In micromagnetic modelling, particular attention has to be paid to length scales in order to always comply with the fundamental hypotheses of the micromagnetic model. The simulated system is divided into elementary cells and the micromagnetic equations are solved in each of these elements. The accuracy of the result depends strongly on the element size; the smaller, the more accurate, but also the longer the simulation. Therefore, an appropriate cell size has to be chosen. Since the exchange interaction has the shortest range, its strength with respect to other forces determines the typical scale over which the magnetization can vary. Two characteristic lengths can be defined: the exchange length λ_{ex} and the Bloch length λ_B . The competition between the exchange interaction and the demagnetizing energy is measured by the exchange length defined as:

$$\lambda_{ex} = \sqrt{\frac{2A_{ex}}{\mu_0 M_s^2}} \quad (1.30)$$

Usually the exchange length is giving the width of magnetic vortex core. The Bloch length is the typical width of a Bloch wall (transition between two magnetic domains antiparallel orientated over which the magnetization rotates perpendicularly to the plane of the wall, unlike the Néel wall where the rotation is within the plane of the domain wall). It is given by the relative strength of the exchange interaction over the magnetocrystalline anisotropy:

$$\lambda_B = \sqrt{\frac{A_{ex}}{K_u}} \quad (1.31)$$

For accurate micromagnetic simulations, the element size has to be smaller than these two lengths. For instance, in Permalloy ($\text{Ni}_{80}\text{Fe}_{20}$), the cell dimension is limited by the exchange length, which is about 5 nm. Therefore an accurate simulation requires a typical cell size of about 2.5 nm.

1.5 Modification related to spin polarized current

The dynamic Eq. (1.28) or (1.29) is suitable for describing the evolution of a micromagnetic system excited by an external magnetic field. However, since the first evidence of the effect of an electric current on magnetization, this phenomenon, called spin-transfer torque (STT), has attracted more and more interest. In order to describe this new kind of interaction, the Landau-Lifshitz-Gilbert equation has to be adapted. The STT generated by a spin-polarized current on the magnetization is represented by an additional term that should be added to the magnetization equation of motion, Eq. (1.28). The debate about the exact expression for the STT is still under consideration, but the most used models are briefly presented below.

For the case of nanopillars, spin-dependent transport theory predicts two terms [*Slonczewski1996, Berger1996*]:

$$\left(\frac{\partial \mathbf{m}}{\partial t} \right)_{STT} = -\gamma_0 a_j \mathbf{m} \times (\mathbf{m} \times \mathbf{p}) - \gamma_0 b_j (\mathbf{m} \times \mathbf{p}) \quad (1.32)$$

The vector \mathbf{p} represents the direction of the pinned layer (of the polarizer), supposed to be fixed. Both terms are current dependent, since a_j and b_j are more or less complicated functions of the

injected current. The term in \mathbf{b}_j can be included in the expression of the effective field; it is therefore called *field-like* torque. In contrast, the term in \mathbf{a}_j is often referred to as the Slonczewski torque or the in-plane torque or damping-like. In metallic spin valves and multilayers, the \mathbf{b}_j term is usually much smaller than the \mathbf{a}_j term. However, in magnetic tunnel junctions, the *field-like* term can be of the same order of magnitude as Slonczewski torque and should be also taken into account to have an accurate description of the magnetization dynamics. It is interesting to note that the effective field term in the LLG equation is deriving from an energy, whereas the in-plane spin torque cannot be associated to any energy since the system is continuously excited. It actually behaves like a damping or antidamping term, depending on the current direction.

If the current flows through a magnetic nanowire containing a domain wall parallel to the wire cross-section, the spin of the conduction electrons interacts with the magnetization of the magnetic domain wall. Two torque terms model this interaction [Thiaville2005]: an adiabatic term and a nonadiabatic term,

$$\left(\frac{\partial \mathbf{m}}{\partial t}\right)_{STT} = -(\mathbf{u} \cdot \nabla) \mathbf{m} - \beta \mathbf{m} \times [(\mathbf{u} \cdot \nabla) \mathbf{m}]. \quad (1.33)$$

The vector \mathbf{u} has units of velocity; it is parallel with the direction of the electron flow:

$\mathbf{u} = \mathbf{J}_{\text{app}} \frac{g\mu_B P}{2eM_s}$ (here, $g = 2$ is Landé factor of the free electron, μ_B is the Bohr magneton, P is the current polarization fraction ($0 < P < 1$), and e is the electron charge).

Novel out-of-equilibrium transport phenomena have also been demonstrated, such as current induced spin-orbit torques induced by the Rashba spin-orbit coupling (SOC) and/or the spin Hall effect, leading to current induced magnetization reversal [Miron2011, Liu2012]. This phenomenon might be included in the equation of motion by a SOC contribution proportional to the electric current:

$$\left(\frac{\partial \mathbf{m}}{\partial t}\right)_{SOC} = \gamma_0 C_{FL} J_{\text{app}} [\mathbf{m} \times (\mathbf{u}_j \times \hat{\mathbf{z}})] + \gamma_0 C_{DL} J_{\text{app}} \mathbf{m} \times [\mathbf{m} \times (\mathbf{u}_j \times \hat{\mathbf{z}})] \quad (1.34)$$

C_{FL} and C_{DL} are sample-dependent coefficients, \mathbf{u}_j is unitary vector of the current direction and $\hat{\mathbf{z}}$ is unitary vector of z-axis (symmetry axis). Obviously this list of physical phenomena that can be included in micromagnetic studies is not exhaustive. A very interesting and absolutely necessary step to understand the behavior of a magnetic body is the study of thermal effects.

1.6 Thermal fluctuations

Magnetic properties are strongly dependent on temperature. In micromagnetism, the thermal fluctuations are taken into account, according to Brown's theory, by a random magnetic field \mathbf{H}_{th} when the temperature of the sample is much less than the Curie temperature (the transition temperature between the ferromagnetic and the paramagnetic states) [Brown1963]. The mean value of the thermal field is zero $\langle \mathbf{H}_{\text{th}}(\mathbf{r}_i, t_k) \rangle = 0$ and its auto-correlation function is given by:

$$\langle \mathbf{H}_{\text{th}}(\mathbf{r}_1, t_1) \cdot \mathbf{H}_{\text{th}}(\mathbf{r}_2, t_2) \rangle = D \delta(\mathbf{r}_1 - \mathbf{r}_2) \delta(t_1 - t_2) \quad (1.35)$$

D is the variance expressed as $D = \frac{2\alpha k_B T}{\mu_0 M_s V \gamma_0}$. Consequently, the thermal field has a Gaussian

distribution centered about zero with a variance proportional to the temperature T and the damping factor α , and inversely proportional to the magnetic volume V . The thermal field is added to the effective field \mathbf{H}_{eff} in the Landau-Lifshitz-Gilbert Eq. (1.28); in this case Eq. (1.28) becomes a Langevin equation. Since \mathbf{H}_{th} is a random field, it accounts for non-deterministic

(stochastic) processes. Therefore, running the same simulation several times at finite temperature leads to a distribution of magnetization trajectories; the larger the temperature, the broader the distribution.

1.7 Numerical micromagnetism

The typical length of magnetization variation is the exchange length λ_{ex} (or the Bloch length λ_B , whichever is the smallest). Therefore, if the lateral size of a ferromagnetic sample is on the order of, or only a few times, the exchange length, the magnetization can be considered uniform: $\mathbf{m}(\mathbf{r}, t) = \mathbf{m}(t)$. This approximation is called macrospin approximation (or *single-domain* approximation, or *uniform-mode* approximation). Instead of using the complicated Eq. (1.13), the mean demagnetizing field and the magnetostatic energy can be easily calculated with an equivalent demagnetizing tensor, Eqs. (1.15) and (1.16). The macrospin approximation is of great utility in building simple analytical models. Moreover, the LLG equation need be solved only for one single macrospin, which makes macrospin simulations much faster than micromagnetic computations. The energy landscape can be plotted within the macrospin approximation since the state of the system is fully given by two independent parameters (the third one being deduced from the conservation of the norm, e.g., the polar angles θ, ϕ). This is particularly useful to gain an insight into dynamic processes, such as magnetization reversal for example. Simple models can also be constructed and solved analytically, such as the Stoner-Wohlfarth model [Stoner1948] to explain magnetic hysteresis during switching, and the Kittel law [Kittel1948], which gives the ferromagnetic resonance (FMR) frequency of the uniform mode as a function of the applied field.

In most cases, the macrospin model is, however, a very rough approximation; three-dimensional micromagnetic simulations, e.g., $\mathbf{m}(\mathbf{r}, t)$, are required for a description of nonuniform magnetization. There are two types of micromagnetic simulations: either the equilibrium state is sought, or a complete time-varying computation is run to study the magnetization dynamics. Usually, the equilibrium state is needed to initialize the dynamic simulation. The most common method to find the micromagnetic equilibrium state is to relax the system with a large Gilbert damping (α) value. In this case, the path described by the magnetization (the intermediate states) has no physical meaning; only the final state corresponds to the physical state potentially reached by the system.

The resolution of the micromagnetic equations (nonlocal, integral equations) is demanding in terms of computational power. Time and space are discretized and the effective field is calculated in each element (or cell) at each time step. An approximate solution is given, but it has to converge to the exact result when the element size and the time step go to zero. A typical time step is about 0.1 ps (for a typical cell size of a few nanometers). The input parameters of any micromagnetic simulation are the saturation magnetization M_s , the exchange constant A_{ex} , and the anisotropy constant K_u . Moreover, the temperature T can be included, as well as a current density J_{app} and the spin polarization.

The micromagnetic solvers are based on different approximations and implementation methods. The finite difference method (FDM) is the most common numerical method for micromagnetic simulations because it is easier and faster than the finite element method (FEM).

The most widely used micromagnetic code utilizing the FDM is certainly the *Object Oriented Micromagnetic Framework* (OOMMF) software but many other software programs can be cited, such as the *LLG Micromagnetic Simulator* by M. R. Scheinfein, *MicroMagus* by D. V. Berkov and N. L. Gorn, *Magsimus* by J. Oti, *MuMax* by A. Vansteenkiste and B. Van de Wiele, *GoParallel* by L. Torres and E. Martinez, and *MicroMagnum* by A. Drews. The last three use graphics cards (GPUs) whereas the others run on single CPU processors. [FDM]

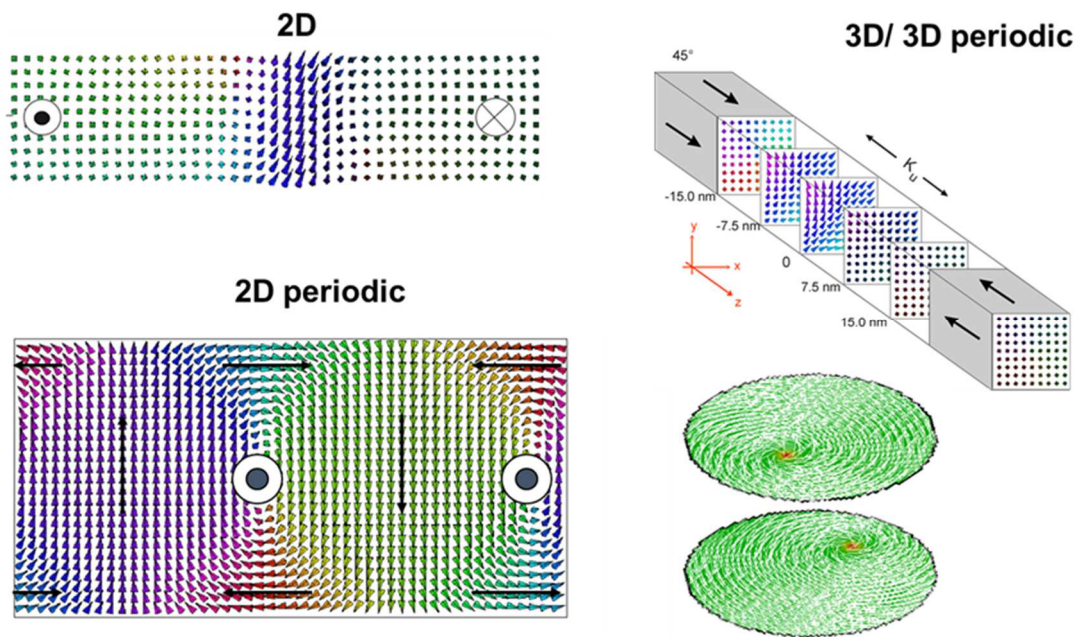


Fig 1.5 Exemplars of configurations 2D and 3D with and without periodicity issued from *Micro3D* solver.

Among other micromagnetic solvers based on the finite element method, one can cite *Nmag* by H. Fangohr, M. Franchin and T. Fischbacher, *Magpar* by W. Scholz, *FEMME* by D. Suess and T. Schrefl, *TetraMAG* by R. Hertel, *FastMag* by V. Lomakin, and *SallyMM* by O. Bottauscio and A. Manzin.

The studies reported hereafter were obtained using the *Micro3D* solver, a finite difference code, applied to explore the magnetic behavior of magnetic nanosize samples such as thin films, dots, and nanowires. Various types of sample are illustrated on the *Fig.1.5*. Some of the studies were carried on in parallel with the FEM solver *feLLGood* in collaboration with J.Ch. Toussaint from Néel Institute in the frame of several PhD thesis (H. Szambolics, E. Kritskis, A. Vaysset).

After setting the main elements of the models, their use is illustrated hereafter through condensed summaries. I prefer a topic driven organization instead a chronological one, revealing that topics are continuously evolving and the models should continuously be adjusted.

Chapter II: Magnetic domain walls

As a general definition the magnetic domain walls are local deformations of the magnetization in a ferromagnetic sample at the boundary separating two uniformly magnetized domains. They are very interesting magnetic objects. Firstly, their internal structure is intimately related to the properties of the magnetic sample (intrinsic parameters but also shape), they can be imaged by various magnetic microscopy techniques and allow one to probe the sample. Secondly, the magnetic domain walls react once a magnetic field is applied, they might propagate and thus contribute to the magnetization process of the sample. Furthermore, a spin polarized current can transfer spin angular momentum to the magnetic domain wall, induces changes of its internal structure and eventually drives the motion of the domain wall. The possibility to manipulate the magnetic domain wall by spin polarized current has launched plenty of innovative concepts for memory and logic devices. For all these reasons, the DW topic represents a large part of my activity from the very beginning and the major results are summarized hereafter.

The Bloch and Néel domain walls are known from the textbooks, they might be addressed analytically under some assumptions. However, pure Bloch or Néel walls are quite rare and, most of the time, the lateral confinement of a ferromagnetic sample has a big impact on the magnetization distribution and especially on the structure of the domain wall. This impact has been investigated for thin films but also for nanowires according to the time chart from Fig. 2.1 Progressively various features have been included in the micromagnetic solver in order to study the behavior of DW under the injection of spin polarized current (STT) and structural inversion symmetry related effects (SOT, DMI).

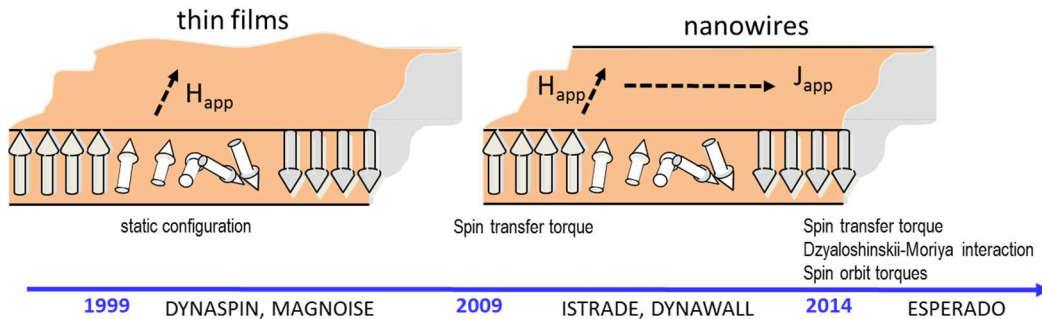


Fig. 2.1 Time evolution of the DW topic and the associated grants. The key phenomena included in the micromagnetic model are indicated.

2.1 Domain wall structure in thin films

The internal structure of magnetic domain walls in thin films has been a topic of predilection from the very beginning of my PhD. The first version of the micromagnetic solver has been dedicated to such 2D systems (translation symmetry along one axis). The micromagnetic solver have been mainly used firstly only for static computation both for periodic (2D stripes) and non-periodic samples. Mainly continuous single crystal thin films of Co have been investigated characterized by their large magnetocrystalline anisotropy. Depending on the substrate, the hexagonal compact structure of the Co might have the c -axis laying longitudinal or perpendicular to the thin film plane. For both cases the magnetization inside the sample is strongly influenced by the thickness as depicted in Fig. 2.2a. Magnetic

domains walls are stabilized between the magnetic domains having a hybrid structure between the standard Bloch and Néel walls. Such structures are the obvious result of a competition between internal interactions: exchange and anisotropy (magneto-crystalline and shape). In the middle of the layer the DW has a Bloch-like wall structure. However the magnetostatic effects behind the shape anisotropy are strongly affected by the size (here the thickness) of the sample. Thus, the magnetization prefers to be aligned with the surface of the sample to reduce the induced magnetic surface charges. The fact that the domain wall acquires a Néel-like structure at the surface proximity is a clear signature of the magnetostatic interaction. As a consequence one might expect having Néel walls in very thin Co layers with in-plane magnetocrystalline anisotropy ($t < 10\text{nm}$) or suppressing completely the domain wall for the perpendicular case ($t < 28\text{nm}$). The predicted variation of the domain wall structure in these films was found in good agreement with experimental observation by MFM [Prejbeanu2000] and FMR [Ebels2001].

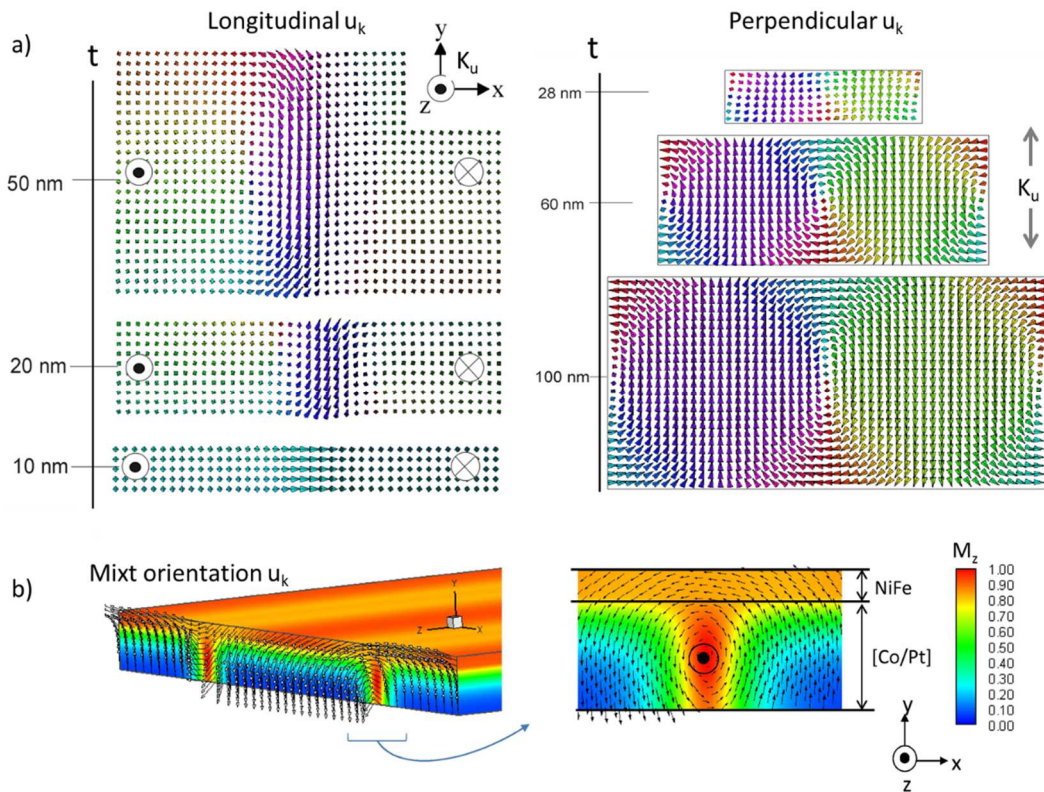


Fig. 2.2 a) Cross-sections showing the evolution of the domain wall internal structure with the thickness of the Co layer if the magnetocrystalline c -axis is laying in the plane or perpendicular to the plane of the film. The arrows are associated to projection of the magnetization vector on the cross-section plane. b) Modification of the domain wall structure in a bi-layer sample combining regions with different anisotropy.

This balance between effective anisotropy and exchange interaction on the magnetization pattern is illustrated also in the case of a thin layer composed of two different materials [Bollero2011]. A very thin NiFe soft layer is deposited on top of [Pt/Co] multilayer with out-of-plane anisotropy. One might notice that the NiFe soft layer is favoring the closure of the magnetic flux inside the sample. The presence of the magnetic domains from [Pt/Co] leads to a shift of the hysteresis loop of an adjacent NiFe thin film with in-plane anisotropy, in an analogous manner to the exchange bias phenomenon typically observed in ferromagnetic/antiferromagnetic systems. Playing with the sample parameters the suitable type of magnetic domain wall can be selected, the internal structure and width can be tuned.

2.2 Domain wall depinning assisted by current and magnetic field

The number of publications related to the magnetic domain walls in ferromagnetic nanowire is huge and a real boom followed once the current induced domain wall propagation have been proved. The large choice of materials, the control of the sizes and fabrication techniques allow the access to a large variety of samples. The first classification is done with respect to the relative orientation of the easy axis of the magnetization with the longitudinal axis of the nanowire. As a consequence, in the case of flat nanowires (i.e. nanotracks) the internal structure of the domain walls is very different: longitudinal configuration favors wide domain walls (~100nm, transverse wall or vortex wall) while for perpendicular configuration the domain walls are very sharp approaching ~10nm and even below.

The theoretical investigations based on diffusive model of spin-dependent transport have converged to the following phenomenological LLG equation (see *eq 1.33*):

$$\frac{\partial \mathbf{m}}{\partial t} = -\gamma(\mathbf{m} \times \mu_0 \mathbf{H}_{\text{eff}}) + \alpha \left(\mathbf{m} \times \frac{\partial \mathbf{m}}{\partial t} \right) - (\mathbf{u} \cdot \nabla) \mathbf{m} - \beta \mathbf{m} \times [(\mathbf{u} \cdot \nabla) \mathbf{m}].$$

The adiabatic torque $\sim (\mathbf{u} \cdot \nabla) \mathbf{m}$, which accounts for transport processes in which the spin of the conduction electrons follows the local spatial magnetization variation by remaining either the in majority or minority state, is well understood and has been reproduced by a number of different transport theories. In contrast, the non-adiabatic contribution $\beta \mathbf{m} \times [(\mathbf{u} \cdot \nabla) \mathbf{m}]$, characterized by a dimensionless parameter β , have been the subject of much debate. Various mechanisms have been put forward to explain its origin, such as momentum transfer, spin mistracking or spin-flip scattering. It is predicted that large nonadiabatic effects should appear in narrow domain walls because of large magnetization gradients, whereby the wall width becomes comparable to important transport scales such as the spin-diffusion length or the Larmor precession length, which are of the order of a few nm in ferromagnetic transition metals.

The presence of a non-adiabatic term is of fundamental importance, because its existence implies that current-driven wall motion is possible for any finite current in a perfect system, even in the absence of an applied magnetic field. The value of this non-adiabatic parameter appears as key question both for experimentalists and theoreticians. The experimental results (domain wall velocities, depinning field,...) have divided the community in two parts: one defending the scenario of small values for the β constant while the another part expects rather large values for β . The agreement between various groups has been not obvious from the very beginning for two main raisons:

i) difficulty in characterizing β experimentally therefore stems in part from being able to distinguish between extrinsic sources of wall pinning, due to structural defects, for example, from the intrinsic finite threshold current predicted for $\beta=0$.

ii) additional phenomena related to structural inversion asymmetry of the samples but at that time missing from the interpretation of the studies.

A main objective for us has been the estimation of the value of the non-adiabatic constant β for narrow domain wall having a Bloch-like internal structure. The general study has been carried out in the frame of the ISTRADE project focused on systems characterized by strong magnetocrystalline perpendicular anisotropy such as FePt and CoNi layers. This study is part of the PhD thesis of Helga Szabolics assisted by the Felipe Garcia-Sanchez. The associated experimental investigations have been done at former NM lab from INAC [Mihai2011] and respectively IEF[Burrowes2009]. The first common feature for these materials is the stabilization of very narrow domain walls separating out-of-plane magnetized magnetic

domains. The second feature of these samples (polycrystalline or single crystal) is that the dynamics of the magnetic domain wall is dominated by the natural crystalline defects occurring randomly. Such non-uniformity in the material parameters might affect the magnetic domain wall structure. If the size of the defect is very tiny with respect to the size of the magnetic domain wall, the defect induces a local perturbation inside the structure of the domain wall and the impact on domain wall motion is negligible. In contrast, if the size of the defect is in the same range with the domain wall width, the domain wall structure is deformed and the consequences might be important. During its displacement, the magnetic domain wall tries to avoid the regions with high anisotropy and in counterbalance to favor the regions with low anisotropy. As a consequence, the domain wall movement might be stopped, and the domain wall pinned if the energy barrier to overcome is too high. By studying thermally activated domain wall depinning, we have tried to get information on the β constant from the variation of the Arrhenius transition rate with the amplitude of the injected currents.

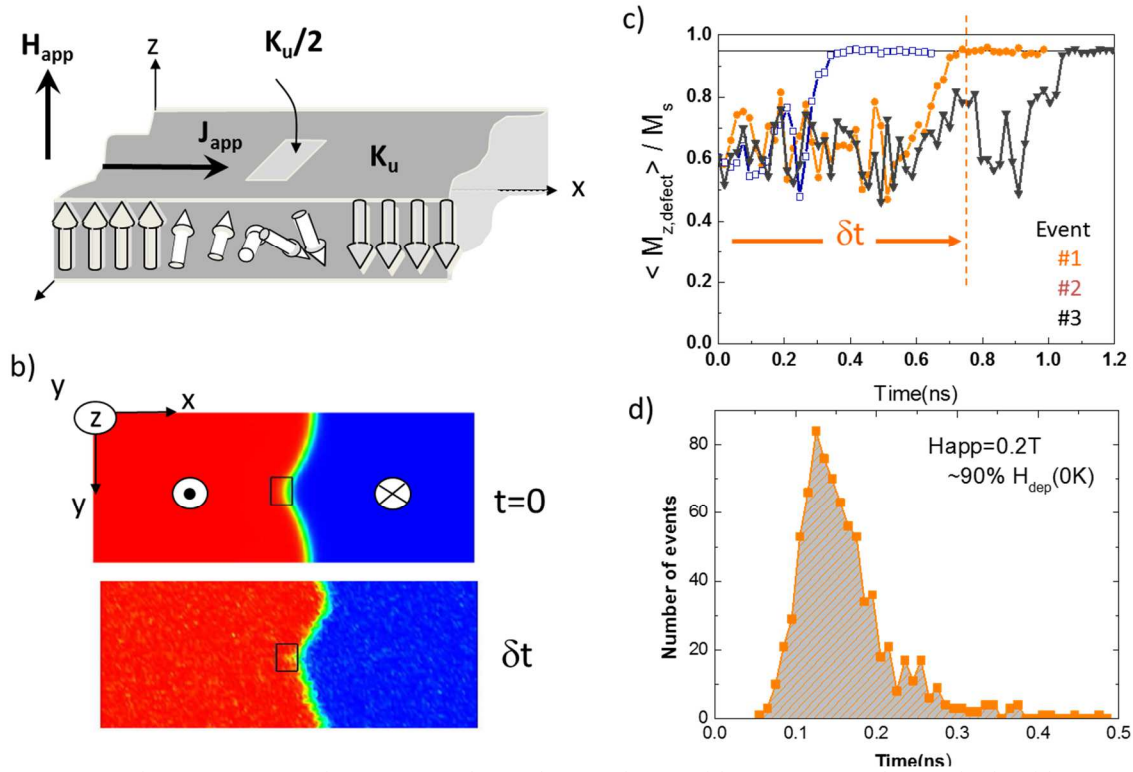


Fig. 2.3 a) Schematic view of the system and coordinates. b) Equilibrium state under applied field $\mu_0 H_{app} = 0.18 T$ at $0K$ and the configuration to one depinning event that $400K$. c) Time evolution of mean value of M_z/M_s calculated inside the defect for three different events. d) Distribution of the depinning events [Garcia2010].

A single defect have been considered view as a small region having the anisotropy reduced by half with respect to the rest of the sample (Fig. 2.3). In purpose, a magnetic domain wall is placed on the defect and an out-of-plane magnetic field lower than the depinning field is applied. At rest the magnetic domain wall is caught on the defect. The energy required to release the domain wall pinned on the defect is provided by thermal fluctuations. The dynamics of the magnetization is monitored in time for several hundred of events and the depinning is occurring stochastically. The depinning time is recorded and single peak distributions are obtained upon varying the applied field and the cumulative distribution function are evaluated giving the probability to have a depinning event after a time t . The analysis of the thermally activated processes is in general a complicated task. However, if the process corresponds to the crossing of a single energy barrier and that barrier is much larger than the thermal energy (i.e., $E_B \ll k_B T$, where E_B is the energy barrier that the DW has to overcome), the process can be described by an exponential probability law $F(t) = 1 - \exp(-t/\tau)$ where τ is the Arrhenius-

Néel relaxation time, given by $\tau = \tau_0 \exp(E_B / (k_B T))$, where τ_0 is the attempt frequency. For quite a large range of applied fields, we found a linear dependence of the energy barrier on the field value. Thus, we can express the energy barrier as: $E_B(H_{app}) = a_H H_{app} + b_H$. This expression represents weak pinning limit and was confirmed experimentally. However, there are differences in the time scales and the actual value of depinning fields. The first one can be assigned to the difficulties in extending our calculation beyond the nanosecond time scale, the latter to the lack of an accurate model for the defect. Nevertheless, the physics of the system is preserved, and the same behavior is obtained.

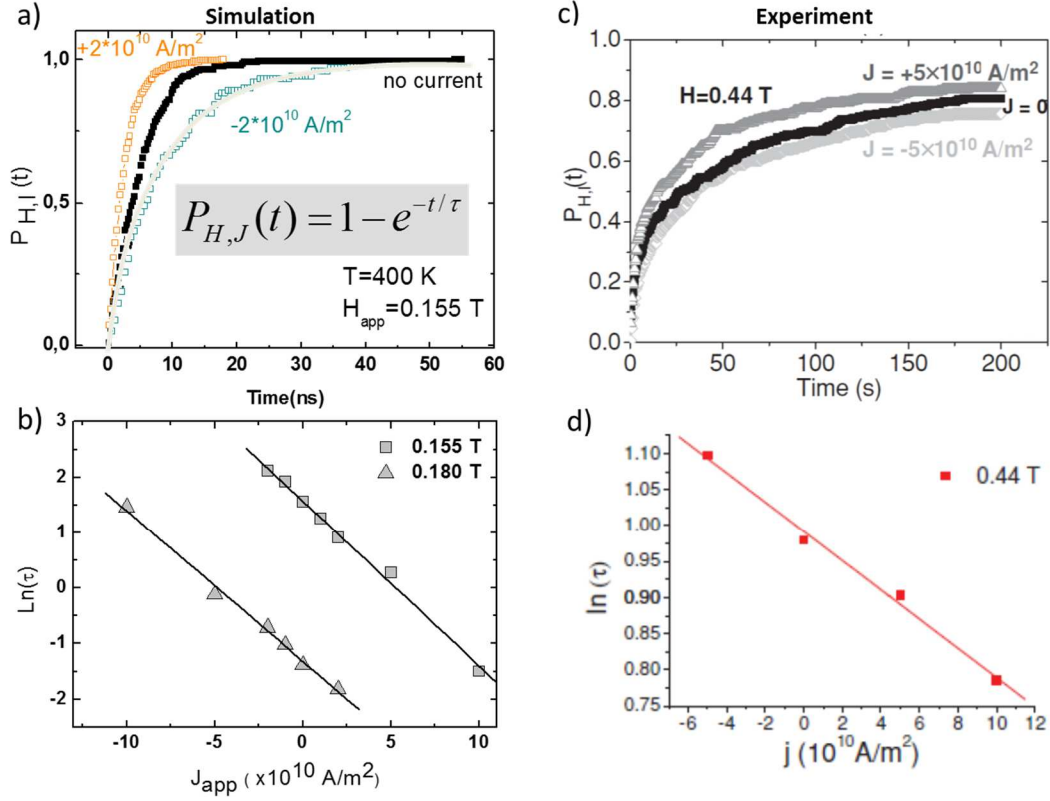


Fig. 2.4 a,c) Probability to be depinned as a function of time and b,d) the characteristic depinning time vs. the applied dc current. a,b are from simulation and c,d) from measurements [Mihai2011].

In the following, we fixed the magnetic field and applied current densities flowing parallel to the long axis of the wire (x -direction) (Fig.2.4). An appreciable effect on the average depinning time is observed even at low-current densities. Moreover, an asymmetric behavior of the probability with respect to the current polarity is present. The effect of negative current is to slow down the depinning, while positive current reduces the depinning time. This result is also consistent with the experimental observations. In Fig. 2.4b the time constant versus the current density for two different applied field values. Again, we observed a linear dependence of the energy barrier on the current density $E_B(J_{app}) = a_J J_{app} + b_J$ conformed experimentally Fig. 2.4d. From this linear current-dependent energy barrier the spin-torque efficiency parameter might be estimated $\xi = a_J / a_H$. Numerically we have found $\xi = 2.4 \cdot 10^{-13} \text{ Tm}^2 / \text{A}$ while the typical experimental value has been in the same order of magnitude $10^{-13} \text{ Tm}^2 / \text{A}$. The results issued from the statistic simulation have been consistent with the initial hypothesis of the model. To conclude, the experimental estimations found for non-adiabatic parameter β are the following: $\beta_{CoNi} = 0.002 \pm 0.002$ and $\beta_{FePd} = 0.06 \pm 0.03$ relatively small values similar to the usual values of the Gilbert damping. In the case of these very narrow magnetic domain walls

the efficiency of the STT is however small, the motion of the DW is strongly perturbed by the defects and thus quite large currents must be injected to get a fast and repeatable DW displacement.

2.3 Chiral magnetic domain walls

Continuing the history of the magnetic domain walls, a famous and remarkable system is the one based on Pt/Co/AlO_x, a trilayer association initially proposed at Spintec by B. Dieny and B. Rodmacq [Monso2002, Rodmacq2003, Manchon2008]. This ultra-thin Co ferromagnetic layer is also perpendicularly magnetized to the plane as the CoNi or FePt layers previously discussed. However, this time the magnetic domain walls are moving very fast $\sim 400\text{m/s}$ (Fig. 2.5). Also remarkable is the fact that the magnetic domain walls are moving against the flow of the electrons in contrast with the prediction of common STT theory [Thiaville2005]. These studies have been initiated in the frame of DYNAMALL grant involving colleagues as M. Miron, T. Moore, G. Gaudin, E. Jué, K. Safeer, O. Boulle and collaborators from Institute Néel (S. Pizzini, J. Vogel, A. Schuhl). The investigation have been pursued in the frame of ESPERADO French grant extending the collaboration to partners from LPS Orsay (A. Thiaville, S. Rohart, J. Miltat).

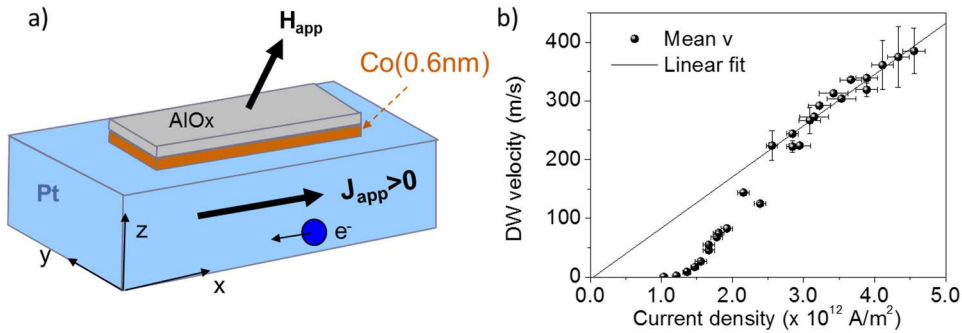


Fig. 2.5 a) Schematic of the Pt/Co/AlO_x trilayer structure. b) Experimental domain-wall velocity as a function of the current density [Moore2011].

After intensive investigations, specific phenomena have been pointed out progressively: Rashba effect, Dzyaloshinskii-Moriya interaction, spin hall effect, chiral damping and etc. These interactions are linked to the structural inversion asymmetry (SIA) and act on the magnetic and electronic transport properties at interfaces of low dimensional magnetic films. In the presence of spin-orbit coupling, SIA leads to an additional term in the exchange interaction, namely the Dzyaloshinskii-Moriya interaction (DMI), which tends to make the magnetization rotating around a local characteristic vector \mathbf{D} . This can destabilize the uniformly magnetized states leading to novel chiral magnetic orders, such as spin spirals. Novel out-of-equilibrium transport phenomena have also been demonstrated, such as current induced spin-orbit torques due to the Rashba spin-orbit coupling and/or the spin Hall effect, leading to current induced magnetization reversal.

According to Thiaville et al. [Thiaville2012] the DMI interaction has been included in the Micro3D solver as an additional contribution to the free energy density (eq.1.2) such as the effective field (eq.1.24) has a supplemental term namely

$$\mathbf{H}_{\text{DM}}(\mathbf{m}) = \frac{2D}{\mu_0 M_s} \left(\frac{\partial m_z}{\partial x}, \frac{\partial m_z}{\partial y}, -\frac{\partial m_x}{\partial x} - \frac{\partial m_y}{\partial y} \right).$$

Beside the boundary condition filled by the magnetization vector on the free surface of the sample must be consequently adjusted. Without DMI the expected domain wall structure is the common Bloch-like structure (Fig.2.6a). The first impact of the DMI is to modify progressively the DW equilibrium structure between Bloch

and Néel (*Fig.2.6c*). Above a critical value, the DMI leads to chiral DWs meaning that the magnetization rotates perpendicular to the DW surface with a unique sense of rotation. The positive value of the DM constant means hereafter left-handed domain walls. Note that these results have been one of the benchmarks of the Micro3D solver with respect to the Thiaville et al [*Thiaville2012*] and Micro3D was among the first solvers including DMI interaction.

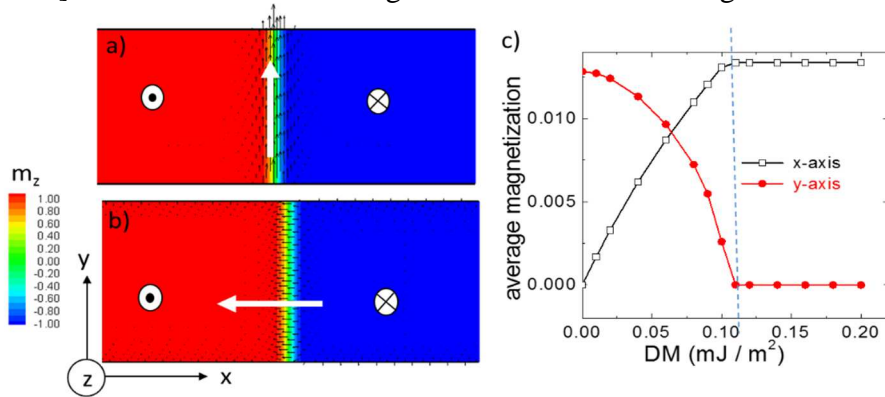


Fig. 2.6 Domain wall structure in 100-nm-wide Co track a) without DMI and b) with a DM constant of 2 mJ/m^2 . c) Transition between Bloch and Néel domain wall upon increasing the DM interaction monitored by the average magnetization of the sample.

Beside the change of the internal structure of the domain wall, the DMI is also responsible of the modification of the geometrical shape of the domain wall. In perpendicular magnetized nanotracks, the domain wall surface is expected to be perpendicular to the nanotrack axis to minimize the domain wall energy. However, the DMI can lead to a sizable tilting of the domain wall surface.

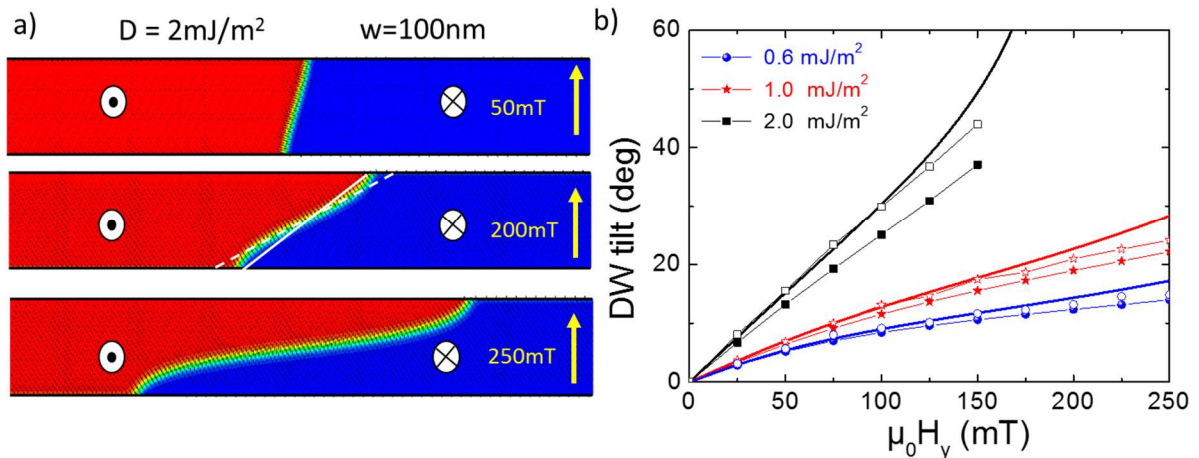


Fig. 2.7 a) Micromagnetic configuration of a 100-nm-wide Co track with $D=2 \text{ mJ/m}^2$ at various transverse fields. b) DW tilt angle as a function of $\mu_0 H_y$ for several values of D . Dots are the results of micromagnetic simulations (various definition of the tilt), whereas the continuous lines are the results of the collective coordinates model [*Boulle2013*].

The simplest way to induce the tilting is to apply a static in-plane magnetic field H_y transverse to the magnetic track (*Fig.2.7*). The domain wall is deformed by the transverse field but there is no effective displacement. We are discussing here about a static induced domain wall tilt. It is important to note that in the development of the domain wall tilt a major role is played by the Brown's boundary condition of the magnetization. The domain wall tilt has a monotonous increase with the transverse field and at a fixed H_y it increases with the DMI. Importantly, the slope of the DW tilting as a function of H_y depends directly on the value of D .

This provides a direct way to measure D , from the dependence of the DW equilibrium tilt angle on H_y .

In the presence of DMI, a tilt of the domain wall surface can also be induced dynamically by applying an easy axis external magnetic field H_z (Fig.2.8). The magnetization distribution in the nanotrack for different magnetic fields and $D=2\text{mJ/m}^2$ reveals that the DW tilts significantly in the steady state regime when driven by H_z . The steady-state tilt angle rapidly increases with H_z and D , although a saturation is observed for large H_z . The domain wall velocity along the track direction as a function of H_z for different values of D is shown in Fig.2.8d. As expected, the DMI leads to an increase of the critical Walker field. For large values of H_z , the DW velocity deviates significantly from the expected linearity as D increases. The domain wall tilt stabilization in time can take several nanoseconds and larger the track width, longer the stabilization time Fig.2.8c.

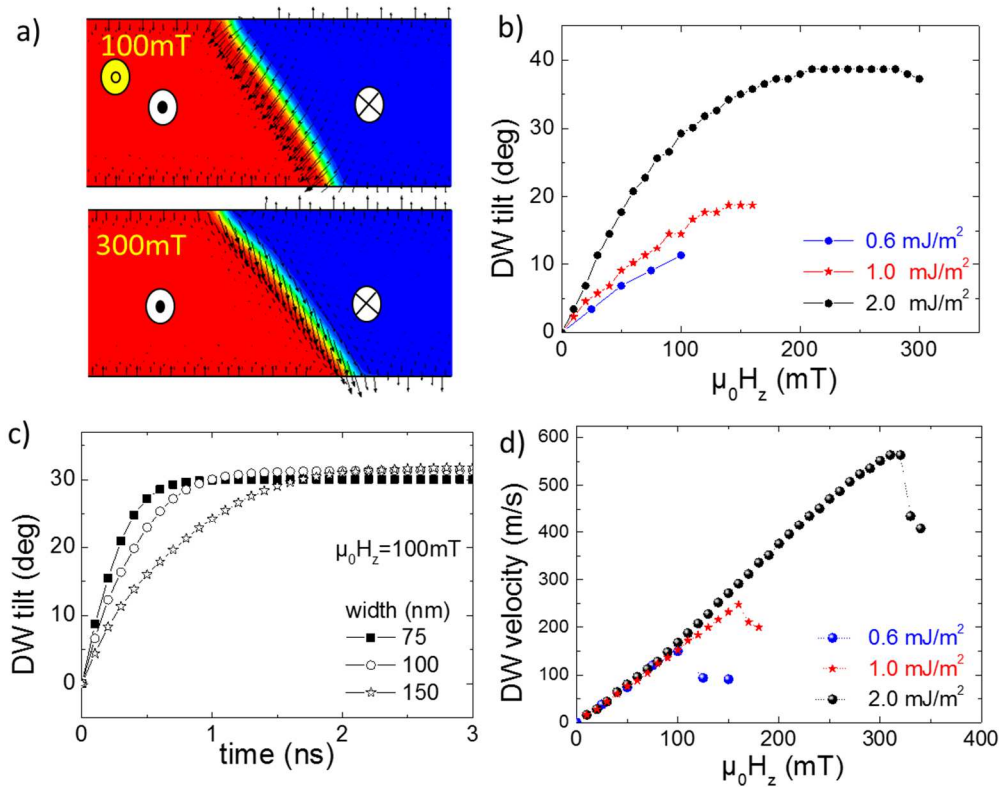


Fig. 2.8 Dynamics of the DW driven by an external magnetic field H_z for a 100 nm wide nanotrack. (a) Magnetization pattern of the DW for different values of H_z with $D=2 \text{ mJ/m}^2$. Tilt angle (b) and velocity (d) of the DW as a function of H_z for different values of D . (c) Time dependence of the tilt angle for $\mu_0 H_z = 100 \text{ mT}$ and different track widths with $D = 2 \text{ mJ/m}^2$.

It is important to remark also the way how the magnetization reversal occurs once the DMI interaction is taken into account (Fig.2.9). The simultaneous application of two magnetic fields (perpendicular H_z and transverse H_y) allows to reverse the magnetization from *up*-state to *down*-state. The reversal magnetization in normal ferromagnetic sample (no DMI) is mediated through the magnetostatic interaction and the reversed magnetic domain is nucleated in the middle of the sample. In this case two Bloch domain walls are created in the center and expelled symmetrically by the edges. In contrast in the chiral sample the nucleation of one single reversed magnetization domain is occurring at the left edge of the sample via the nucleation of a Néel like domain wall. The domain wall propagates along the y -direction being ejected at the opposed edge. These numerical predictions are consistent with the MOKE experimental observations [Pizzini2014].

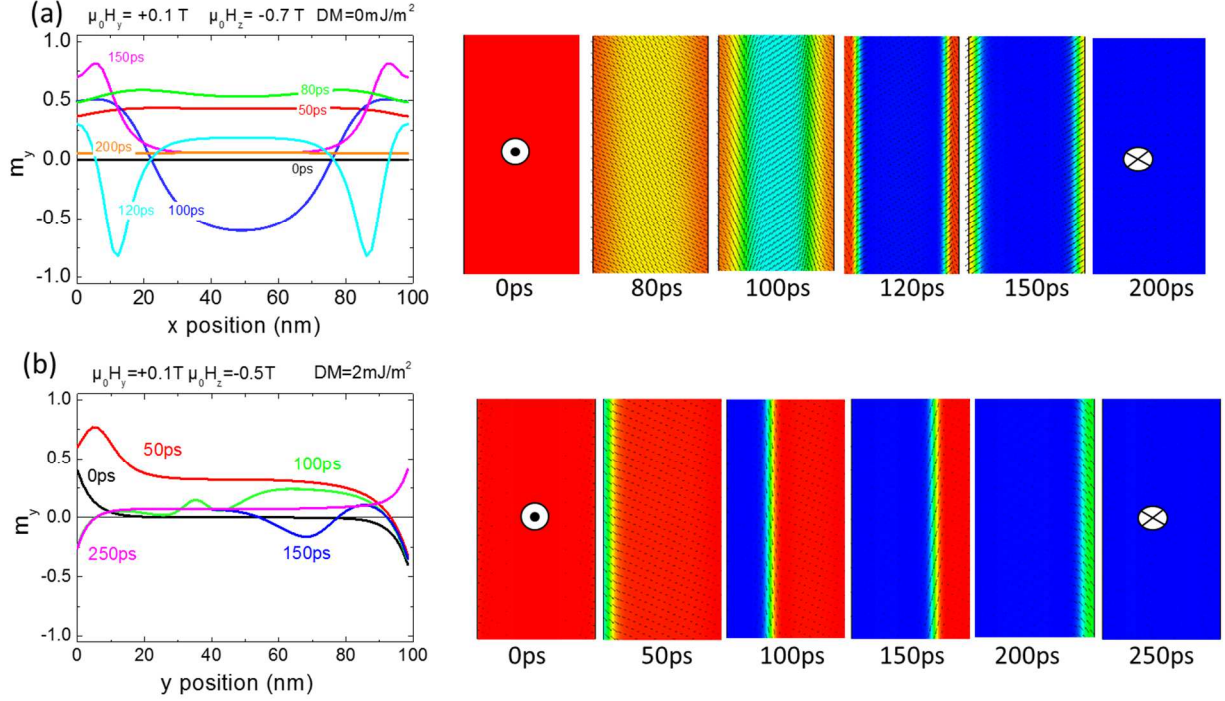


Fig. 2.9 Micromagnetic simulations showing the modification of the micromagnetic structure of the sample under the effect of two combined field H_y and H_z for a sample having a) no DMI and b) with $D = 2 \text{ mJ/m}^2$.

Many similarities might be found between the behavior of the chiral domain wall under perpendicular field and longitudinal injected current. The LLG equation has been modified by adding two torques related to the spin-orbit coupling : a *damping-like* and a *field-like* (eq. 1.34).

$$\frac{\partial \mathbf{m}}{\partial t} = -\gamma_0 (\mathbf{m} \times \mathbf{H}_{\text{eff}}) + \alpha \left(\mathbf{m} \times \frac{\partial \mathbf{m}}{\partial t} \right) + \gamma_0 C_{FL} J_{\text{app}} (\mathbf{m} \times \hat{\mathbf{y}}) + \gamma_0 C_{DL} J_{\text{app}} \mathbf{m} \times (\mathbf{m} \times \hat{\mathbf{y}})$$

Here $\hat{\mathbf{y}}$ is the unitary vector of the transverse direction and coincides with the polarization of the spin current flowing vertically from the Pt ($\parallel O_z$). The precise origin of these torques is still under debate but combines both spin Hall effect due to the current flowing in the nonmagnetic heavy metal layer (Pt) and Rashba spin-orbit coupling. It leads to an effective easy-axis magnetic field on the DW proportional $\sim C_{DL} J_{\text{app}} (\mathbf{m} \times \hat{\mathbf{y}})$ reaching a largest value on the core of the magnetic domain wall ($\parallel O_x$). Similarly the SOT tends to rotate the DW magnetization along the y -axis away from the Néel configuration, providing an additional source for the DW tilting. When injecting a current in the track, a fast DW motion is observed against the electron flow and the velocity increases with J_{app} and D . At the same time, a significant tilting of the DW occurs increasing with the current value and DMI. The velocity of the domain wall approaches the limit of 400m/s for the case of $D=2\text{mJ/m}^2$. At high current the tilt starts to be large and the structure of the DW is much distorted before entering in a more complicated dynamic regime. These numerical results are slightly affected by additional torques in LLG such as the *field-like* or common spin transfer torques (adiabatic and non-adiabatic)

This complete study show that the Dzyaloshinskii-Moriya interaction can lead to a tilting of the domain wall (DW) surface in perpendicularly magnetized magnetic nanotracks when DW dynamics are driven by an easy-axis magnetic field or a spin polarized current. The DW tilting affects the DW dynamics for large DMI, and the tilting relaxation time can be very large as it scales with the square of the track width. There is a simple way to estimate the DMI in magnetic multilayers by measuring the dependence of the DW tilt angle on a transverse static magnetic field. The tilt of the domain wall has been reported also by Riu et al [Ryu2013]

experimentally in the case of Pt/Ni/Co/Ni/Ta in perpendicularly magnetized nanotracks with SIA. The conclusions of our numerical study are valid also for these samples.

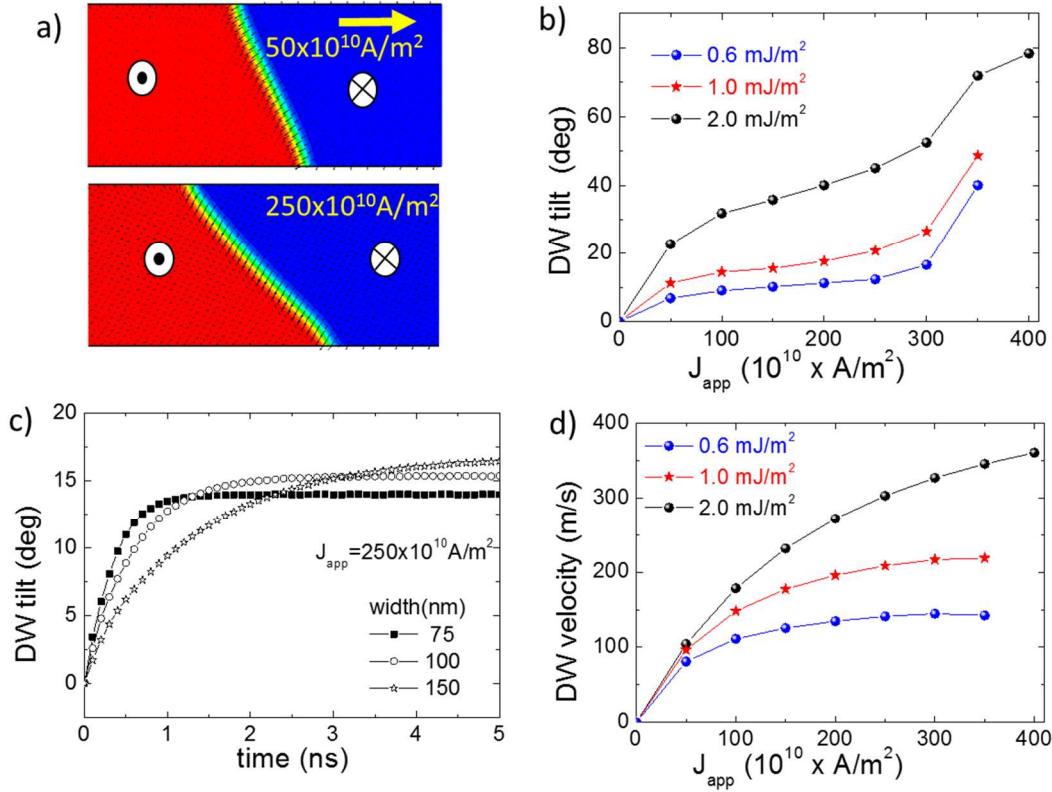


Fig. 2.10 Dynamics of the DW driven by the spin orbit torque ($\mu_0 H_{\text{So}} = 0.1 \text{ T}/(10^{12} \text{ A/m}^2)$) for a 100 nm wide nanotrack. (a) Magnetization pattern of the DW for $D = 2 \text{ mJ/m}^2$ and different values of J_{app} . The yellow arrow indicates the current direction. (b) Tilting and (d) velocity of the DW as a function of J_{app} for different values of D . (c) Time dependence of the DW tilt angle for different track widths for a current of density $0.25 \times 10^{12} \text{ A/m}^2$ applied at $t=0$ ($D=2 \text{ mJ/m}^2$).

One interesting case is the non-collinear configuration: the current flow is no longer restricted to a single direction of the nanotrack and can have any orientation within the film plane. Safeer et al. have studied by Kerr microscopy the spin-orbit torque-driven domain wall motion in Co/AlOx wires with different shapes and orientations on top of a current-carrying Pt layer (Fig.2.11a, [Safeer2015]). The displacement of the domain walls is found to be highly dependent on the angle between the direction of the current and domain wall motion, and asymmetric and nonlinear with respect to the current polarity (Fig.2.11b).

We have carried on micromagnetic simulations accounting both for *damping-like* and *field-like* terms in LLG for various orientation of the DC injected current with respect to the nanotrack axis. As previously, the motion of the DWs reaches a translation regime with a structure well stabilized (Fig.2.11c) and a velocity reported in Fig.2.11d. A clear asymmetry between the two current polarities is predicted in agreement with the experimental observations performed however with ns pulses of current instead of DC current. The velocity of the DW is varying non-linearly with the orientation of the current for positive current, instead the variation is linear for negative polarity (Fig.2.11c). One should note that our 100-nm large track is free of defects and this is not the case of real sample, the impact of the defects at large angle (proximity of 90°) might be important since the efficiency of SOT is substantially reduced for such angles.

For positive current, the *damping-like* torque has the largest efficiency for a configuration around 45° and since it is the responsible of the DW motion, this configuration

corresponding to the largest expected DW displacement. Once again the experimental observation could be well explained by symmetry considerations.

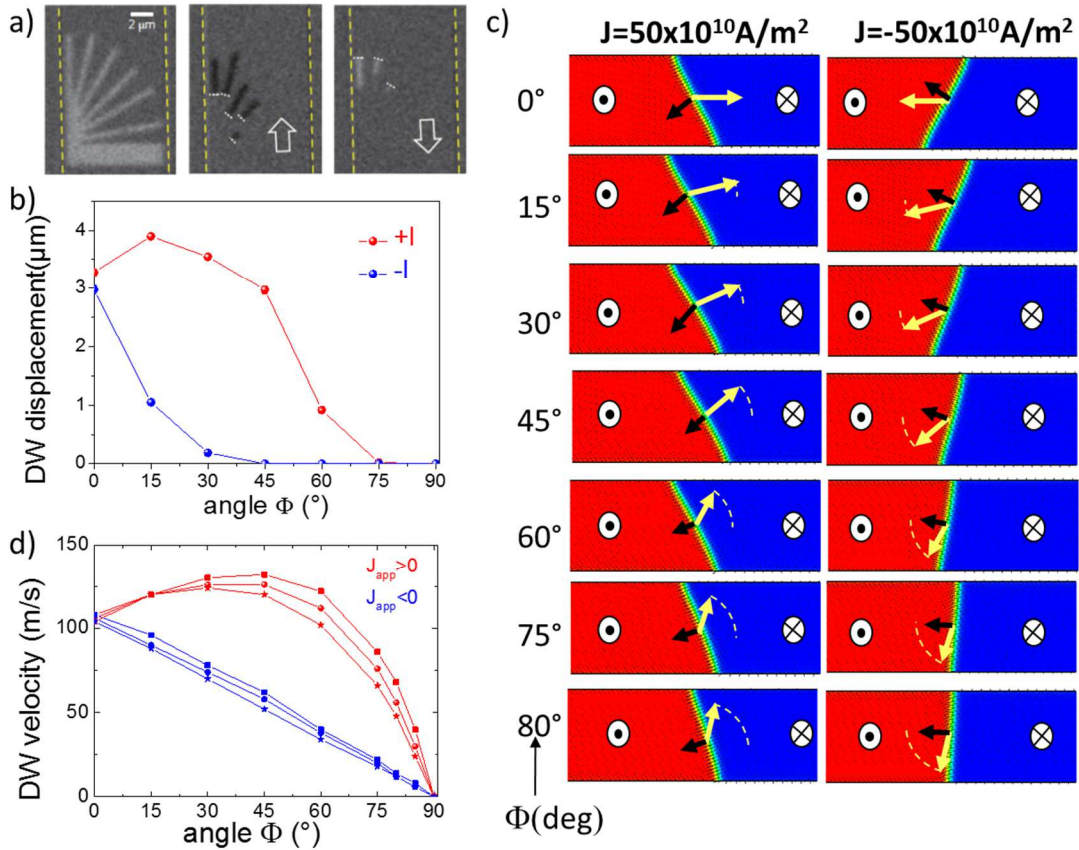


Fig. 2.11 a) Non-collinear domain wall motion. Differential Kerr microscopy images of the structure. Left: image corresponding to a saturated state with the magnetization pointing down. Middle: displacement of up/down domain walls after ten positive current pulses (2.62 ns at $1.75 \times 10^{12} \text{A/m}^2$). The white dotted lines show the initial positions of the domain walls in each wire, and the white arrow indicates the direction of the current. Right: displacement of up/down domain walls after ten negative current pulses (2.62 ns at $1.75 \times 10^{12} \text{A/m}^2$). For angles $>30^\circ$ we do not observe any domain wall motion. b) Domain wall displacements measured for a positive and negative series of ten current pulses (2.62 ns at $1.75 \times 10^{12} \text{A/m}^2$). [Saefer2015] c) The magnetization of the DW in the nanotrack for various non-collinear orientation of the injected current (yellow arrow). Black arrows indicates the magnetization in the DW center. d) Domain wall velocities according to micromagnetic simulation for both polarities.

To conclude this part related to the chiral magnetic domain wall, we turn now towards a special type of chiral object, namely the skyrmion. The very thin magnetic layers presenting chiral exchange interaction originating at the interface with a heavy metal or an oxide layer, are the suitable candidates to stabilize single skyrmions. Many studies are performed in order to investigate such a singular object and to finally have skyrmions at room temperature and take benefit of their properties for building application (e.g. logic devices). The topic is very reach, our first objective in this topic has been to image chiral domain wall and particularly a chiral bubble (Fig.2.12a,b). This has been possible in Pt/Co(1nm)/MgO. From micromagnetic point of view many simulations were done in order to approach as much as possible the size of the bubble imaged by XMCD-PEEM (Fig.12c,d). Material parameters such as the exchange constant, DMI and the magnetocrystalline anisotropy have been varied and the size of the circular chiral domain wall have been extracted and compared with the experimental observations (Fig.2.12c,d). The lateral confinement of the dot has a strong impact on the stability of the chiral bubble and this should be a key parameter of adjustment of the size of the

chiral bubbles. Moreover local variation of the interfaces or thickness layers might induce defects with an impact on the domain wall pinning.

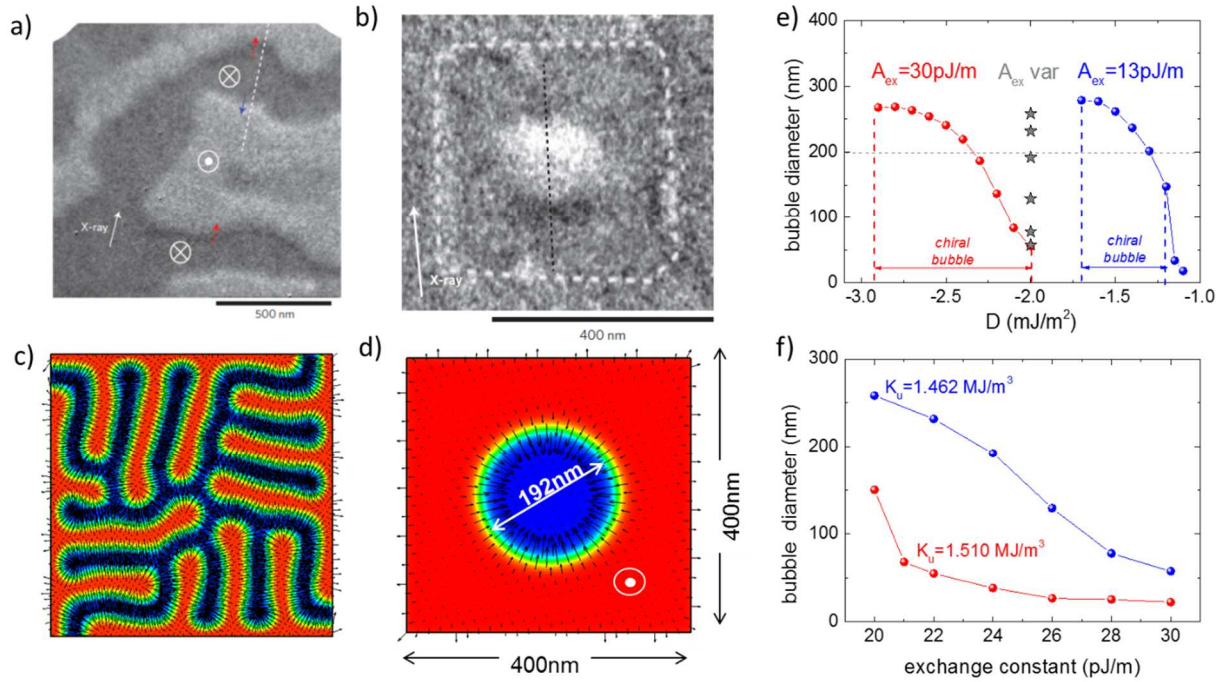


Fig. 2.12 a) Magnetic image of a multidomain state in a continuous Pt/Co/MgO film. For DWs lying perpendicular to the X-ray beam direction, thin white and black lines can be seen, corresponding to the magnetization being aligned antiparallel and parallel to the photon beam, respectively. This demonstrates their chiral Néel structure. b) Magnetic skyrmion observed at room temperature and zero external magnetic field by XMCD-PEEM in 420 nm square dot (indicated by the dotted line) [Boulle2016]. c) Stripe domains with Néel DW and d) a chiral bubble with a diameter of 192nm. Variation of the bubble diameter in a square dot of 400nm: e) upon changing the DMI (fixed K_u , several values of A_{ex}) and f) upon varying the A_{ex} (fixed D , several values K_u).

The interest on the magnetic domain walls evolved fairly fast and the rhythm is still accelerating these last years in view of potential non-volatile applications. The possibilities to adjust the properties of the domain walls and to control their motion arouses the imagination of the researchers in conceiving unique association of materials and combining ingeniously multiple phenomena. The story of the magnetic domain walls is still in progress. My contribution to the field shed some light on the domain wall dynamics and their interaction with spin-polarized currents.

Chapter III: Spin-torque nano-oscillators

The idea to use the spin angular momentum transfer to excite steady-state precession of the magnetization is developed around two types of samples: nanopillars and nano-contacts. In the auto-oscillatory state the magnetization of the free layer might evolve almost uniformly in the space or develops in highly complex manner (vortex gyration, bullet mode,...). My activity concerns STNO based on nanopillars with lateral sizes below 100nm having the magnetization of the free layer more or less uniform. The magnetization of the free layer is laying in the plane of the dot while the polarizer layer was fixed either perpendicular to plane or in the plane. The RF properties of STNO were studied by modelling upon injecting a DC spin polarized current alone or combined with a static magnetic field. The STNOs are intrinsically non-isochronous oscillators and this feature has great impact on the STNO operation either in free running or forced regime (synchronization, modulation). These properties were studied numerically using macrospin and/or micromagnetic approaches as well as analytical models.

Future wireless communications demand new RF devices with low power consumption, which are compact and multifunctional. Spin torque nano-oscillators (STNOs) use the spin transfer torque (STT) effect in thin magnetic nanoelements to induce steady state oscillations via spin angular momentum transfer from the conduction electrons to the local magnetization. These magnetic oscillations are then converted into an oscillatory output signal at frequencies from 100MHz to several tens of GHz depending on the STNO type. STNOs have been identified as a promising class of RF devices for applications in wireless communication as well as read heads. This is due to their sustained microwave frequency oscillations and their large frequency tunability by the injected DC current and the applied field, as well as their large agility which allows for a fast modulation of the STNO output. In addition, STNOs are highly compact due to their nanoscale dimension and compatible with complementary metal-oxide semiconductor (CMOS)

The operating principle of STNOs combines two phenomena: spin transfer torque (STT) to set the magnetization into auto-oscillation, and the magnetoresistance (MR) to produce an output voltage (Fig. 3.1).

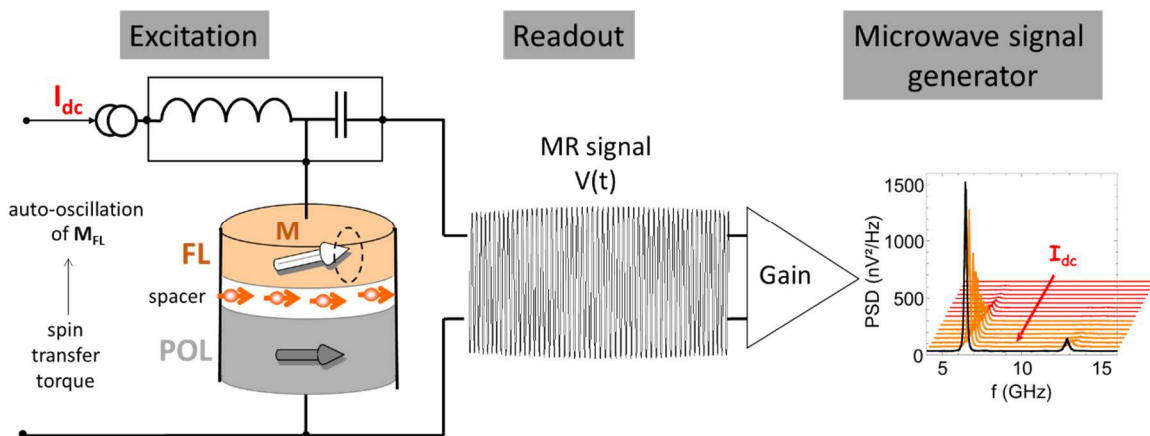


Fig. 3.1 Building blocks of a STNO: excitation via an injected current, readout signal and the microwave signal generator.

The properties of the microwave signal generator are controlled by the properties of the nanopillar. The STNOs might be classified with respect to relative orientation of the magnetization of the active layers (Fig. 3.2): perpendicular STNO having the polarizer pointing

out-of-plane perpendicularly to the magnetization of the free layer (a); planar STNO having the magnetization of both active layers laying in the plane (b). From the point of view of relevance of the assumptions, the models are supposing that only the magnetization of the free layer is allowed to move (a, b) or all the layers of the structure are interacting and collectively evolve in time (c). We concentrated our efforts on samples having the magnetization of various layers in single domain state in contrast with other research teams interested by the case of vortex based oscillators [Pribiag2007, Mistral2008]. The main raison of this choice is supported by the potential use of STT oscillator in the range of high frequency (10 of GHz) while the vortex oscillators are operating at lower frequency (< 1GHz).

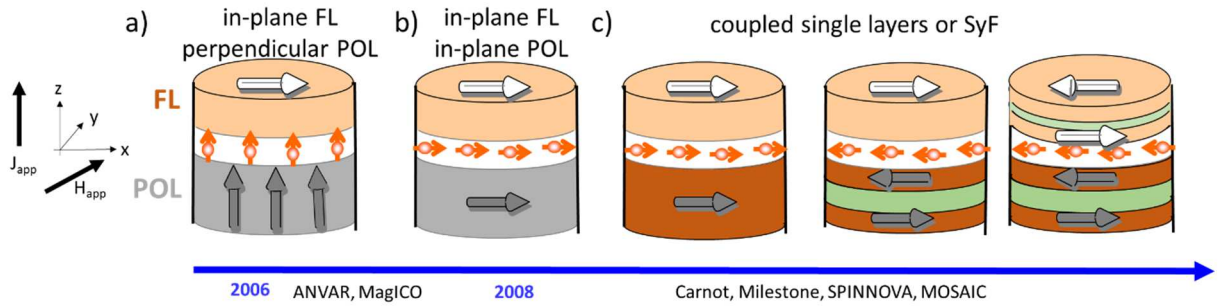


Fig. 3.2 Schematics of typical STNO nanopillar structures. The free layer magnetization (FL) is laying in xOy plane while the magnetization of the reference layer (polarizer POL) is fixed either perpendicular to plane (a) or in the plane of the dot (b). c) The polarizer might be free to evolve being coupled to the free layer, or even replaced by a synthetic anti-ferromagnet. Bottom : time scale of STNO topic at Spintec and the associated grants.

Depending on the specificity of each sample, various kind of steady states might be stabilized once the injected current is swept. In an auto-oscillation state the magnetization of the free layer describes 3D trajectories with almost constant energy either in the plane (IPP, Fig. 3.3a) or out-of-plane (OPP, Fig. 3.3b). If the magnetic layers are coupled such as the case of a synthetic antiferromagnet (SAF) structure both layers are describing IPP like trajectories with different amplitudes. Even that the symmetry of the trajectories looks very different, a unified description might be used namely “non-linear auto-oscillator theory” (called hereafter KTS model [Tiberkevich2008, Slavin2009]).

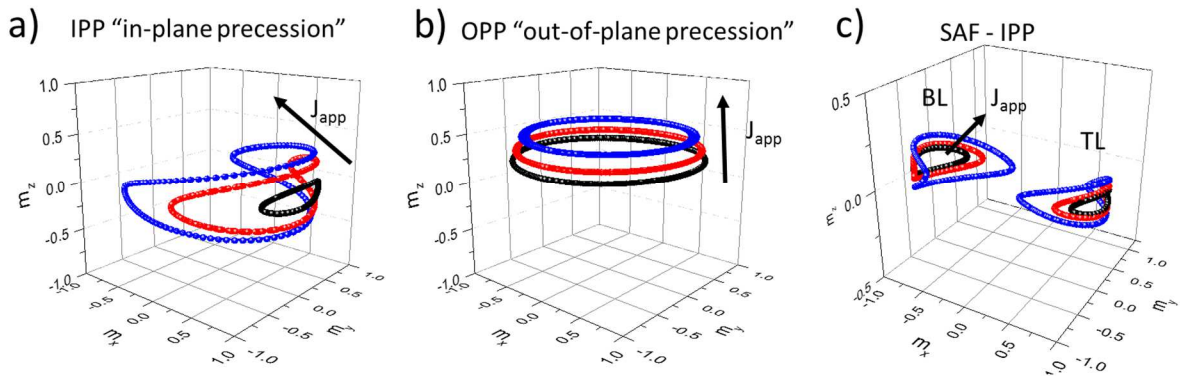


Fig. 3.3 Magnetization trajectory in 3D space corresponding to a) an in-plane precession (IPP) and b) an out-of-plane precession (OPP). c) Trajectories of a synthetic antiferromagnet structure corresponding to an IPP mode.

To address in a simple and general way the STNO is convenient to change the variables, replacing the unitary magnetization vector $\mathbf{m} = (m_x \ m_y \ m_z)$ by a complex variable c and its complex conjugate c^* . The phenomenological LLG (eq. 1.28) including the spin transfer torque (eq.1.32) is transformed in an equivalent form:

$$\frac{dc}{dt} + j \frac{d\mathcal{H}}{dc^*} + \mathcal{F}_c = 0 \quad (3.1)$$

where \mathcal{H} is the hamiltonian. \mathcal{F}_c is the dissipative contribution, the sum of a positive contribution from the Gilbert relaxation proportional with the damping constant α and negative contribution from the STT, proportional with the injected current. The hamiltonian is diagonalized and the dissipative term has a linear and a quadratic contribution only:

$$\frac{dc}{dt} + j\Omega(p)c + \Gamma(p)c = 0 \quad (3.2)$$

where the complex variable is $c = \sqrt{p}e^{-j\phi}$, p is the power and ϕ is the phase of the oscillator. The two functions $\Omega(p) = \omega_0 + Np$ and $\Gamma(p) = \gamma + Qp$ are both usually restricted to a linear dependence on the power p . ω_0 and γ are the linear hamiltonian and dissipative coefficients, N and Q are the corresponding non-linear coefficients. The precise values of all these coefficients are depending on the internal properties of the free layer (spontaneous magnetization, anisotropy, size,..) and related with the spin polarized current properties (amplitude, polarization,..). The general c -equation (3.2) allows to derive the following power and phase equations:

$$\frac{dp}{dt} = -2\Gamma(p)p \quad (3.3a)$$

$$\frac{d\phi}{dt} = \Omega(p) \quad (3.3b)$$

describing in a general formalism most of the features of the STNO. The trajectories of the magnetization corresponding to the steady state are simply the solution of *eq. 3.3a*. One can identify easily the required conditions (current, field) to reach an auto-oscillation state, establishing state diagrams, deriving the stable trajectories and the tuning of the frequency by non-linear phase-amplitude coupling.

As a synthesis of all the modelling studies performed on a large variety of STNO samples, three main objectives might be identified:

1. existence of auto-oscillation states : compulsory conditions of excitation (field, current,...) to establish a steady precession of the magnetization;
2. expected properties of the auto-oscillation states: dispersion diagrams;
3. understanding the mechanism behind the auto-oscillation by simple models.

The following subsections are illustrating the operation of uniformly magnetized STNO, the understanding of various properties and their utility for applications.

3.1 STNO with perpendicular polarizer

The concept of perpendicular STNO was initiated at Spintec in 2006 by U. Ebels and B. Dieny based on several patents [*US6532164B2*, *US8063709B2*] and since supported by several research grants. This reciprocal perpendicular configuration is the most suitable since it maximizes the efficiency of the spin angular moment transfer $\sim \mathbf{m} \times \mathbf{p}$, \mathbf{m} and \mathbf{p} being perpendicular vectors, (*Fig. 3.2a*). Macrospin modelling confirms the possibility to excite steady-state oscillation once the injected current is above the critical value (J_{c1}). The magnetization describes trajectories almost circular out-of-plane (*Fig. 3.4*, OPP) and progressively goes toward the out-of-plane saturated state upon reinforcing the injected current (OPS above J_{c2}). The two OPP regions on the JH state-diagram (*Fig. 3.4a*) are that of interest for application and particularly the possibility to have such auto-oscillation without supplying any extern magnetic field is very

appealing. Indeed for this last case, the frequency of the auto-oscillator can be tuned in the range of GHz by adjusting the current (*Fig. 3.4b*), a continuous dependence of the frequency on the injected current is predicted by macrospin approximation. Practically, one wants to have as large as possible operation window meaning small J_{c1} and large J_{c2} . The first critical current is controlled mainly by the in-plane anisotropy of the free layer [Ebels2008]:

$$J_{c1} = \pm \frac{2e}{\hbar} \frac{\mu_0 M_s t}{g(\eta, \theta = 90^\circ)} \frac{H_K}{2}$$

damping parameter:
$$J_{c2} = \pm \frac{2e}{\hbar} \frac{\mu_0 M_s t}{g(\eta, \theta = 90^\circ)} \alpha \left(M_s + \frac{H_K}{2} \right)$$

with M_s the saturation magnetization, t - the thickness of the free layer, H_K - the in plane anisotropy field, $g(\eta, \theta = 90^\circ)$ the pre-factor of the STT term. To maximize the operation window samples having an enhanced damping are suitable. However, the tunability of the STNO is damping dependent, the frequency being inverse proportional with the damping of the free layer:
$$f = \frac{\gamma_0}{2\pi} \frac{\hbar}{2e} \frac{g(\eta, \theta = 90^\circ) J}{\mu_0 M_s t \alpha}.$$

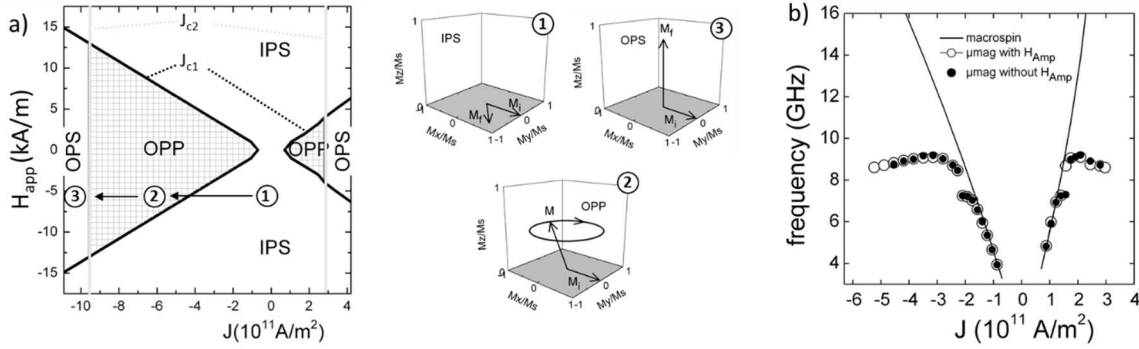


Fig. 3.4 a) Current-field state diagram as deduced by macrospin simulation with the associated states IPS, OPP and OPS b) Frequency dispersion versus injected current in zero applied field [Firastrau2008].

Several features predicted by the macrospin approach are however invalidated by micromagnetic modelling. Especially at high current, the values of frequency saturate below 10GHz while the macrospin approach indicates their continuous increase (*Fig. 3.4b*). The main reason of this discrepancy between models is originating in the possibility of the magnetization distribution to deviate from the uniform state. Even that the lateral size of the pillar is smaller than 100nm, the magnetization has the possibility to develop domain-like structures located on the edge of the sample (*Fig. 3.5*). At low current, both models are converging since the magnetization is almost uniform having a coherent rotation. At intermediate current, the magnetization is partially reoriented out-of-plane in two domains on the edge are stabilized as a compromise between the demagnetizing effects and spin transfer torque. The size of these edge domains progressively grows and finally the magnetic domains collapse by nucleating a vortex-like structure with stops the auto-oscillation regime. The non-uniformity of the magnetization is reducing the slope df/dI being detrimental for the agility of the oscillator. At very high currents the magnetization dynamics becomes very complex with multiples vortices, this being also in contradiction with the macrospin model with predicts out-of-plane stable state.

The impact of various parameters on the auto-oscillator properties was further studied mainly by micromagnetic simulation. Upon increasing the damping of the free layer the frequency is shifted downwards in the regime of coherent rotation as predicted by macrospin model (*Fig. 3.6a*). However the saturation of the frequency at high current is less sensitive to the damping indicative that non-uniformity of the magnetization is responsible of the

degradation of the *RF* properties. In contrast, by changing the cross-section size of the nanopillar, it is possible to play on the frequency saturation threshold. A shape quasi-circular is the most suitable allowing to extend the operation window and reach higher frequencies (*Fig. 3.6b*). As supplemental verification of the pertinence of the numerical results, the numerical auto-oscillations have been studied by two micromagnetic solvers *Micro3D* (FDM) and *FeeLLGood* (FEM) based on different numerical approaches (*Fig. 3.6c*). The frequency dispersion curves are very close despite to some differences inherent to the numerical methods.

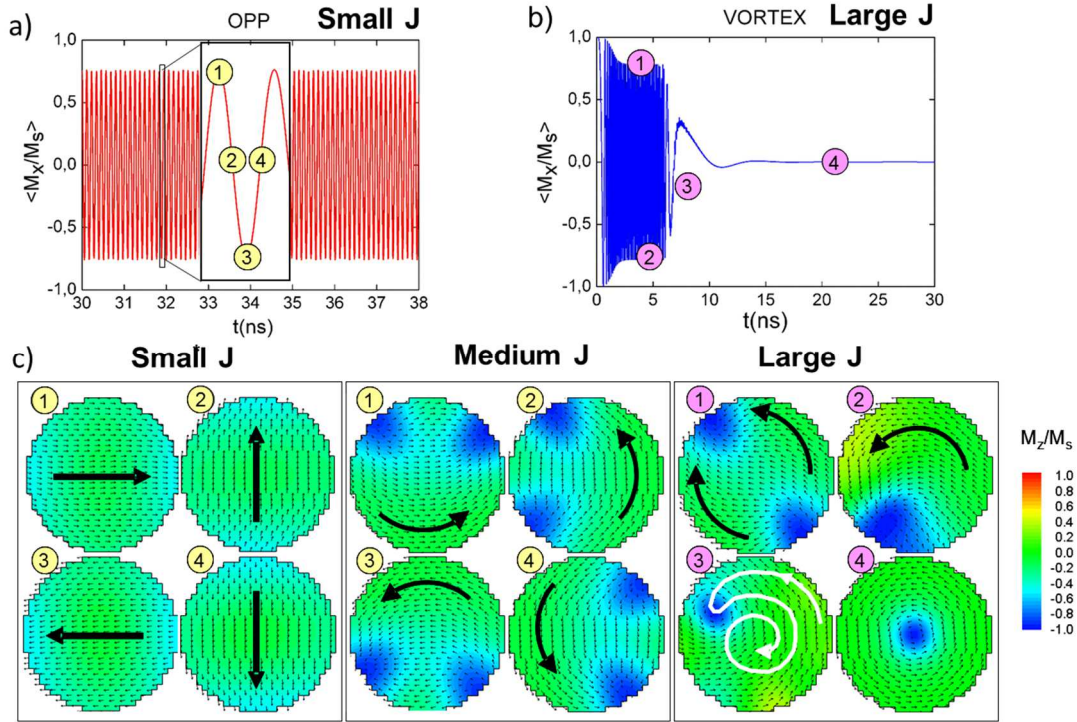


Fig. 3.5 a) Time trace of the magnetization at small current in a OPP steady-state (a) and large current with a vortex-like nucleation (b). The corresponding snapshots of the magnetization or three current levels (c). [Firastrau2008].

The experimental studies carried by D. Houssameddine show that the frequency of the excited mode has several similarities with the numerical predictions (*Fig. 3.6d*): a first regime with increasing frequency followed by a frequency saturation regime. However the experimental frequency is still twice time lower than the numerical expected value even after adjusting most of the parameters of the sample, including the magnetic field generated by the current itself (Oersted field) and the stray field yielded by the polarizer. Our modelling deals only with the free layer magnetization but the experimental samples are more complex that the simplified structure (*Fig. 3.2a*). From the MR detection point of view the symmetry of the OPP steady-state trajectory is not allowing to have large enough signal since the variation of the magnetization component parallel with the magnetization of the polarizer (POL) is very small. In purpose, additional magnetic layer is included in the nanopillar on top of FL having an in-plane magnetization used as *analyzer*, thus the MR signal is substantially increased and the auto-oscillation state easily monitored. As a first action of the analyzer on the sample response, one might mention the necessity to apply an external bias field to compensate the dipolar field yielded on the free layer by the analyzer (*Fig. 3.6d*). Moreover, a second action of the analyzer is less obvious and involves the spin dependent transport since the analyzer contributes to the spin polarization of the current on equal foot with the perpendicular polarizer. Indeed some experimental results are indicative of the existence of a current driven mode compatible with an in-plane polarizer. Trying to include everything in the model requires to have a complete

characterization of the sample and unfortunately many of the unknown parameters are technically very difficult even impossible to extract.

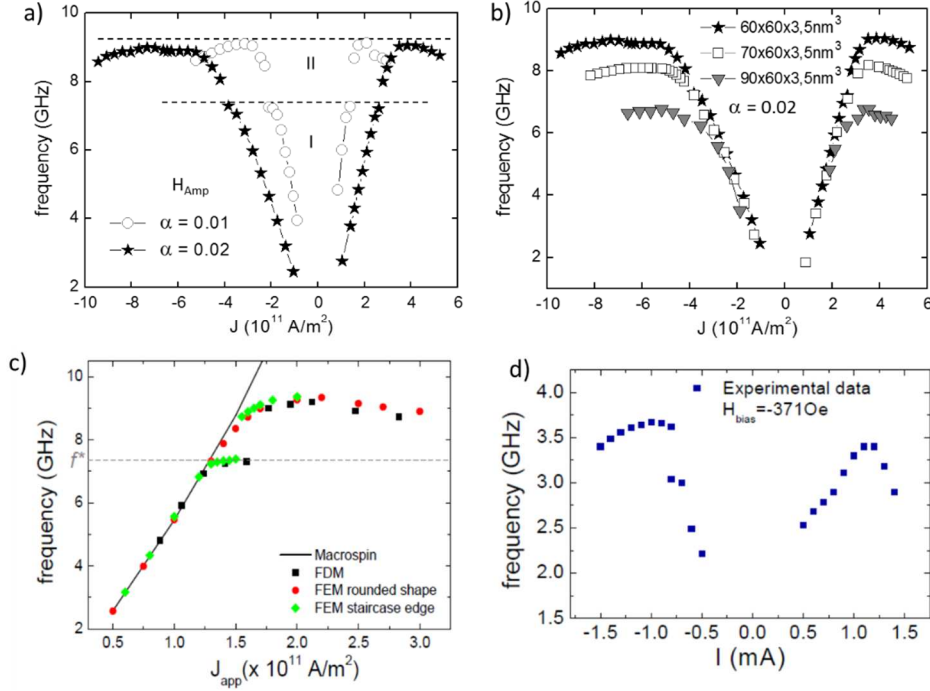


Fig. 3.6 Frequency dispersion impacted by the damping parameter (a) and by the sample size (b) [Firastrau2008]. c) Frequency dispersion as predicted by various numerical approaches [VayssetPhD]. d) Experimental frequency dependence on the injected current [Houssameddine2007].

As conclusion of this section one might keep three messages:

- the main features of OPP auto-oscillator are described easily by the macrospin approach;
- the use of micromagnetic modelling is mandatory to explain some operation regimes in which the macrospin fails;
- some strategy of optimization for the STNO are clearly identified.

3.2 STNO with planar polarizer

In order to improve the amplitude of the MR signal the full metallic GMR samples are replaced by samples based on magnetic tunnel junction (MTJ). However the resistance area product (RA) of such devices must be relative low in order to support the injection of high current densities. At Spintec the study of RF properties of such MTJ based STNO was initiated during the PhD of D. Houssameddine working on samples provided at that time by Hitachi. The magnetization of the free layer is collinear with the magnetization of the polarizer (Fig. 3.2b), both active layers being magnetized in the plane. For such geometry, the general model of the auto-oscillator (eq. 3.1) in the limit of macrospin approximation predicts a critical current value

$$J_{c1} = \alpha \frac{2e}{\hbar} \frac{\mu_0 M_s t}{g(\eta, \theta = \pi)} \left(H_K + H_{app} + \frac{M_s}{2} \right)$$

to initiate an in-plane precession around the equilibrium position. At a fixed value of the current the frequency dependence on the applied field follows a typical Kittel law:

$$f(H_{app}, J) = \frac{\gamma_0}{2\pi(1+\alpha^2)} \sqrt{(H_K + H_{app})(H_K + H_{app} + M_s)} + F(J, \alpha)$$

with the last term $F(J, \alpha)$ accounting for the current dependence.

After patterning circular or elliptical shape pillars, two kinds of samples are identified: HTMR samples with high resistance and high TMR (100%), and LTMR samples with low resistance and low TMR (30%). The lower MR performance of LTMR devices is caused by defects in the tunnel barrier. The RF characteristics of LTMR and HTMR devices are very distinct (*Fig. 3.7*). The linewidth of LTMR devices can be as low as 10MHz whereas the linewidth of HTMR samples is larger than 100 MHz. The plots of the frequency and the linewidth as a function of field are shown in *Fig. 3.7a* for both types of sample at current larger than the critical current. Frequency increases with the applied field, as predicted by the Kittel model [*Kittel1948*]. The most striking feature of these plots is the existence of several *branches* (labeled as A, B, C and D). For LTMR sample, the frequency changes abruptly at several field values. This is particularly visible on the second harmonic. Moreover, these frequency jumps are correlated with linewidth maxima. The large linewidth value at the frequency discontinuities is likely due to the presence of two peaks in the Fourier spectrum that blend together. On the plot corresponding to an HTMR sample, the frequency discontinuities are less visible. However, the large increase of linewidth at some field values is evidence of a similar underlying behavior. The correlation between linewidth and frequency jumps shows that the origin of the different branches has to be understood to control the coherence of STOs. Reducing the linewidth is necessary for applications and therefore the frequency jumps have to be avoided.

Analyzing alone the free layer current driven dynamics in the framework of macrospin approximation fails in explaining the features experimentally observed: several modes excited by the STT. The first step in the modelling is to allow the magnetization developing inside the free layer in a non-uniform distribution. This was done during the PhD thesis of A. Vaysset. In *Fig. 3.7c* the frequency dependence on the in-plane applied field is reported as predicted by micromagnetic modelling. Upon increasing the injected current the frequency is deviating from the Kittel law and different modes are clearly identified. In order to get rid of numerical artefacts related to the regular mesh (drawback intrinsic to finite difference method) various cross checking between FDM and FEM micromagnetic solvers were carried out. The existence of different modes is confirmed very similar to the experimental observations. The micromagnetic simulation results reported are obtained using a FEM solver (FeeLLGood) in collaboration with J-Ch. Toussaint from Institute Néel.

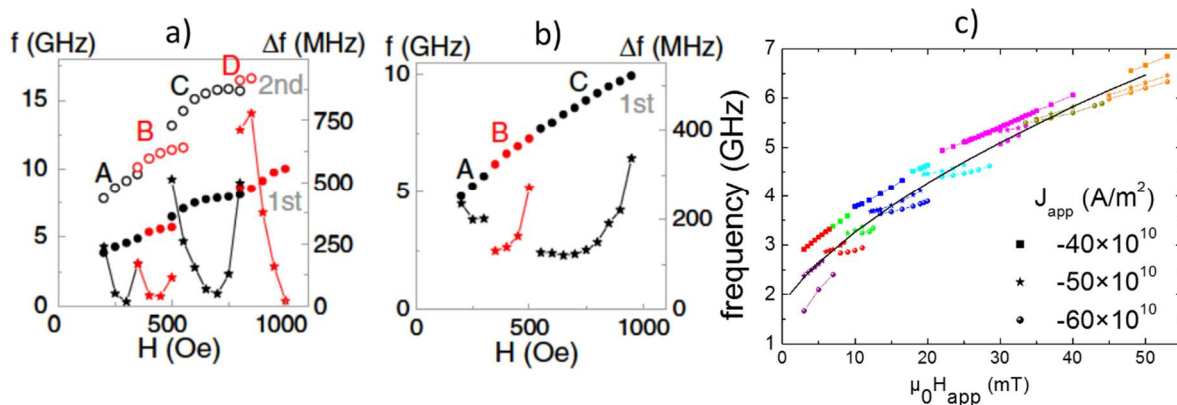


Fig. 3.7 a) Frequency vs. bias applied field measured for a) LTMR sample (both 1st and 2nd harmonics are shown by dots) and b) HTMR sample. The linewidth of the 1st harmonic is plotted as stars [Houssameddine2008]. c) The frequency vs. applied field as predicted by micromagnetic simulation for several injected current. The values given by macrospin approach are plotted by the continuous line [VayssetPhD].

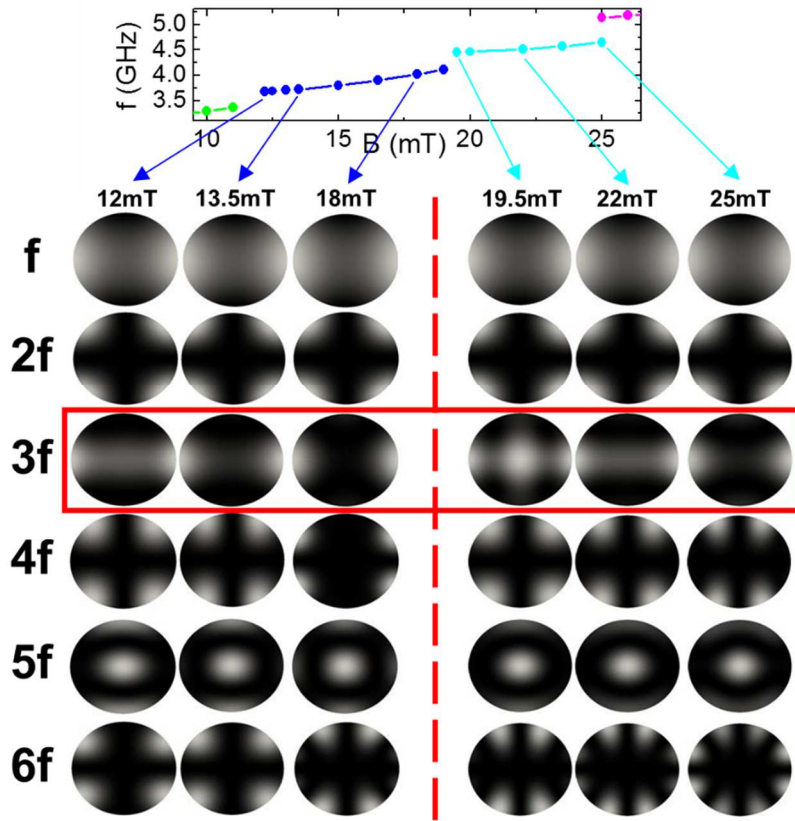


Fig. 3.8 Spectral maps at $J = -5 \times 10^{11} \text{A/m}^2$ for two adjacent branches. For each harmonic, the first line contains the maps obtained for m_x (longitudinal component). The regions in white give the largest contribution to the power of the corresponding peak [VayssetPhD].

The micromagnetic spectral mapping technique allows to clearly show that each branch is associated with a different mode, various regions of the sample are differently excited for each point inside a branch. Our first main numerical observation identify the contribution $3f$ ($6f$) as being the biggest difference between the branches.

In a system where oscillations are small deviations from the equilibrium state, it is possible to decompose the magnetization motion on a basis of eigen-modes (or normal modes). These eigen-modes are derived in the limit of small oscillations. Several techniques exist to compute the micromagnetic normal modes of a ferromagnetic sample, we have used for our study the software Spinflow. The eigen-modes are shown on Fig. 3.9 with the eigen-frequencies plotted as a function of applied field. On the same figure, the frequencies of IPP harmonics are plotted for $J = -5 \times 10^{11} \text{A/m}^2$. One would expect the eigen-modes to be the "perturbation modes" excited at the beginning of each branch. Thus, the curve of $3f$ (or another harmonic frequency) would cross an eigen-frequency at the beginning of each branch. The reality is more complex. First, the excited modes cannot be clearly identified as deriving from eigen-modes. Second, it seems that the modes excited at the beginning of each branch have a strong variation of their longitudinal component, as shown by the spectral maps (Fig. 3.8 at $4f$). Therefore, these perturbation modes are not normal modes but nonlinear modes. Currently, no theory is available allowing to check the frequency of these nonlinear modes.

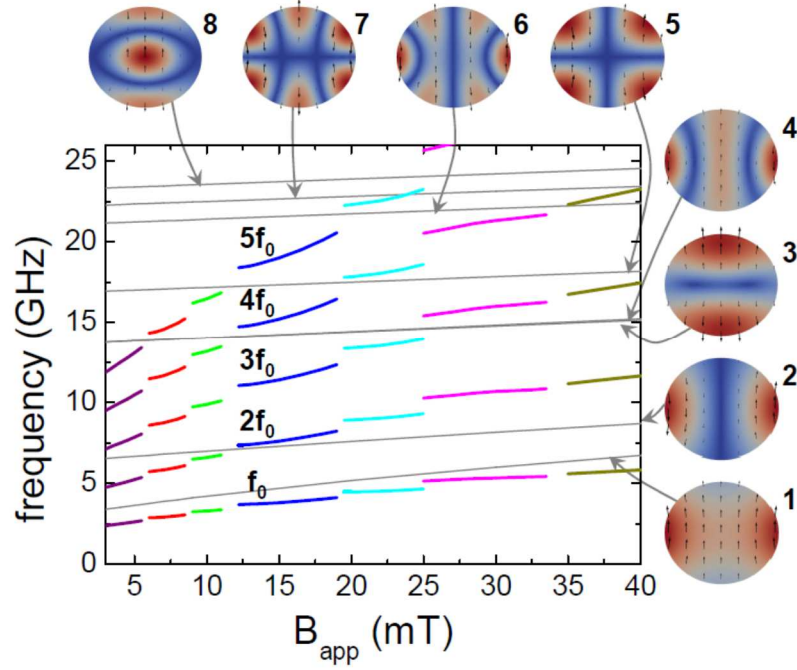


Fig. 3.9 Configurations: free layer eigen-modes. f vs B_{app} : eigen-frequencies (in grey) and harmonic frequencies at $J_{app} = -5 \times 10^{11} \text{ A/m}^2$, same colors as in previous figures). [VayssetyPhD]

To summarize, when the field (or the current) is varied, the oscillation frequency is also varied in a non-continuous manner. Jumps in frequency have been confirmed by two different numerical methods (FDM, FEM). They are accompanied by minor variation of the shape of the average magnetization trajectory but the various contributions to the free energy are showing discontinuities for any current larger than the critical current. Using the micromagnetic spectral mapping technique, the origin of the jumps has been clarified. After each discontinuity, at the beginning of a branch, a mode is strongly excited at the frequency $3f$. This mode is nonlinear as the variation of its longitudinal component is large, and therefore its pattern does not clearly match the configuration of any of the linear eigen-modes computed with Spinflow. It is thought that a frequency jump appears when the curve $3f$ crosses the natural frequency of the excited non-linear mode. Thus, the series of "band gaps" observed in the Fig. 3.7c would give an indication about the frequency of the non-linear modes as a function of applied field. The simulations show that oscillations of a single layer can already lead to very complex dynamics.

3.3 Synchronization of STNO with planar polarizer

From practical point of view, one of the main issues that remains to be addressed for these spin transfer torque oscillators is their relative large linewidth (\sim tens of MHz) originating mainly from the phase noise. One possibility to reduce the linewidth is to couple either different layers within an oscillator (see section 3.5), or to couple several oscillators. For this second case, several options were proposed, experimentally and theoretically as: current mediated coupling [Georges2008, Grollier2006], dipolar coupling [Urazhdin2010, Belanovsky2013] or spin wave coupled nanocontacts [Sani2013, Rippard2005]. As a first step to understand the conditions for an efficient synchronization we addressed the synchronization of a STNO to an external microwave source: either an RF current $I = I_{DC} + I_{RF} \cos(\omega_{ext} t)$ or an RF magnetic field $\mathbf{H}_{app} = \mathbf{H}_{DC} + \mathbf{H}_{RF} \cos(\omega_{ext} t)$.

The synchronization of the STNO by a microwave current was initiated at Spintec during the PhD of M. Quinsat and continued during the PhD thesis of C. Dieudonné, while the synchronization via an RF magnetic field was addressed by the PhD thesis of J. Hem. Support was provided by the I. Firastrau, D. Guskova and M. Tortarolo. We focus our research on standard homogeneous in-plane magnetized oscillators (in-plane polarizer and in-plane free layer), for which an in-plane precession (IPP) mode is stabilized. Starting from the existing theoretical descriptions, based on spin wave theory of spin torque oscillator, we have addressed in a general manner the synchronization.

The Landau-Lifshitz-Gilbert equation including the spin transfer torques (i.e. *damping-like* and field-like) is a vectorial equation and the RF excitation arises from 6 terms: $\mathbf{m} \times (\mathbf{m} \times \mathbf{u}_i)$ and $\mathbf{m} \times \mathbf{u}_i$ with \mathbf{m} – unitary vector of the magnetization and \mathbf{u}_i – unitary vector of the axis $i=x,y,z$. After several transformations taking advantage of their properties of linearity, one might show that these 6 terms generate 4 different forcing terms $F_{sync}c$ whatever the nature of the RF signal, acting in the following general c -equation (eq. 3.2):

$$\frac{dc}{dt} + j\Omega(p)c + \Gamma(p)c = F_{sync}c$$

The forcing terms $F_{sync}c$ are listed in the table below.

RF excitation origin	Irreducible form F_{sync} $A,B,C,D \in \mathbb{R}$	Additional phase shift ψ_0
$\mathbf{m} \times (\mathbf{m} \times \mathbf{u}_x)$	$A_1(p)\cos \psi_{2n} + jA_2(p)\sin \psi_{2n}$	0
$\mathbf{m} \times \mathbf{u}_z$	$C_1(p)\cos \psi_{2n+1} + jC_2(p)\sin \psi_{2n+1}$	0
$\mathbf{m} \times (\mathbf{m} \times \mathbf{u}_y)$		
$\mathbf{m} \times \mathbf{u}_x$	$j(B_1(p)\cos \psi_{2n} + jB_2(p)\sin \psi_{2n})$	$\pi/2$
$\mathbf{m} \times \mathbf{u}_y$	$j(D_1(p)\cos \psi_{2n+1} + jD_2(p)\sin \psi_{2n+1})$	$\pi/2$
$\mathbf{m} \times (\mathbf{m} \times \mathbf{u}_z)$		

The geometrical origin of the forcing term leads to a different synchronization ratio (even $2n$ or odd $2n+1$) and prefactor (j or 1). A consequence of the complex nature of the prefactor relates the additional phase shift ψ_0 , which is the phase shift in the synchronized state at zero detuning. Up to now, ψ_0 was known to be only dependant of $\pm \arctan(\nu)$ with ν the non-linearity of the oscillator. Here we observe a supplementary phase shift of $\pi/2$ if the prefactor is imaginary. One potential result would be to combine different forcing terms to continuously shift the phase over 2π while the system stays at the centre of the locking range to resist the influence of thermal noise.

As an illustration, *Fig.3.10* summarizes the comparison between the extended analytical model and numerical macrospin simulations. For the sample schematically presented on *Fig.3.10a*, two important cases namely field synchronization at $2f$ across $\mathbf{m} \times \mathbf{u}_x$ with $B_1(p), B_2(p) \neq 0$ and current synchronization at $2f$ across $\mathbf{m} \times (\mathbf{m} \times \mathbf{u}_x)$ with $A_1(p) \neq 0$ are reported. The macrospin simulations allow to monitor the evolution of the generated frequency f_g of the oscillator once the frequency of the external control parameter f_{ext} is swept. A frequency locking occurs each time when the external RF source frequency f_{ext} is a multiple of the free-running frequency of the oscillator ($1f, 2f, 3f, \dots$). One might notice that the $2f$ synchronization is particularly efficient both for current and longitudinal field cases, this feature being intrinsic to the IPP steady state oscillations. With respect to the geometry of the sample and the symmetry of the excitation some fast oscillating terms become resonant at $2f$ having a big impact on the magnetization dynamics. The analytical results (lines) predict quantitatively the locking range $\Delta\Omega$ (*Fig.3.10b,c*) for different operating J_{DC} , in both cases, even if the functions $A_1(p), B_1(p)$,

$B_2(p)$ are limited to the first order in amplitude p . Furthermore the model predicts the phase shift inside the locking range ψ (Fig.3.10c,d) and particularly the value of the additional phase shift ψ_0 , which differs from $\pi/2$ between the two situations.

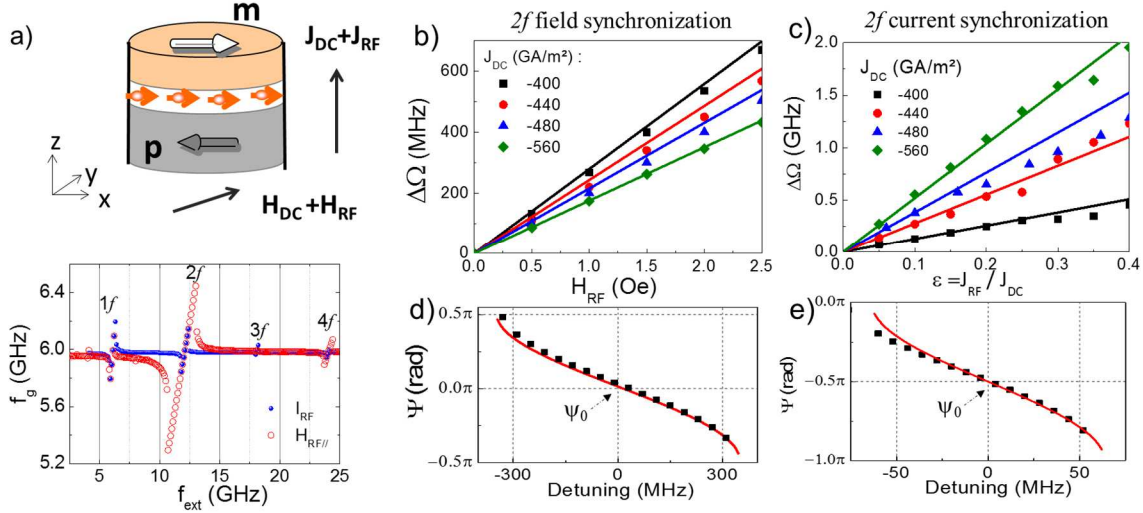


Fig. 3.10 a) Schematics of the in-plane STNO for synchronization and the generated frequency variation with the external source frequency. Locking range $\Delta\Omega$ at $2f$ versus the excitation amplitude H_{RF} for synchronization by field (b) and J_{RF}/J_{DC} for synchronization by current (c). The corresponding phase shift Ψ inside the detuning range (d,e). Lines are analytical results and dots numerical results. Parameters of the STNO: critical current $J_{cr} = -380 \text{ GA/m}^2$, $H_{DC} = 400 \text{ Oe}$, size of the free layer $90 \times 80 \times 3.9 \text{ nm}^3$, $\alpha = 0.02$, free running frequency $f_0 = 5.98 \text{ GHz}$ and amplitude $p_0 = 0.1$, non-linearity $v = -22$ [HemPhD].

The analytical method developed here treats a variety of synchronization cases for any spin torque uniform oscillators. It is a helpful tool to develop and optimized RF spintronic devices based on synchronization phenomena.

The planar STNO being very sensitive to the $2f$ synchronization by RF current, most of our investigations were focused on this case. As it is well known that the phase noise is the main source of linewidth broadening for non-isochronous oscillators, we investigate the phase noise behavior on the locked regime. The effect of thermal fluctuations on the transient behavior of the synchronized state of an STNO is analyzed in the frame of the generic model of a non-linear auto-oscillator with the complex variable $c = \sqrt{p}e^{-j\phi}$ (p - power and ϕ - phase) injecting a total current density of:

$$J_{app}(t) = J_{DC} + J_{RF} \cos(\omega_{ext}t) = J_{DC} [1 + \varepsilon \cos(\omega_{ext}t)].$$

In $2f$ synchronized state the phase difference between the phase of the generated signal and the external signal defined as $\psi = 2\phi - \omega_{ext}t$ is constant and the stationary power p_s is shifted by $\delta p = p_s - p_0$ from the free-running power p_0 . Keeping only the resonant terms at $2f$, it is possible to obtain the coupled equations:

$$\begin{cases} \frac{d\psi}{dt} = -\Delta\omega + 2N\delta p \\ \frac{d\delta p}{dt} \cong -2\Gamma_p\delta p + 2p_0F \cos(\psi) \end{cases}$$

with $\Delta\omega = \omega_{ext} - 2(\omega_0 + Np_0)$ and $\mathcal{F} = \varepsilon P_x \Gamma_J \frac{|\mathcal{B}|}{2\mathcal{A}} p_0$. The stable stationary solution

corresponding to the $2f$ synchronized state has the phase difference given by $\psi_s = \arccos\left(\frac{\Delta\omega}{\Delta\Omega}\right)$

with locking range $\Delta\Omega = \frac{2Np_0}{\Gamma_p} \mathcal{F}$ and the power shift $\delta p_s = \frac{\Delta\omega}{2N}$. Linearizing the above

equations around a stable solution allows us to study the transient behavior of the synchronized state, and analytically calculate the decaying rate of the amplitude and phase fluctuations in the synchronized state. In this case, the decay rate becomes:

$$\lambda_{1,2} = \Gamma_p \left[1 \pm \sqrt{1 - \frac{\varepsilon}{\varepsilon_c}} \right] \quad \text{with} \quad \varepsilon_c = \frac{\Gamma_p^2}{2Np_0^2 P_x \Gamma_J \frac{|\mathcal{B}|}{\mathcal{A}} \sin\psi_s}.$$

This decay rate is related to the power relaxation rate Γ_p of the free-running state, (or the frequency roll-off $f_p = \Gamma_p / \pi$). If $\varepsilon > \varepsilon_c$, $\lambda_{1,2}$ are complex conjugate and describe an oscillatory approach to the phase-locked state, which suggests the presence of sidebands on the locked regime due to the frequency of the transient oscillations. The side-bands are shifted from the carrier by: $\Omega = \Gamma_p \sqrt{\varepsilon / \varepsilon_c - 1}$. The phase approaches its locked state exponentially and oscillating above a certain critical microwave current.

Taking into account the thermal fluctuations as a Gaussian white noise, we can calculate the spectral density of the phase fluctuations on the synchronized state:

$$PSD_\phi = 2\pi\Delta f_o \frac{\left(\frac{\Gamma_p}{\pi}\right)^2 (1 + \nu^2) + f^2}{\left[-\left(\frac{\Gamma_p}{\pi}\right)^2 \frac{\varepsilon}{\varepsilon_c} + f^2\right]^2 + 4\Gamma_p^2 f^2}$$

where $\nu = Np_0 / \Gamma_p$ is the nonlinear coupling parameter and Δf_o is the linear linewidth. It is important to note that analyzing the phase noise properties in the Fourier space, inverse power law dependence on frequency $\sim 1/f^x$ is expected and information about underlying noise processes can be extracted. *Fig.3.11a* shows at very high frequency $f \gg f_p$ a $\sim 1/f^2$ dependence characteristic for a random walk behavior whatever the strength ε of the excitation. Instead at lower frequency $f \ll f_p$, the model predicts a crossover from $1/f^2$ to $1/f^0$ (white noise behaviour) even for a tiny microwave current such as $\varepsilon = 0.01$. Increasing further the RF current the noise level is expected to continuously decrease.

The transition from random walk to white noise has a direct impact on the shape of the peak of the signal which becomes very narrow and two symmetric sidebands appear upon increasing the RF current *Fig.3.11b*. The linewidth is progressively decreasing and the lowest value is reached once the phase noise flattens (*Fig.3.11c*). This is a proof that the linewidth is mainly controlled by the phase noise since the amplitude noise (*Fig. 3.11e*) has from the very beginning a white noise behaviour. A very good agreement it is found between the side-bands peaks predicted by the analytical model and all the numerical extracted information. However the analytical predictions are partially invalidated by the macrospin simulation since the full reduction of the linewidth below the resolution limit of the numerical calculation (20 kHz). occurs for much higher RF current (*Fig.3.11c*).

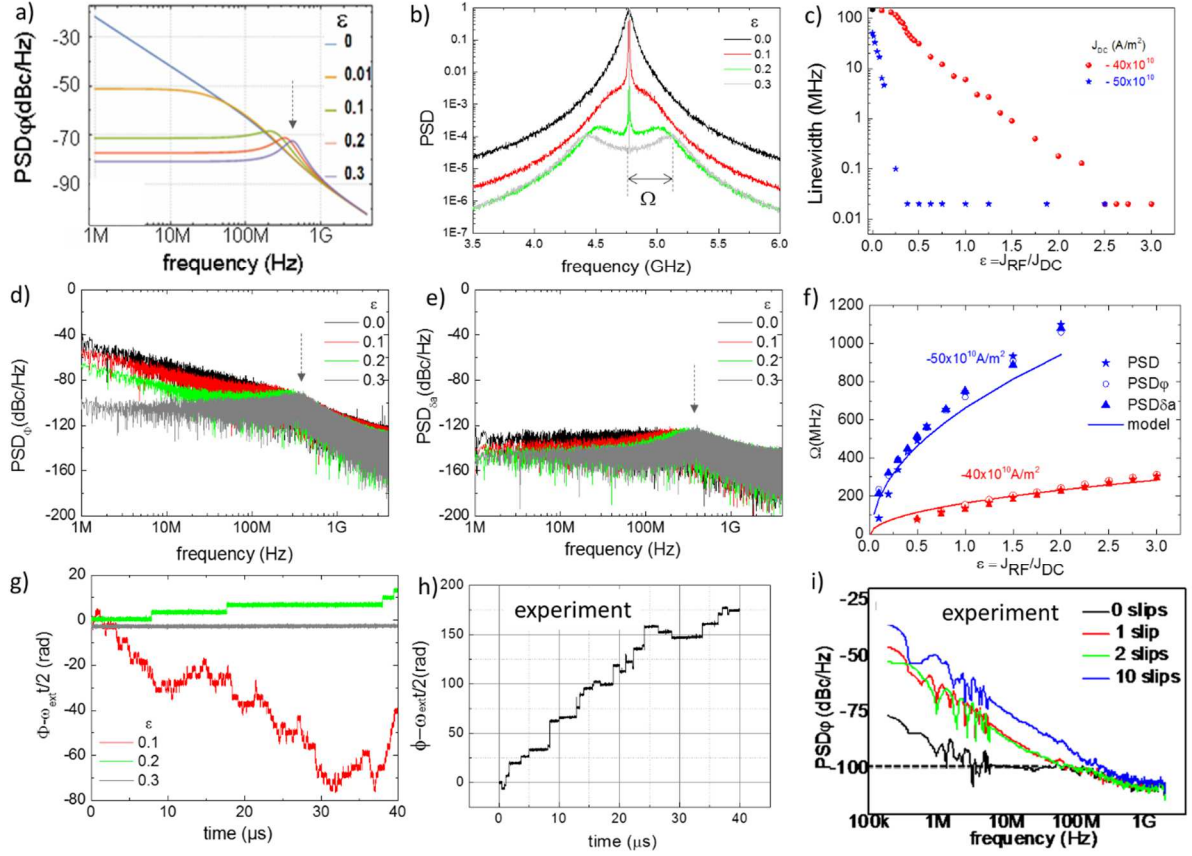


Fig. 3.11 a) Phase noise from analytical model. b) The PSD of m_y magnetization component as a function of ε . c) FWHM vs. ε for low current $J_{DC} = -40 \times 10^{10} \text{ A/m}^2$ (red dots) and medium current $J_{DC} = -50 \times 10^{10} \text{ A/m}^2$ (blue dots). d) Phase noise and e) amplitude noise from numerical simulation at 50K. f) Side-bands frequency for both low current regime (red set) and medium current regime (blue set). g) Simulated and h) experimental phase temporal traces. i) Phase noise analysis from the experimental time trace from $3 \mu\text{s}$ segments with 0, 1, 2, 10 phase slips.

The apparent disagreement between the analytical model and numerical results is related to existence of the *phase slips* intrinsic by the numerical simulation but not considered by the analytical model (i.e. the analytical description is addressing only the phase fluctuations around the stable phase). The temporal traces of the phase extracted from simulation (Fig.3.11g) shows a drift in time, together with the appearance of the phase slips, which becomes well defined upon increasing the RF current (Fig.3.11g). The number of phase slips per sampling period ($\sim 40 \mu\text{s}$) decreases at high RF current and above a threshold the phase slips are completely suppressed. These phase slips are responsible for the $1/f^2$ contribution of the phase noise at low offset frequencies and there are hiding the predicted $1/f^0$ contribution.

Jointly experimental studies were carried out on typical STO devices with in-plane magnetized MTJ having composition based on multilayers such as : IrMn /CoFeB /Ru /CoFeB /MgO /CoFe /CoFeB. Some important experimental results are summarized on Fig.3.12. In the autonomous regime, the oscillations have a free running frequency $f_0 = 7.5 \text{ GHz}$, with a linewidth of 55 MHz for an applied in plane field of 350 Oe and DC current $I_{DC} = -1.6 \text{ mA}$. The synchronization experiment was done varying the source frequency around two times the free running frequency of the oscillator, from 14 GHz to 16 GHz, and the source power was varied from -15 dBm to -5 dBm ($I_{RF} \sim 0.3$ to 1.3 mA), just before the sample starts to show signs of degradation. The PSD map of the output voltage of the generated frequency f_g as a function of the source frequency f_{ext} is shown in the Fig.3.11a for $\varepsilon = J_{RF} / J_{DC} = 0.7$. Fig.3.12b confirms that the frequency locking range $\Delta\Omega$ becomes wider by increasing the amplitude of the reference

current (ε) and that the linewidth decreases progressively until a minimal value. Notice that the linewidth reaches one order of magnitude reduction (8 MHz with a 1 MHz resolution). The temporal traces of the signal measured with a single shot oscilloscope are used to analyze simultaneously the amplitude and the phase noise. The amplitude noise shows an $1/f^0$ behavior both for synchronized (Fig.3.12c, black full line) and free running state (Fig.3.12c, gray dashed line), characteristic of white noise fluctuations of the amplitude around its average value. The phase noise in the synchronized (Fig.3.12c, red dashed line) and the free running state (red full line) show that the synchronization mechanism is efficient to reduce the phase noise by 20 dBm respect to the non-synchronized state. However both plots display a $1/f^2$ behavior characteristic from random walk behavior indicating that the pure phase locking state is not yet reached. Our experiments show that for the maximum applied microwave current, even though the oscillator is synchronized with the external source the emission linewidth remains broad. The phase noise decreases but it does not reach the $1/f^0$ behavior that would decrease the linewidth. Limited by the voltage breakdown of the samples we were not able to continue increasing the current and forcing a pure phase locking. The phase is subject of many slips (Fig. 3.11h) very similar with the macrospin simulation and the pure phase locking is possible only for short few μ s (Fig. 3.11i).

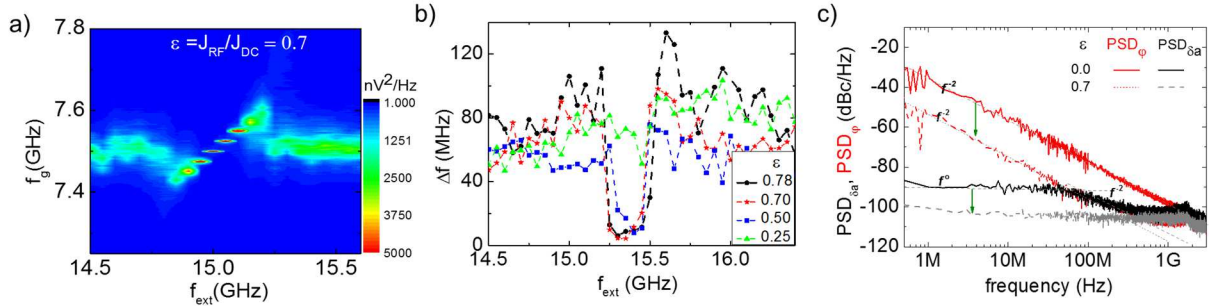


Fig. 3.12 a) Experimental PSD map of the output voltage at $I_{RF} = -1.12$ mA and $I_{DC} = -1.6$ mA. b) Linewidth vs $\varepsilon = J_{RF}/J_{DC}$. c) Amplitude and phase noise from the experiment for the non-synchronized state, (continuous line, $\varepsilon = 0$) and synchronized state (broken line, $\varepsilon = 0.7$). Notice that the synchronization mechanism is efficient to reduce the noise level (green arrows).

Analytically the synchronization at $2f$ by RF magnetic field is very similar with the synchronization by RF current. Experimental measurements must be done in the future for confrontation.

The theoretical and experimental studied confirm jointly that the synchronization of a STNO by RF current allows to drastically reduce the linewidth when phase slips are suppressed, but it is not possible to reduce it below the bounded noise level, which is almost independent from the RF current. Moreover, thermal fluctuations for in-plane magnetized STNO induce sidebands in the signal that should be taken into account for applications.

3.4 Modulation of STNO with planar polarizer

The STNO devices are of interest for microwave applications such as wireless communication but have also been proposed as a solution for read heads to rise up the bit data rate [Braganca2010, Watson2001]. In such a dynamic read head, STNOs read back the bit information using the concept of Frequency Shift Keying (FSK) [Watson2001]. The bit stray field, H_{bit} , modulates the frequency of STNOs between two discrete values around its carrier frequency. FSK concepts are also of interest for wireless communications in sensor networks. A first demonstration using Amplitude Shift Keying ASK [Watson2001] has been reported recently [Choi2014] by on-off switching the bias current, demonstrating 200-kbps data rate at a distance of $1m$ between the transmitter and receiver.

The modulation of the planar STNO might be implemented either by a current ($I_{\text{RF}}=I_m \cos\omega_{\text{mt}}$) either by a magnetic field $\mathbf{H}_{\text{RF}}=\mathbf{H}_m\cos(\omega_{\text{mt}})$. The modulation by current was straightforward after the synchronization by RF current previously presented since only the frequency of the RF current must be reduced, the topic was addressed by M. Quinsat during his PhD thesis, with the support of F. Garcia-Sanchez. The modulation under magnetic field was addressed by A. Purbawati both for periodic and pulse modulation supported by Ana Ruiz Calaforra. These studies together were focused on understanding the mechanism behind the modulation in the case of a non-isochronous auto-oscillator and establishing the useful features and limitations in perspective of applications.

3.4.1 Modulation under current

Modulation is occurring for the situation when the oscillator receives simultaneously a DC current I_{DC} (to generate the oscillation at frequency $\omega_g=2\pi f_g$) and an RF modulation current $I_{\text{RF}}=I_m \cos(\omega_{\text{mt}})$ (to modulate the response at $\omega_m=2\pi f_m$). This corresponds to a direct modulation of the generated microwave signal. The DC current sets the amplitude of the steady state excitation which is determined by the balance between the spin transfer torque and the damping torque. Hence an RF current modulates in first place the signal amplitude (signal power). This might be seen in *Fig. 3.13a* and *Fig. 3.13b* where the output voltage signal of a MTJ based oscillator is shown to oscillate in time in response to an RF current at the modulation frequency of $f_m=4\text{MHz}$.

The auto-oscillator general theory (*eq. 3.3*) indicates that small fluctuations due to noise of the signal amplitude are damped out over a time scale given by the power relaxation rate Γ_p . In the limit of small RF modulation amplitudes I_m , the above theory might be extended allowing to show that the instantaneous power deviation $\delta p(t)$ of the modulated signal with respect to the stationary power p_0 is proportional with the strength of the modulation $\varepsilon=I_m/I_{\text{DC}}$:

$$\delta p(t) = \varepsilon \frac{2\Gamma_-(p_o)p_o}{\sqrt{\omega_m^2 + 4\Gamma_p^2}} \cos(\omega_m t + \psi)$$

with $\psi = -\arctan\left(\frac{\omega_m}{2\Gamma_p}\right)$ and $\Gamma_-(p_o)$ is the prefactor of the spin transfer torque. The STNO is

non-isochronous and consequently its generated frequency $f_g(t)$ is adjusted simply by : $2\pi f_g(t) = \omega_0 + Np_0 + N\delta p_o$. If the coefficient of the nonlinear amplitude-phase coupling (N) is large a strong variation of the generation frequency $f_g(t)$ is expected. The equation for $\delta p(t)$ shows that the modulated amplitude rolls off at the relaxation frequency $f_p=\Gamma_p/\pi$. Therefore, this relaxation rate Γ_p determines the upper frequency at which the STNO amplitude (power) can respond to an RF current modulation. Thus, the amplitude and frequency modulation in a

STNO occur simultaneously, and frequency modulation in an STNO is a result of an amplitude modulation by the RF current.

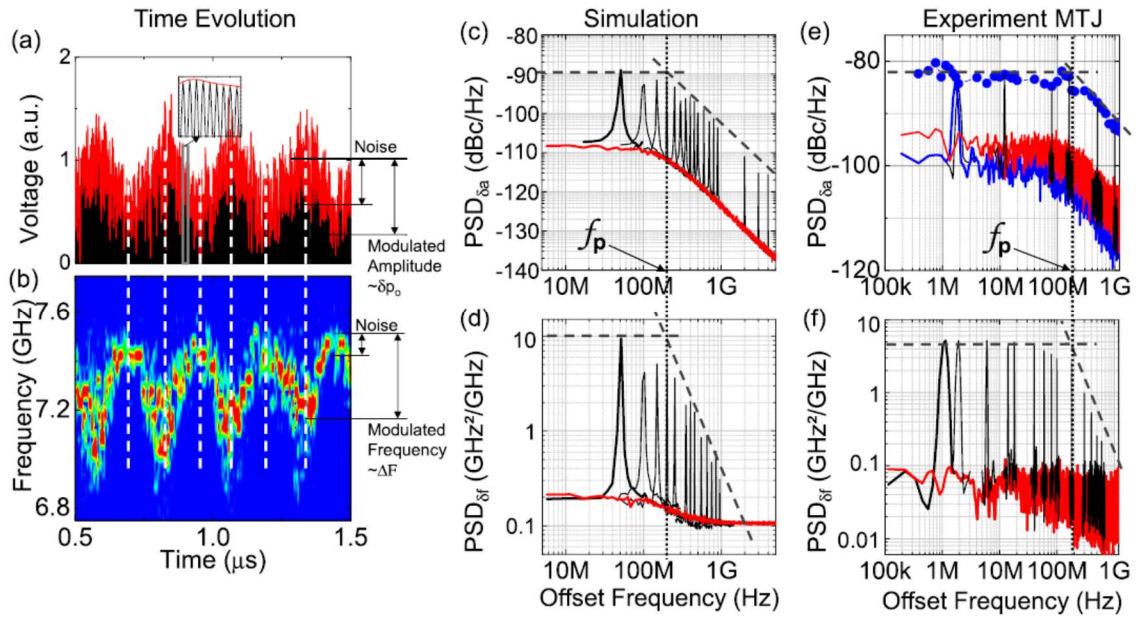


Fig. 3.13 (a) Time evolution of the STNO (a) output voltage and (b) frequency under RF current modulation. The injected RF modulation power is $P_{mod} = -20$ dBm and the modulation frequency is $f = 4$ MHz. For IPP modes the slope of frequency vs. current $df/dI < 0$ is negative (frequency redshift). (c) to (f): Amplitude noise $PSD_{\delta a}$ from (c) simulation and (e) experiments and frequency noise $PSD_{\delta f}$ from (d) simulation and (f) experiments. The blue dotted points in (e) correspond to the peak power of the modulation peaks obtained from different experiments upon varying the modulation frequency f_m . For sake of clarity, not all peaks are shown. As a guide to the eye, the envelope of these peaks is given in (c)–(f) by the dashed lines indicating the roll-off at f_p , estimated by the vertical dotted lines [Quinsat2014].

The theory predicts that the non-isochronous auto-oscillators have finite frequency bandwidth of both the amplitude and the frequency modulation and these bandwidths are determined by the damping rate. Experimental measurements and macrospin simulations were jointly used in order to verify this theoretical predicted feature in the case of STNO with in-plane polarizer and free layer. Practically, the investigation of the modulation might be done either by analyzing the sidebands appearing in the voltage power spectral density [Pufall2005, Muduli2010, Consolo2010] or via the amplitude and phase noise spectroscopy technique [Quinsat2010]. The latter technique has the advantage of providing separately the response of amplitude and frequency and to characterize their corresponding roll-off frequency being the most adapted with respect to the purpose of our study.

Typical amplitude noise $PSD_{\delta a}$ plots are shown in Figs. 3.13(c) and 3.13(e) (double logarithmic scale) for simulations and experiments, respectively, where the offset frequency corresponds to the frequency of the modulating or noise signal. In both simulations and experiments, two contributions to the signal can be seen. A low level background contribution that is due to noise (in red in Fig. 3.13c,e with -110 dBc/Hz for simulation and -95 dBc/Hz for the experiment at 10 MHz offset frequency) superposed by well-defined peaks that are ~ 20 dB above the background noise level and that are due to the modulation. The background contribution to the amplitude noise $PSD_{\delta a}$ due to amplitude fluctuations is white (independent on the frequency) up to a cut-off frequency $f_p = \Gamma_p / \pi$ and then falls off as $1/f^2$ (simulation $f_p = 185$ MHz, experiment $f_p = 200$ MHz). Upon varying the modulation frequency at a constant modulation power, the sharp peaks above the background shift accordingly. The envelope of these modulation peaks shows the same roll-off close to the f_p threshold, this is a prove that the

bandwidth of the amplitude modulation is given by the amplitude relaxation rate. In contrast to the amplitude, the oscillation phase of the free running oscillator is free. Hence phase fluctuations add up in time resulting in a random walk process that is characterised by an overall $1/f^2$ dependence for the phase noise PSD_ϕ . With $\text{PSD}_{\delta f} = f^2 \text{PSD}_\phi$ this is equivalent to a white frequency noise $\text{PSD}_{\delta f}$. Typical frequency noise $\text{PSD}_{\delta f}$ plots are shown in Fig. 3.13 d,f for simulation and experiment.

Using this technique for standard in-plane magnetized STNO devices, it was shown that in case of RF current modulation, this roll-off frequency is on the order of 100MHz and more importantly, that it is determined by the amplitude relaxation rate ($\Gamma_p = \pi f_p$). This will be a limit when Gbps data rates are targeted. This limit in current modulation is explained by the fact that I_{dc} sets the amplitude of steady state excitations oscillating at frequency $\omega_g = 2\pi f_g$. An additional RF current modulates the signal amplitude or signal power of the STNO. Frequency modulation occurs due to the nonlinear amplitude-phase coupling (non-isochronous property of STNOs). This explains why in this case frequency modulation is limited by the amplitude relaxation rate.

3.4.2 Modulation under magnetic field

Looking for a solution to avoid the roll-off frequency detrimental effect, we explored analytically and numerically the STNO modulation by a RF magnetic field. The modulation by an RF field is mainly involving the conservative part of the LLG equation while the modulation by current is related to the dissipative term. From this basic difference conservative/dissipative origin of the excitation one might expect to have perhaps modified mechanism of the frequency modulation. Indeed our studies confirm this initial intuition as presented hereafter.

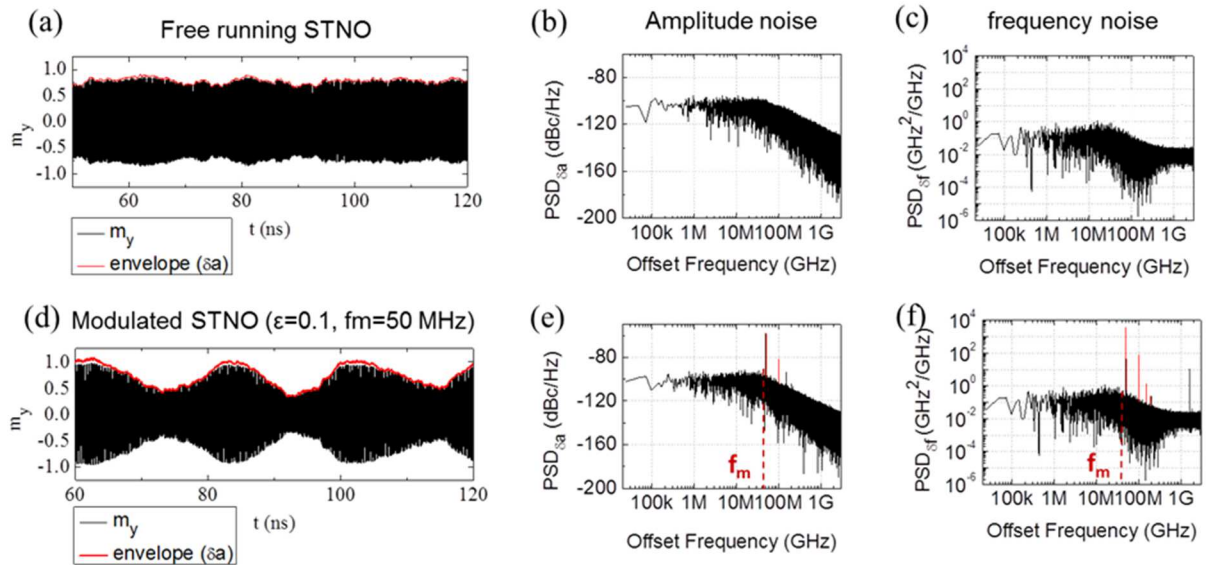


Fig. 3.14 a) The time traces of m_y -component of the free running STNO (black) and its corresponding amplitude fluctuations around its average value (red). b) The corresponding amplitude noise and c) the frequency noise. d) The time traces of m_y -component of modulated STNO with modulation strength, $\epsilon=0.1$ at slow modulation frequency, f_m . The amplitude is modulated at every 20 ns ($f_m=50$ MHz). The envelope of the amplitude modulation (in red) shows that the modulated amplitude fluctuates around its average value. e) The amplitude noise and f) the frequency noise of modulated STNO [PurbawatiPhD].

Series of simulations were performed on a similar sample as that analyzed previously in the synchronization by RF current study (Fig.3.10a). Typical temporal trace of transverse m_y magnetization including the thermal fluctuations corresponding to the free running state is

shown in Fig 3.14a. Both the amplitude noise Fig 3.14b and the frequency noise Fig 3.14c are presenting the roll-off around 200MHz in agreement with the corresponding analytical value of the $f_p=212\text{MHz}$. Superposing on the DC a modulating field $\mathbf{H}_{\text{RF}}=\mathbf{H}_m\cos(\omega_m t)$ (longitudinal configuration) the resulting amplitude is modulated at a frequency of 50MHz. Red peaks are appearing both in the amplitude noise and in the frequency noise spectra superposed on the black background of the free-running state Fig 3.14e,f.

At first glance, the observed behavior is very similar with modulation under current case. However, varying the \mathbf{H}_m field orientation, amplitude and frequency f_m (Fig.3.15) one might notice that for longitudinal pumping there is no roll-off frequency (Fig.3.15a-b). The modulation of the frequency is efficient up to 1GHz even that the relaxation rate of the STNO is around 200MHz and this features is conserved for various pumping strength ε (Fig.3.15e-f). This configuration of high symmetry is indeed very promising for the FSK application. Instead once the modulating field is transverse (perpendicular to the bias DC field) the frequency modulation is again limited by a roll-off frequency similar to the response observed in current modulation.

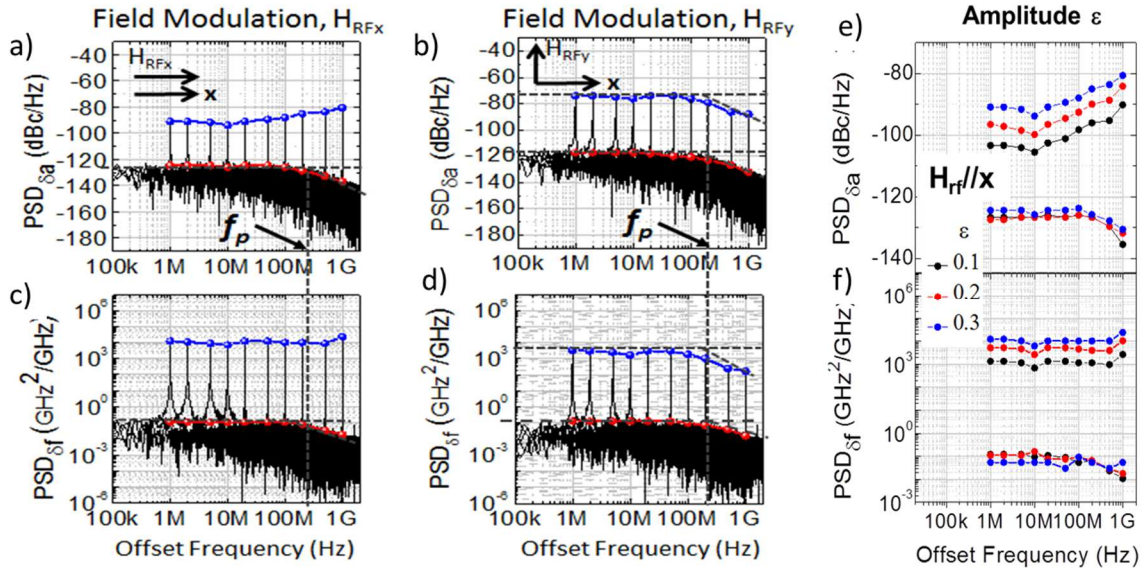


Fig. 3.15 Time traces of $42\mu\text{s}$ was analyzed in double logarithmic plots of the amplitude noise $\text{PSD}_{\delta a}$ and frequency noise $\text{PSD}_{\delta f}$ of the modulated signal for (a,b) longitudinal $H_{\text{RF}/x}$ and (c,d) transverse $H_{\text{RF}/y}$ RF fields. The current and field modulation simulation was performed with the same parameters of free running STNO ($H_{\text{app}}=40\text{mT}$ and $J_{\text{app}}=-50 \times 10^{10} \text{ A/m}^2$) at temperature of 50K and the same modulation strength $\varepsilon=0.3$. The envelope of the background level due to thermal noise is indicated by the red dotted line and the envelope due to the modulation signal by the blue dotted line. The envelope of modulation and noise PSD of (e) amplitude $\text{PSD}_{\delta a}$ and (f) frequency $\text{PSD}_{\delta f}$ for longitudinal RF field modulation as a function of modulation strength ε . [Purbawati PhD].

To better see the origin of these angular dependence behavior, the c -equation of the auto-oscillators was extended. In the longitudinal pumping case, analytically it is predicted that the instantaneous power deviation $\delta p(t)$ of the modulated signal with respect to the stationary power p_0 is proportional with the strength of the modulation field $\varepsilon=H_{\text{RF}x}/H_{\text{DC}}$:

$$\delta p(t) = \frac{-2\alpha \gamma_0' H_{\text{RF}x} p_0}{\sqrt{\omega_m^2 + (2\Gamma_p)^2}} \cos(\omega_m t - \psi) \quad \text{with the phase } \cot \psi = \frac{2\Gamma_p}{\omega_m}$$

Nevertheless, $\delta p(t)$ is also linear dependant with the damping parameter of the free layer α having usually very small value ~ 0.01 and the instantaneous power deviation is expected to be consequently small. More important, the instantaneous generated frequency is given by the

following relation: $2\pi f(t) = \omega_0 + N(p_0 + \delta p) + \frac{A}{\omega_0} \gamma_0' H_{RFx} \cos(\omega_m t)$. One might notice the presence of an additional term proportional directly with the modulating field H_{RFx} . Interestingly via this term the modulating field acts directly on the frequency and thus the absence of any roll-off mechanism is explained. As illustration, *Fig.3.16a* shows that the analytical model is in perfect agreement with the macrospin simulation for the longitudinal pumping. It confirms also that the non-linear amplitude-phase coupling plays negligible role in the frequency modulation in this case while for the current modulation the frequency modulation is mainly due to the non-linear amplitude-phase coupling (*Fig.3.16c*). In contrast, the transverse pumping case is more intricate since the frequency modulation looks similar with that of the case of the current modulation (*Fig.3.16b*).

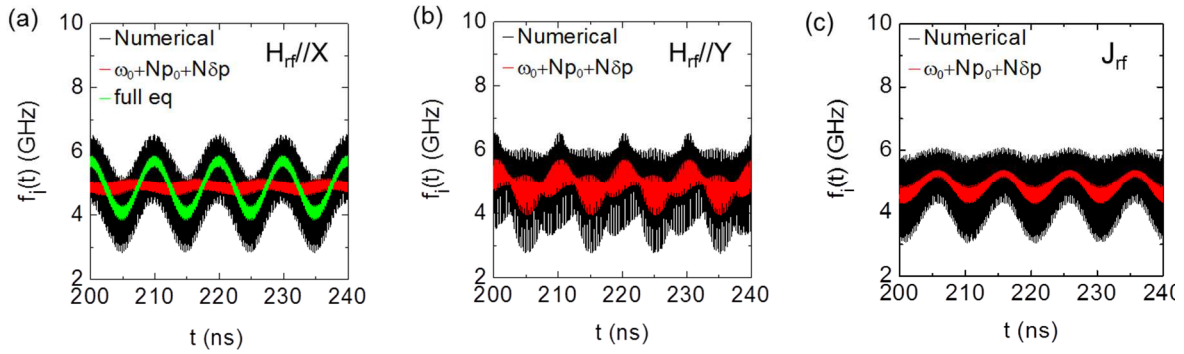


Fig. 3.16 Comparison between the numerical (black line) and analytical (red and green lines) instantaneous frequency $f_i(t)$ for a) longitudinal RF field ($H_{RF//X}$) modulation, b) longitudinal RF field ($H_{RF//Y}$) modulation, and c) current modulation at modulation frequency $f_m=100$ MHz and modulation strength $\varepsilon=0.3$. The red line considers only the contribution from amplitude modulation and the green line considers both amplitude and direct frequency modulation for longitudinal modulation case. The analytical evaluation was performed for $H_{app}=40$ mT and $J_{app}=-50 \times 10^{10}$ A/m² leading to the following analytical parameters $\omega_0=40.5$ Grad/s, $N=-31.6$ Grad/s and $A \varepsilon \gamma_0' H_{app}/\omega_0=5.217$ Grad/s.

We demonstrate via numerical simulation that the modulation of STNOs under RF field is an alternative way with no upper limit to the modulation frequency. In the case of in-plane magnetized materials, modulation at frequencies higher than $f_p=\Gamma_p/\pi$ can be achieved when using a modulating RF field that is oriented along the equilibrium direction given by an external dc bias field (longitudinal RF field, H_{RFx}). In contrast, tilting the modulating RF field in-plane perpendicularly with respect to the bias field (transverse RF field, H_{RFy}), the modulation is again limited by a roll-off frequency similar to the response observed in current modulation. The absence of the roll-off in longitudinal RF field modulation is explained within an extended analytical model from which the deviation of the instantaneous power and the instantaneous frequency of the modulated output signal are extracted and analyzed in comparison to numerical simulation.

3.5 Coupling phenomena in STNO

3.5.1 Influence of interlayer coupling on the spin-torque-driven excitations

A standard STNO configuration contains an in-plane magnetized synthetic antiferromagnet (SyF) as a polarizer and an in-plane magnetized free layer (FL) (see Fig. 3.17a). Most experimental observations on the excitations of such STNOs have been analyzed theoretically or numerically in the frame of a single layer model, where the free layer is considered independent with respect to the SyF whose magnetization is kept fixed. However, several features observed experimentally cannot be explained within the frame of a single layer model. This difference arises from the fact that in a real STNO nanopillar there are multiple interactions between the layers that influence the emission properties. The topic of the interlayer coupling was addressed mainly by the PhD thesis of E. Monteblanco, with the support of several post-doctoral colleagues (B. Lacoste, A. Jenkins, M. Romero, F. Garcia-Sanchez, D. Gusakova) and intern students (G. Geranton, A. Marronnier).

Fig. 3.17b shows the corresponding experimental field-current state diagram measured in a spin valve device: static and dynamic states are excited varying the field and the current, complicated boundaries between various regions are observed. Moreover, the frequency-field dispersion of the steady state mode presents gaps and kinks, very different features with respect to the Kittel-like behavior predicted by the single-FL model (section 3.2). The comparison between the field-current state diagram computed in the single-FL model with that computed once various couplings are considered (mutual spin transfer torque, dipolar coupling, RKKY inside de SAF polarizer) is a first indication of the importance of the couplings. The boundaries of the diagrams are very sensitive especially to the dipolar coupling between and the gaps observed can be attributed to the dipolar interaction.

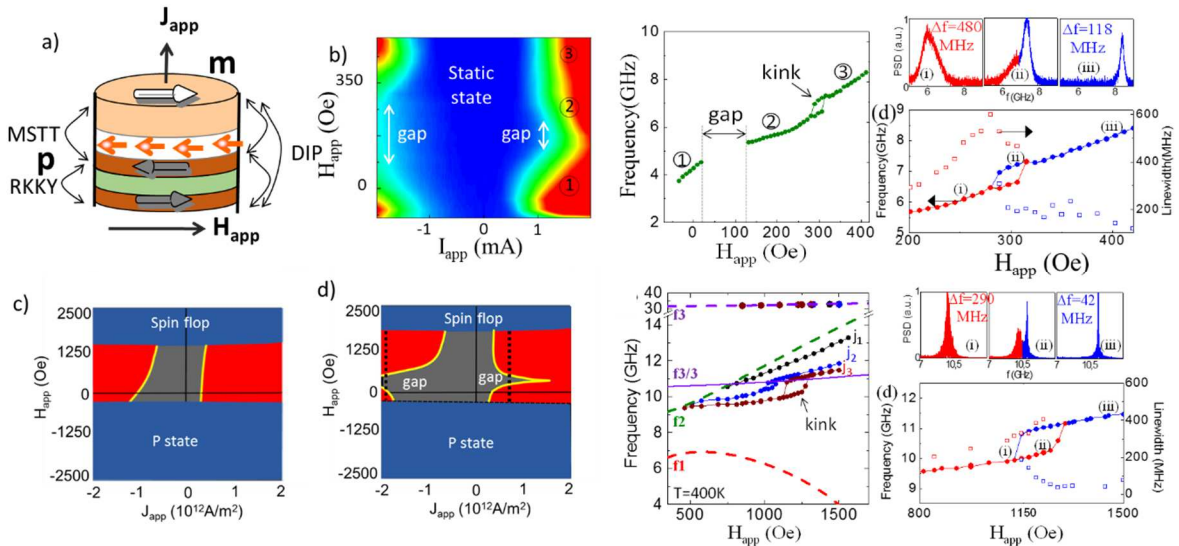


Fig. 3.17 a) Schematic of the standard STNO device considered in experiment and simulations and indication of the interactions between the different layers, with MTT mutual spin torque, DIP dipolar interaction, and RKKY the interlayer exchange interaction. b) Experimental field-current state diagram deduced from the power spectral density map. The blue region corresponds to the static AP state and the colored region corresponds to self-sustained steady states. Experimental frequency-field dispersion at $J_{app}=0.32 \times 10^{12} \text{A/m}^2$. Experimental power spectral density (PSD) spectra of the steady state mode at different values of applied field, corresponding to points (i), (ii), and (iii) indicated on the zoom of the experimental frequency (full dots) and linewidth (open squares) as a function of field. c) Simulated state diagram in the limit of uncoupled layers. d) Simulated state diagram for 3 coupled layers. Simulated frequency-field dispersion, PSD spectra for various operation points. [Romera2015]

Analyzing experimentally the generated frequency of the STNO in the proximity of the *kinks* one might notice a discontinuous evolution of the frequency with a splitting into two branches (upper and lower frequency) that coexist over a certain range of fields (see point (ii) in *Fig.3.17b*). Furthermore, the PSD peak is much narrower for the mode in the higher frequency branch and consequently the linewidth of the upper frequency branch is lower than that of the lower frequency branch (open squares).

According to the linear approximation, in a 3 coupled layers system 3 eigenmodes and their harmonics can be excited as shown by the dashed lines—labeled by their respective frequencies f_1 , f_2 , and f_3 on the simulated frequency-field dispersion (*Fig.3.17d*). It is noted that the magnetization of all three layers are involved in the oscillations of modes 1, 2, and 3. The stability analysis of these linear modes defines the conditions for which one of the modes is driven into steady state in the presence of a spin polarized current. Here, the analysis focuses on the range of larger positive fields (but lower than the SyF spin flop field) and positive current where mode 2 is driven into steady state when the current is larger than the critical value. This mode corresponds to an in-plane precession (IPP) mode that is dominated by the FL. The macrospin simulations confirm the existence of a kink, the mode splits into two branches that coexist over a certain range of fields. By switching on and off the different interactions in the simulations, it was checked that the dipolar coupling between the layers is the main responsible coupling mechanism for the observed kink and not the mutual spin torque interaction which only plays a minor role changing slightly the field and current values for which the kinks are observed. Further analysis of the simulated PSD spectra shows that the mode splitting occurs in the region where the third harmonic of the steady state mode 2 is close to the frequency of mode 3 that is overdamped for the given sign of current. As in the experiment, the mode splitting also affects the linewidth of the simulated peaks. The reduced linewidth can be explained by a reduction of the non-linear contribution to the linewidth via an enhanced effective damping.

To conclude, macrospin simulations and experiments on spin valve nanopillars show distinct features in the spin torque driven excitations that cannot be explained without taking the interactions between the magnetic layers into account, in particular, the dipolar coupling. This coupling has the effect that when the FL dominated mode is driven into steady state, a discrete jump in frequency occurs for certain ranges of current and field values. It was shown that this is a non-linear effect, where the spin torque driven (FL-dominated) mode can pump a damped mode (in this case here the SyF dominated mode) via its 3rd harmonics through dynamic dipolar interaction. These results will be of importance for applications, indicating that microwave performances of STNOs can be optimized by designing STNO stacks of appropriate dipolar and RKKY interaction to take advantage of the coupling mechanisms.

3.5.2 Non-linear auto-oscillator model for coupled layers

The influence of the coupling between the layers on the STNO emission properties is an important issue for the development and the optimization of STT microwave devices. Macrospin simulations can account various couplings mechanism and reveal the associated signature on the STNO operation. However, the identification of the role played by each coupling and how each one can be better exploited is not obvious. We are familiar with the non-linear auto-oscillator model (*c*-equation model) to explain the basic features of single layer excitations. Developing an equivalent compact and simple analytical model but for coupled layers was our objective.

We have focused on the spin torque driven dynamics of a self-polarized system based on two layers coupled via interlayer exchange (conservative coupling RKKY) and mutual spin torque (dissipative coupling, MSTT). As reported on *Fig.3.18a-d* the macrospin simulations

indicate very different frequency-current dispersion law. If the single layer model predicts clearly a redshift behavior $df/dj < 0$, instead for the coupled layers a transition from the redshift $df/dj < 0$ to blueshift $df/dj > 0$ is expected. This latter feature has been observed experimentally in a similar RKKY coupled system using an external polarizer, being a typical feature of the dynamics of a two-layer coupled system that is driven by STT into steady state.

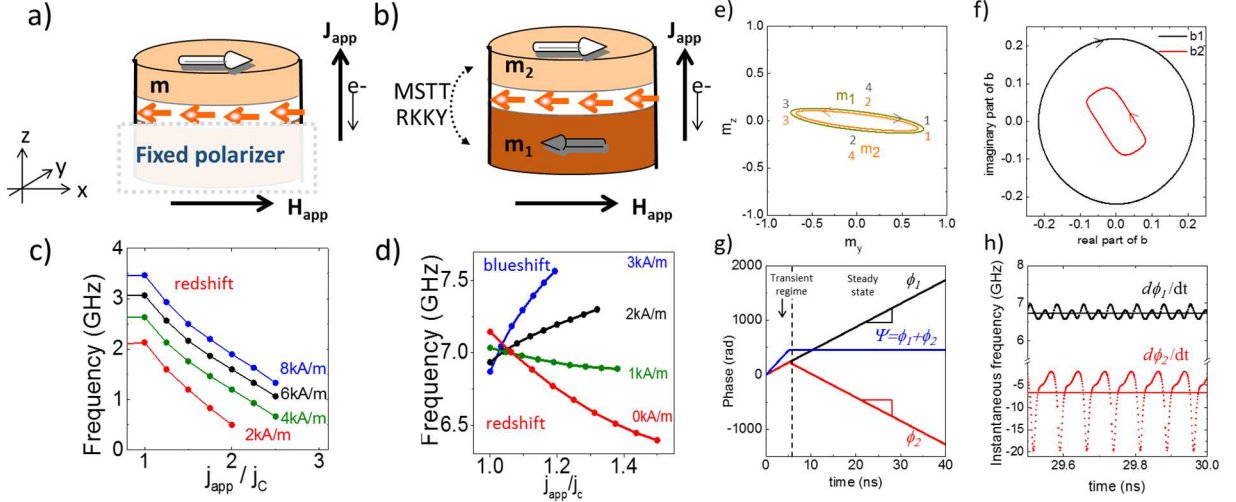


Fig. 3.18 Schematics of (a) the single layer picture and (b) the self-polarized SyF system. Frequency versus supercriticality j_{app}/j_c (j_{app} is applied current density and j_c is critical current density) at $T = 0K$ at different values of field for (c) the single layer case and (d) for the self-polarized SyF obtained by solving numerically the LLGS equation. Analysis of the steady state dynamics in (e) the $m_{x,y,z}$ components and (f) in the b basis, obtained by numerical simulations for zero applied field and $j_{app} = 450 \times 10^{10} A/m^2$. (f) Imaginary vs real part of b_1 and b_2 . Time evolution of the phases (g) and instantaneous frequencies (h). Horizontal lines in (h) correspond to the average frequency values. [Romera2016]

The non-linear auto-oscillator theory is based on a change of coordinates to complex variables to represent the magnetization dynamics of the layers. The phase and amplitude of the complex variables describe the non-linear dynamics of the auto-oscillator. The validity of this approach is limited to quasi-conservative trajectories, for which the energy is almost constant, and to small oscillation amplitudes. Using common diagonalization techniques, the conservative part of the magnetization equation of motion is simplified to two terms: a linear and a non-linear contribution. The dissipative part, which is supposed to be small compared to the conservative part, defines the equilibrium energy of the auto-oscillator by balancing the negative Gilbert damping and the positive STT. These general concepts of spin wave theory are adapted to pass from vectorial variables \mathbf{m}_1 and \mathbf{m}_2 to complex conjugate b_1, b_1^*, b_2, b_2^* . The mathematical formalism of this transformation was developed by B. Lacoste and the general perturbed hamiltonian equation of the self-polarized SyF system reads as:

$$\begin{aligned} \dot{b}_1 &= -[j(\Omega_1 + \Psi_1 + \Sigma_1) + \Gamma_1 + \Pi_1]b_1 \\ \dot{b}_2 &= -[j(\Omega_2 + \Psi_2 + \Sigma_2) + \Gamma_2 + \Pi_2]b_2 \end{aligned} \quad (3.4)$$

Here Ω_i, Ψ_i $i = 1, 2$ are functions derived from the conservative terms of the LLG equations and depend only on the sample parameters and applied field. The dissipative terms of the LLG equations generate $\Sigma_i, \Gamma_i, \Pi_i$ $i = 1, 2$ which are functions depending on the sample parameters, applied field but also the injected current value and the damping constants.

The full transformation of the IPP trajectories describes by \mathbf{m}_1 and \mathbf{m}_2 from 3D real space in the complex space is shown in Fig.3.18e-f. In 3D space both layers are excited at almost equal amplitude, but precess such that their relative phases are close to an optic-like mode. The optic-like character of the excited mode is straightforward in b representation since

the amplitude $|b_1|$ is much larger than the amplitude $|b_2|$. The rotation sense of b_2 is opposite to the one of b_1 , the sum of the phases is locked and layers oscillate with the same average frequency even that the b_2 variable (acoustic-like) is subject of very large variations of the instantaneous frequency.

The significant part of the model development consists on selecting the terms in *eq. 3.4* which integrated over one oscillation period are nonzero (resonant terms) with a significant impact on the steady state dynamics of the coupled system. The balance between conservative and dissipative terms is subtle. From the analysis of the different terms and their comparison to the numerical simulations, it is possible to truncate the general perturbed hamiltonian arriving to a simplified equation as follows:

$$\begin{pmatrix} \dot{b}_1 \\ \dot{b}_2 \\ \dot{b}_1^* \\ \dot{b}_2^* \end{pmatrix} = - \begin{pmatrix} i(\Omega_1 + \tilde{\Psi}_1) + \tilde{\Gamma}_1 & \tilde{\Theta}_1 & \tilde{\Xi}_1 & \tilde{\Delta}_1 + i\vartheta_1 \\ \tilde{\Theta}_2 & i(\Omega_2 + \tilde{\Psi}_2) + \tilde{\Gamma}_2 & \tilde{\Delta}_2 + i\vartheta_2 & \tilde{\Xi}_2 \\ \tilde{\Xi}_1 & \tilde{\Delta}_1 - i\vartheta_1 & -i(\Omega_1 + \tilde{\Psi}_1^*) + \tilde{\Gamma}_1 & \tilde{\Theta}_1 \\ \tilde{\Delta}_2 - i\vartheta_2 & \tilde{\Xi}_2 & \tilde{\Theta}_2 & -i(\Omega_2 + \tilde{\Psi}_2^*) + \tilde{\Gamma}_2 \end{pmatrix} \begin{pmatrix} b_1 \\ b_2 \\ b_1^* \\ b_2^* \end{pmatrix} \quad (3.5)$$

The full definition of the terms is given in the reference [Romera2016]. Note that all off-diagonal terms have a dissipative origin. The *antidiagonal* terms ($\tilde{\Delta}_i \pm i\vartheta_i$) are those with strongest impact in the dynamics. As a main remark, in contrast to the single layer model, the phase equation of the coupled system has a contribution coming from the dissipative part of the LLGS equation. In order to describe the STT steady state excitations, both linear eigenmodes contribute and the characteristic relation between the phases of the eigenmodes is such that the sum of the phases remains constant, and not the phase difference as it is the case in most phase locked systems.

It is found that the blueshift regime numerically predicted comes from the competition between conservative and dissipative terms, where the nontrivial dependence of these terms on the amplitudes and phases plays a crucial role. It is found that the blueshift regime can only occur when the power ratio p_1/p_2 has a weak dependence with current. This happens only in a region of field where the two linear eigenmodes contribute equally to the steady state mode (i.e., high mode hybridization).

This analytical model opens perspectives to better control and understand nonlinear phenomena and it will be important to further predict the nonlinear parameters as a function of coupling strength, and to exploit the coupling mechanisms to optimize the microwave performances for applications.

The above report on the STNO activity from view point of the modelling is indicative of the large diversity of challenges to overcome, problems to solve and questions to address. The STNO topic is not complete, strong by our past experience new challenges will be pursue as listed later in the chapter with the prospective activities.

Chapter IV: Magnetic random access memories

The concept of random access memories having magnetic nanopillars as memory points covers a large panel of configurations. Firstly the MRAMs are divided with respect to the writing scheme based on field driven, current-driven or heat assisted magnetization switching. Taking as criterion the orientation of the magnetization of the storage layer the MRAM are planar, perpendicular or even mixed between (precessional). If the writing path is used or not also as reading path one might have 2-terminal or 3-terminal devices respectively. My activity is related to current-driven writing MRAM both STT and SOT for cells with in-plane and out-of-plane magnetization. By modelling we focused on the way how the magnetization of the storage layer is reversed, targeting fast and reliable switching, with low power consumption and high retention.

The memory function supposes: to read/write the information and keep it for long time. The reading as for the STNO is straightforward based on tunnel magnetoresistance, the main issue is to have two stable states easily distinguishable (high signal to noise ratio). The writing of the information means to successfully commute the magnetization between the two stable states using nanosecond range pulses of spin-polarized current (spin torque transfer STT or spin orbit torque SOT). The robustness of the information storage is controlled by the intrinsic parameter of the storage layer but it must be guaranteed against the thermal fluctuation or any perturbation occurring during the reading. The schematics of the configurations addressed by modelling are summarized in Fig.4.1.

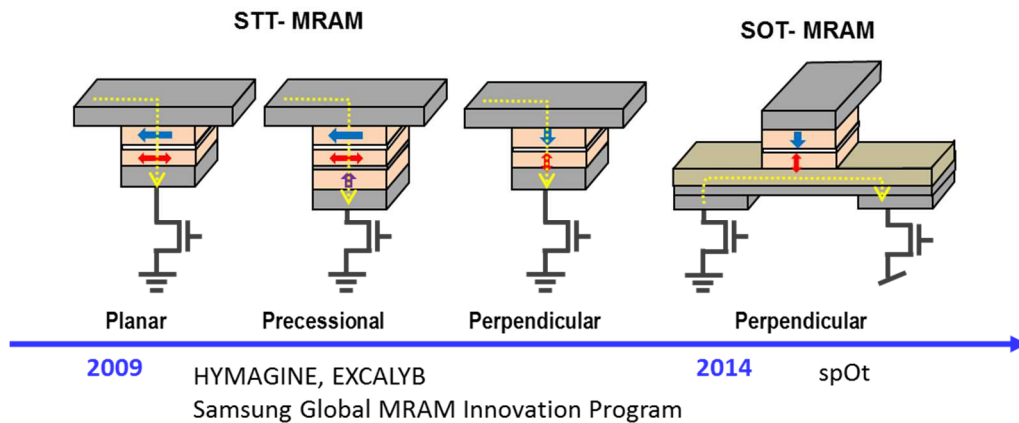


Fig. 4.1 Schematics of typical MRAM cells based on spin transfer torque and spin orbit torque. Red arrows are the magnetization of the storage layer while the blue arrows are the magnetization the fixed reference layer. The writing current path is indicated in yellow.

Typical 3D trajectories described by the magnetization of the storage layer during the reversal are illustrated on Fig. 4.2 if the free storage layer has the easy axis laying in the plane or out-of-plane. According to a macrospin approach the magnetization is moving on the unitary sphere following large angle dynamics. Hereafter several types of MRAM writing scheme are briefly summarized from the view point of the modelling. Conclusions will be listed either for the operation of the memory cell but also concerning the use and validity of various modelling tools.

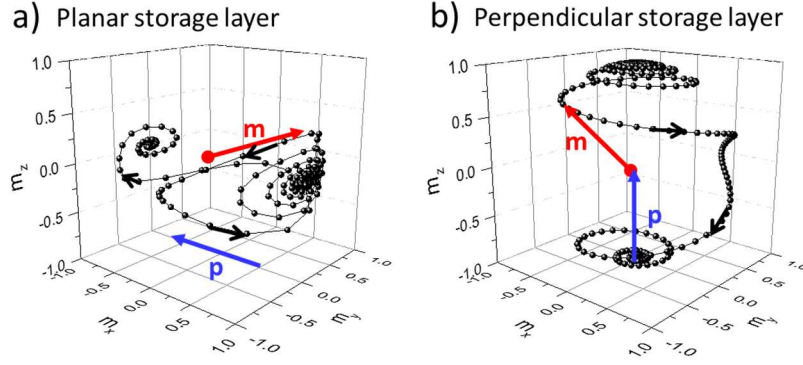


Fig. 4.2 Trajectory of the magnetization during the reversal by STT for a) planar and b) perpendicular case.

4.1 Planar spin transfer torque MRAMs

The modelling predictions are affected by the hypotheses on which the model is built. The comparison with the experimental observation should be carefully addressed. Especially if the size of the nanopillar is relatively large with respect to the characteristic length of the storage layer material parameters (exchange length, domain wall width) the use of a macrospin approach is limited. The trajectories obtained by micromagnetic modelling are large angle precessions similar to the macrospin ones but magnetization dynamics is quite different. As an illustration, the case of the writing process in an MRAM with both in-plane magnetized storage and reference layers. The core of the cell is placed in the middle of a nanopillar with an elliptical cross-section $130\text{nm} \times 65\text{nm}$ and total height of 125 nm. This is a very simple case: a uniform DC spin-polarized current is injected in the structure and only the magnetization of the free layer can evolve in time since the magnetization of the polarizer is fixed (i.e. parallel to the long axis of the elliptical sample). In zero applied field for an elliptical cross-section dot, because of the shape anisotropy, only two stable states are possible: single-domain with the magnetization pointing left or right. The magnetization can be switched from one direction to the other if a high enough spin-polarized current is injected. The switching from parallel state (PP, free layer magnetization parallel with the polarizer) to the antiparallel state (AP, free layer magnetization antiparallel with the polarizer) is obtained for an injected current of 5 mA ($\sim 7.5 \times 10^7 \text{ A/cm}^2$). The time traces of the mean magnetization component parallel with the long axis of the free layer are depicted in Fig.4.3a for three different models. *i*) The black curve was obtained with a macrospin model. After a precessional motion of increasing amplitude, the switching occurs in 3.1 ns (i.e., the time for which longitudinal magnetization crosses the time axis $\langle m_x \rangle = 0$). *ii*) The red curve was computed by three-dimensional micromagnetic simulation. The result very similar to the macrospin prediction, but the estimated switching time is shorter, ~ 2.7 ns. *iii*) If the Oersted field generated by the injected current itself is considered, the switching takes longer, ~ 3.4 ns, and the time trace is quite complicated. The reason for this difference is intimately related to the magnetization dynamics, as revealed by the snapshots shown in Fig. 4.3b-c.

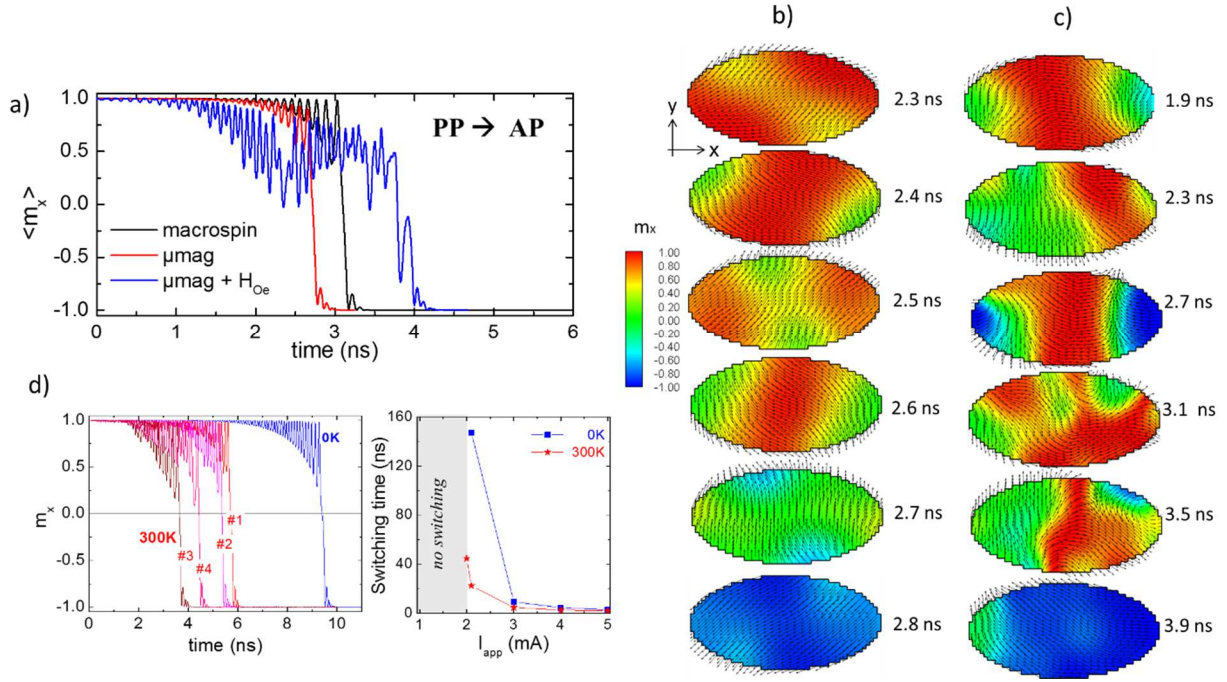


Fig. 4.3 a) Time evolution of the longitudinal magnetization once the current is switched on (i.e., STT is active) as given by a three-dimensional micromagnetic model, with and without the Oersted field generated by the current itself. Magnetization snapshots during the reversal process considering only the STT term b) and including also the Oersted field generated by the current itself (c). The color scale is associated with the longitudinal magnetization component and the arrows indicate the in-plane magnetization direction. d) Time traces of the longitudinal magnetization obtained by a macrospin model at 0 K and 300 K (4 events). Average value of the switching time as a function of the injected current. The statistics was achieved using 4000 events.

Even in the case considering only the spin transfer torque action, the magnetization pattern is very non-uniform. This is counter-intuitive, considering that the time traces of the magnetization are rather similar to that for the macrospin case. Furthermore, when combining the influence of spin-transfer torque and Oersted field, the nonuniformity of magnetization distribution is enhanced. The central symmetry induced by the Oersted field fights against the uniaxial shape anisotropy. As a result, during the reversal process, a lot of spinwaves are generated and their extinction takes more time (i.e., small damping value) with a direct impact on the switching time.

The above results are for a temperature of 0 K (no thermal fluctuations). Insight about the impact of thermal fluctuations on the switching time is provided by carrying out simulations at 300 K as shown in Fig. 4.3d. Large number of simulations is requested for accurate statistical analysis thus the macrospin is the most suitable model for such kind of investigations. As expected upon increasing the injected current the magnetization reversal is faster for both temperatures. The impact of the thermal fluctuations is obvious near the critical current value. This prediction is in agreement with experimental observations: the reversal depends strongly on thermal fluctuations. In such collinear configuration the symmetry must be broken to initiate the reversal, the fluctuations must create an initial angle between the storage layers magnetization \mathbf{m} and the spin current polarization \mathbf{p} so that the STT becomes nonzero, which triggers the magnetization reversal. Therefore, if nothing is done to avoid it, there is a random incubation time preceding the magnetization switching (see various events Fig. 4.3d), which can last several nanoseconds. This phenomenon must be carefully addressed in designing fast memories. Hopefully, the magnetization naturally bends at the edge of the pillar, which helps to nucleate the magnetization reversal, thus allowing to reduce the stochasticity.

4.2 Precessional switching for MRAMs

One way to counter-act the switching stochasticity consists in using a planar-perpendicular configuration such that previously studied for the STNO, known as Orthogonal Spin Transfer-MRAM (OST-MRAM). The system under consideration is composed of an in-plane magnetized MTJ with an additional perpendicular polarizer separated from the storage layer by a non-magnetic spacer (a metal such as Cu or an insulator such as MgO). This concept was studied at Spintec during the PhD thesis of M. Marins de Castro, B. Lacoste with the help C. Papisoi. By modelling A. Vaysset addressed the role of the dipolar coupling between the layers on the robustness of fast magnetization reversal. Two configurations were compared having as polarizer a single layer or a synthetic antiferromagnetic (SAF) (Fig. 4.4). It is known that a single layer perpendicularly magnetized dot generates a magnetic stray field in the surroundings. Since the storage layer is placed nearby the polarizer (~few nm away), it is subject of this strong highly non-uniform dipolar coupling. Inserting an additional SAF in the structure of a MTJ nanopillar is not a trivial issue from fabrication point of view and requested optimization. Thus knowing that the SAF structure is really mandatory or not for the memory cell operation was our main task. Firstly, we identified the switching conditions (current value and pulse duration) and secondly we investigated how these conditions are affected or not by the dipolar coupling.

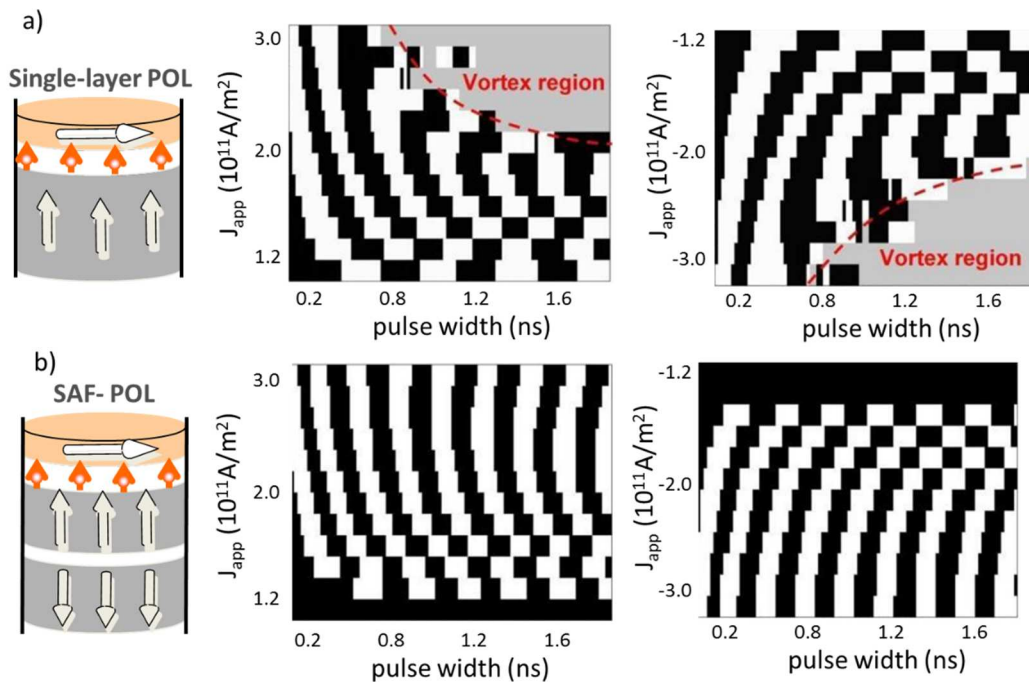


Fig. 4.4 Current – pulse duration switching diagrams for a) a single-layer polarizer and b) SAF polarizer case. Color scale: white is for switching, black is for non-switching, and grey for a vortex in final state [VayssetPhD]. Size of the nanopillar 100 nm x 90nm.

In this purpose, the current density and the pulse length are swept and switching diagrams are plotted for the two current polarities for both devices. Black stripes alternate with white stripes meaning no-switching versus switching regions. As expected, for short pulses one needs higher injected current to trigger the magnetization reversal. One might note that the switching of the magnetization can be achieved with quite short pulses well below ns (~250 ps). At a given current value, above the threshold current to drive the OPP steady state (see section 3.1) the pulse duration must be adjusted with respect to the period of the oscillation in

such a way to stop the magnetization OPP precession around the opposite state with respect to the initial state orientation. These conditions are easily fulfilled for the SAF polarizer case, the switching stripes are very regular with a periodicity equivalent to the OPP. In contrast, adding the stray field of the polarizer, the diagrams are changing for large current and/or long pulses. The origin of the difference might be found in the magnetization dynamics as depicted in *Fig. 4.5*. The presence of the dipolar field with a strong out-of-plane component facilitates the nucleation of out-of-plane magnetization regions in the storage layer and thus the creation of a vortex-like structure which destroys the coherent OPP dynamics. At the end of the pulse, if the vortex is sufficiently far from the border it remains stable and spirals around the center of the free layer at a much slower frequency with a trajectory of gradually decreasing radius. Consequently once the current is turned off at the end of the writing cycle, the probability of the switching process is around 50%.

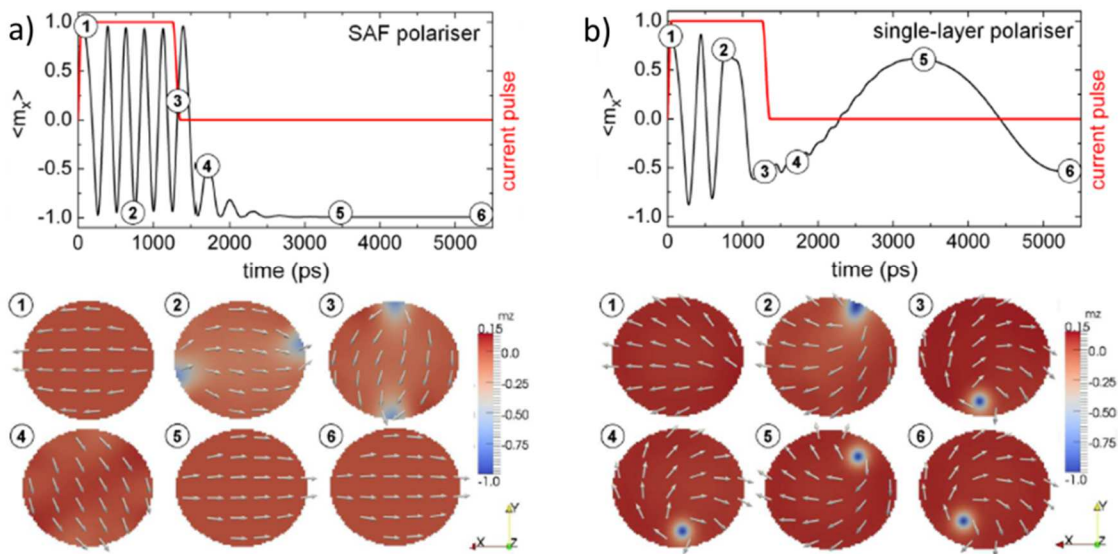


Fig. 4.5 a) Simulations for a current density $J_{app} = 2.5 \times 10^{11} \text{ A/m}^2$ and pulse length $\Delta t = 1210 \text{ ps}$ with (a) a SAF perpendicular polarizer and (b) a single-layer perpendicular polarizer. The color scale represents the out-of-plane component of the magnetization. In (b), when the current is off, the vortex describes a spiral around the free layer center. The system is at static equilibrium when the vortex reaches the center. [VayssetPhD]

In conclusion, the coherence of the magnetization dynamics is affected by the stray field created by the polarizer, and leads to a rapid damping of the oscillations of switching probability as a function of pulse duration. Therefore, the use of SAF polarizer improves the switching reproducibility in these very fast switching MRAM cells.

The experimental studies confirm partially the numerical predictions (*Fig. 4.6*). For the single-layer polarizer one single peak is only clearly detected for the transition P→AP so the writing procedure based on precessional mechanism is even less efficient than predicted by the simulation. Instead, for the case SAF-polarizer the probability of switching between P and AP states (forward and backward) is varying periodically with the pulse duration as expected. One might distinguish up to 4 peaks but unfortunately their amplitude goes progressively to 50%. The control on the writing scheme is lost for long pulses because of thermal effect, longer the pulse higher the heating of the structure. This feature was not predicted by the simulation since the Joule effect was not accounted by the micromagnetic model.

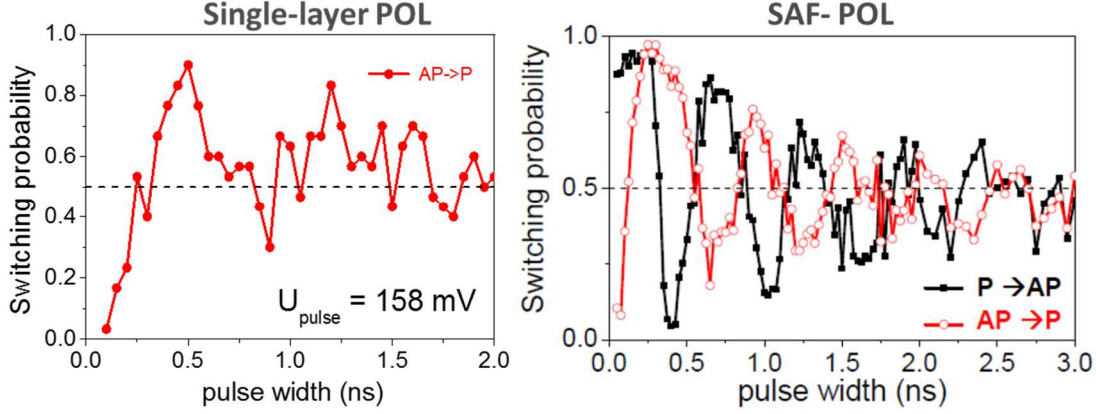


Fig. 4.6 a) Switching probability versus pulse length. $P_{switch} = 1$ means switching was observed in 100% of the measurements. $P_{switch} = 0$ means final state was always identical to initial state [Papusoi2009].

4.3 Perpendicular spin transfer torque MRAMs

The previous studies addressed cells with lateral sizes on the order of 100nm, this range is not allowing very compact memories. Scaling down the size is mandatory to be competitive with the equivalent dense semiconductor memories. So far the pSTT-MRAM standing for perpendicular STT-MRAM represents the most promising technology. Both the storage and the reference layer are perpendicularly magnetized, besides the polarizer itself is a very robust SAF structure to avoid unfavorable dipolar coupling (schematics Fig.4.4). Moreover the associated materials in the stack of the nanopillar allow for very high perpendicular anisotropy for the storage layer and even for small volume (small lateral size < 50 nm) the thermal stability ratio Δ is maintained in the limit requested by the industry ($40k_B T$). The anisotropy is originating from interfacial phenomena occurring between the ferromagnet (CoFeB) and the insulator (MgO) being high enough to balance the demagnetizing effect. Thus the magnetization at the interface is forced to point perpendicularly to the plane and through exchange interaction the total magnetization of the layer is orientated out-of-plane. Upon increasing the thickness of the layer the interfacial effect is diluted and the benefit of out-of-plane anisotropy is lost, the magnetization is laying in the plane as imposed by the shape anisotropy (demagnetizing effects).

At Spintec the topic of pSTT-MRAM was addressed intensively by A. Timopheev and N. Strelkov under the coordination of B. Dieny, R. Sousa and M. Chshiev in the frame of *Samsung Global MRAM Innovation Program*. The core of the associated studies is represented by the stability field-voltage diagrams allowing to extract information about the mechanisms and the properties of STT induced magnetization switching. These diagrams by their shape are intimately related with the intrinsic parameters of the sample such as the transport parameters, the anisotropy or the damping. The analysis is based on the LLG equation having the two terms coming from the spin transport namely the *damping-like* and *field-like* typical for MTJ characterized by a prefactor $a_{//}$ and a_{\perp} respectively:

$$\frac{\partial \mathbf{m}}{\partial t} = -\gamma_0 (\mathbf{m} \times \mathbf{H}_{\text{eff}}) + \alpha \left(\mathbf{m} \times \frac{\partial \mathbf{m}}{\partial t} \right) - \gamma a_{//} V \mathbf{m} \times (\mathbf{m} \times \mathbf{p}) + \gamma a_{\perp} V^2 (\mathbf{m} \times \mathbf{p}).$$

For the collinear geometry (i.e. applied field parallel with the easy-axis of the storage and polarizer layers), the LLG equation allows one extract some critical line using the technique of stability analysis. It is similar with the analysis carried on for the STNO for determining the threshold current to drive the oscillations and the results are summarized on the Fig. 4.7a. The

vertical lines are corresponding to the switching field $H_{C\pm} = \pm[H_K - (N_{ZZ} - N_{YY})M_s]$ controlled by the magnetocrystalline H_K and shape $(N_{ZZ} - N_{YY})M_s$ anisotropy. The two other lines have quadratic dependence on the voltage such as:

$$H_{app} = \pm[H_u - (N_{ZZ} - N_{YY})M_s] - \left(\frac{1}{\alpha} \frac{a_{//}}{\mu_0} V_{C\pm} - \frac{a_{\perp}}{\mu_0} V_{C\pm}^2 \right) P_z$$

with P_z the pointing direction of the polarizer. Note that the V^2 dependence starts to be important in front of the *damping-like* contribution only for very strong *field-like* STT. The experimental diagram measured on a nominal 50nm diameter pillar (Fig.4.7b) is quite similar even that the recording procedure is based on 40ns voltage pulses. The analytical lines are valid for static applied field and DC voltage and it is not possible to have them if finite writing pulses. However the $V_{C\pm}$ lines should be shifted towards large voltage amplitude upon reducing the pulse duration.

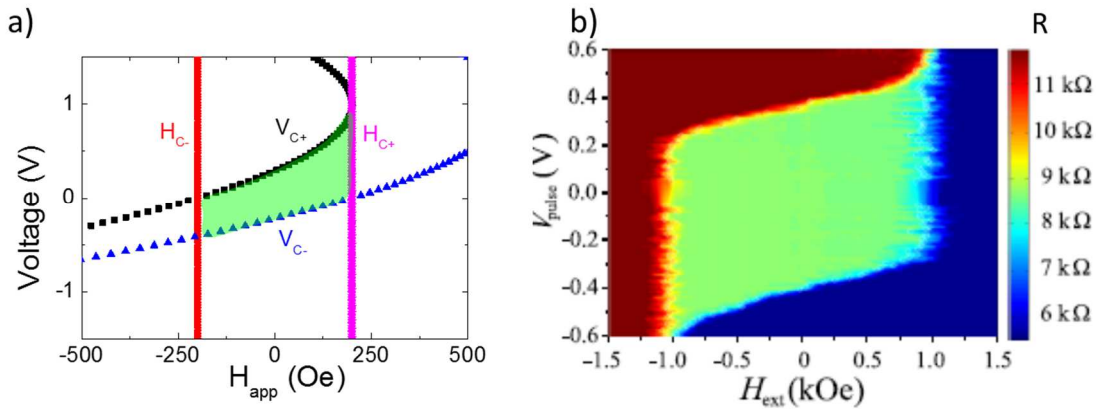


Fig. 4.7 a) Analytical critical lines from stability analysis under DC voltage and DC field with $a_{//}=0.8\text{mT/V}$ and $a_{\perp}=10\text{mT/V}^2$. b) Experimental stability VH diagram measured with writing pulse of 100 ns [Timopheev2015].

The analytical model does not account either for the heating (thermal fluctuations), the numerical macrospin modelling is thus again necessary. We tried to evaluate the impact of transport pre-factors ($a_{//}$ and a_{\perp}) on the stability diagram as shown on Fig.4.8. Pulses of voltage of 40ns and variable amplitude are applied on the storage layer under a static magnetic field parallel with the easy-axis (out-of-plane). Thus three types of regions are identified: blue for parallel stable state (P), red for anti-parallel stable state (AP) and green for bi-stable region (both P and AP states are stable). The shape of these regions is evolving with the relative strength of the pre-factors. When the effective contributions from both pre-factors are comparable, the phase diagram acquires a noticeable asymmetry, as can be seen for the last two diagrams in the middle column. However, such a combination of pre-factors $a_{//}$ and a_{\perp} already can be physically unrealistic in terms of values. The experimental phase diagram shape is similar to those obtained from the theoretical analysis and the simulations where the *field-like* STT term is not dominating.

Finite temperature macrospin simulations in LLG formalism under finite writing pulse duration have confirmed the negligible role of the *field-like* term in the current-driven switching process of pMTJ structure. Limitations of the macrospin model are not expected to be important in the case of pMTJ pillars with diameters comparable to or below the exchange length. This is confirmed by the experiments carried out on 40-nm-diameter pMTJ pillars.

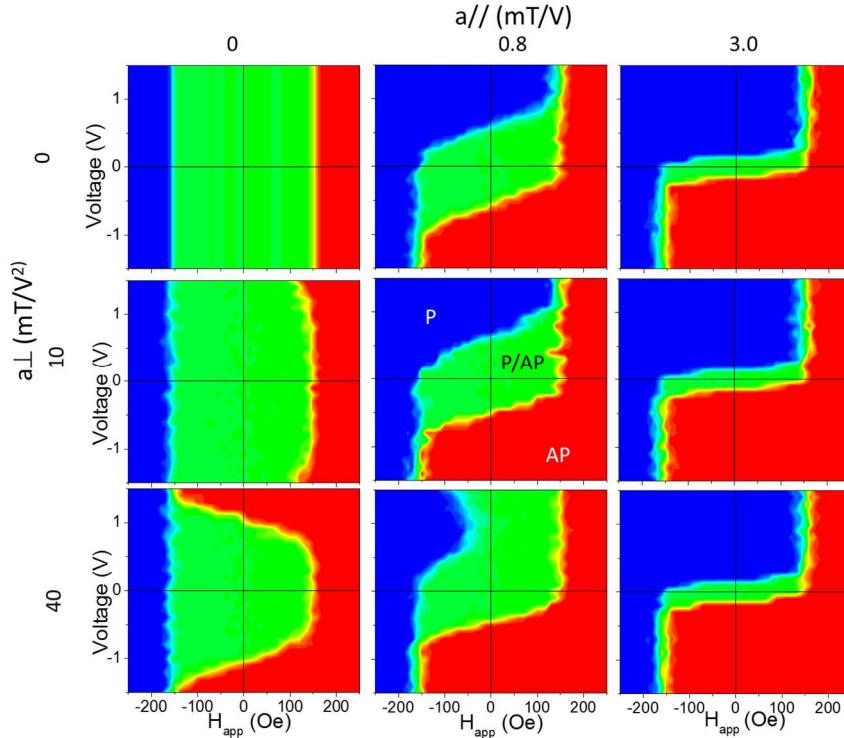


Fig. 4.8 a) Finite writing pulse phase diagrams for different in-plane and out-of-plane STT prefactor magnitudes: at $T = 300$ K. The model parameters are $H_{sat} = 200$ Oe, and $\alpha = 0.01$. Integration time was $1 \mu\text{s}$ in each field point, and the writing pulse width is 40 ns. Each diagram is an average of 10 identical simulations [Timopheev2015].

Considering the rising interest for noncollinear geometries, it is also interesting to study these phase diagrams in such geometry, i.e. in situations where the field is applied at some angle with respect to the normal to the layers, introducing thus a non-collinearity in the static configuration of the storage and polarizer layers. Non-collinear configuration of magnetic electrodes influences the switching characteristics of the storage layer and its field dependence defines the phase boundaries of the stability diagram. The experimental measurements performed on MgO based MTJ with finite writing pulse are reported on Fig. 4.9 confirming the strong dependence of the VH diagrams on the direction of the applied field while the bistable P/AP region preserves its symmetry around the origin.

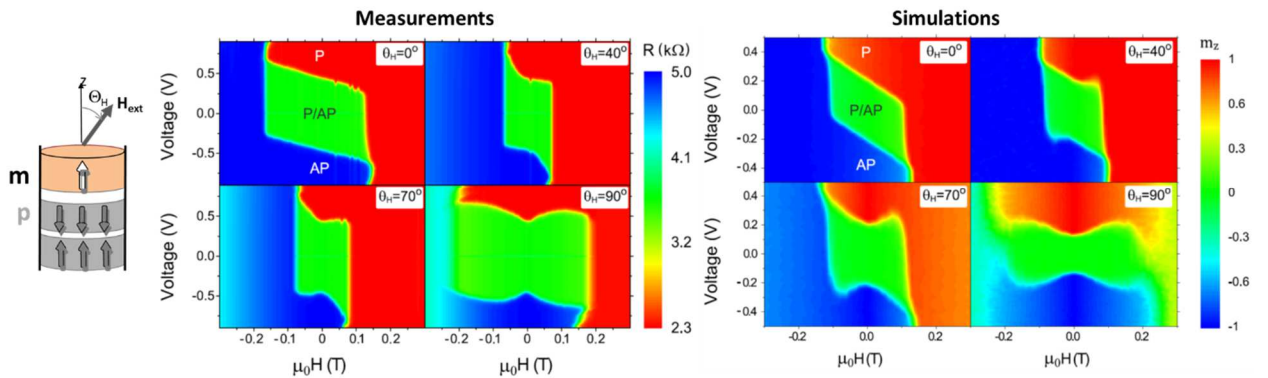


Fig. 4.9 Experimental and simulated stability VH diagrams of 80 nm diameter MTJ at room temperature for $\Theta_H = 0^\circ, 40^\circ, 70^\circ$ and 90° . Voltage pulse length was 100 ns. The color scale is related to the resistance of MTJ or the out-of-plane magnetization component [Strelkov2017].

All our attempts to recover by macrospin or micromagnetic modelling the experimental observations fail for a standard model accounting for a strong out-of-plane uniaxial anisotropy $E_{anis} = K_1(1 - m_z^2)$. Nevertheless, a good agreement between experiments and simulations is recovered when a second order anisotropy contribution is introduced in the model such as: $E_{anis} = K_1(1 - m_z^2) + K_2(1 - m_z^4)$. The signature of this higher order anisotropy term is not always visible in the collinear geometry but clearly shows up once the field is applied away from the normal to plane of the sample. Such second order anisotropy contribution is similar to that reported previously in literature and it seems to originate mostly from the interface imperfection.

Due to this second order term, when the condition $K_{2,cr} < -\frac{1}{2} \left[K_1 - \frac{1}{2} \mu_0 (N_{ZZ} - N_{YY}) M_s^2 \right]$ is fulfilled, the magnetization of the magnetic layer is no longer parallel with the normal to the layers at zero field, but prefers to lay on an easy-cone surface (*Fig. 4.10a*). An important parameter for the application is the estimation of the critical current with no applied field. Upon reinforcing K_2 , the switching voltage distributions progressively move towards smaller values and their width becomes narrower as depicted in *Fig. 4.10b*. In the inset of the same figure the switching voltage variation with the pulse duration is shown. As one can see, there are two regimes: above 30 ns the voltage is almost constant while a sharp increase is observed for very short pulses below 5 ns. Usually the pulse duration for STT memory application is in the range of 10 ns. Taking as a reference this pulse duration, the switching voltage dependence on K_2 for two different temperatures 300 K and 30 K is represented in *Fig. 4.10c*. In the easy-axis regime the thermal fluctuations are mandatory for the initiation of the magnetization switching thus the two curves are clearly separated. In contrast, in the easy-cone regime, the switching voltage is independent of temperature. In addition, due to the intrinsic tilt of the magnetization, the two curves are superposed. The easy-cone state is thus favorable for memory applications since the writing stochasticity is considerably reduced.

However, the K_2 affects not only the switching voltage distribution but also the energy barrier as given by the following relation:

$$\frac{E_B}{Volume} = \begin{cases} \frac{K^2}{4|K_2|} & K + 2K_2 < 0 \\ K + K_2 & K + 2K_2 > 0 \end{cases}$$

The energy barrier over $k_B T$, shown in *Fig. 4.10d* by the grey line, is continuously decreasing upon reinforcing K_2 . At the onset of the easy cone regime $K + 2K_2 = 0$ the stability factor

$\Delta = \frac{E_B}{k_B T}$ has decreased already by 50% with respect to the situation $K_2 = 0$. This might be seen

as a detrimental condition for memory application. Nevertheless, the energy consumption of the memory (right axis *Fig. 4.10d*) is also continuously decreasing approaching tens of fJ for 5 ns pulses.

As a result, second order anisotropy term appears to be quite beneficial for fast STT-MRAM even in the still easy-axis regime provided the thermal stability of the storage layer magnetization can be maintained sufficiently large to cope with the memory retention specification. For memory applications the second order anisotropy appears to be an interesting parameter to control and adjust, since it allows to write with lower energy and less stochastically while preserving a reasonable thermal stability.

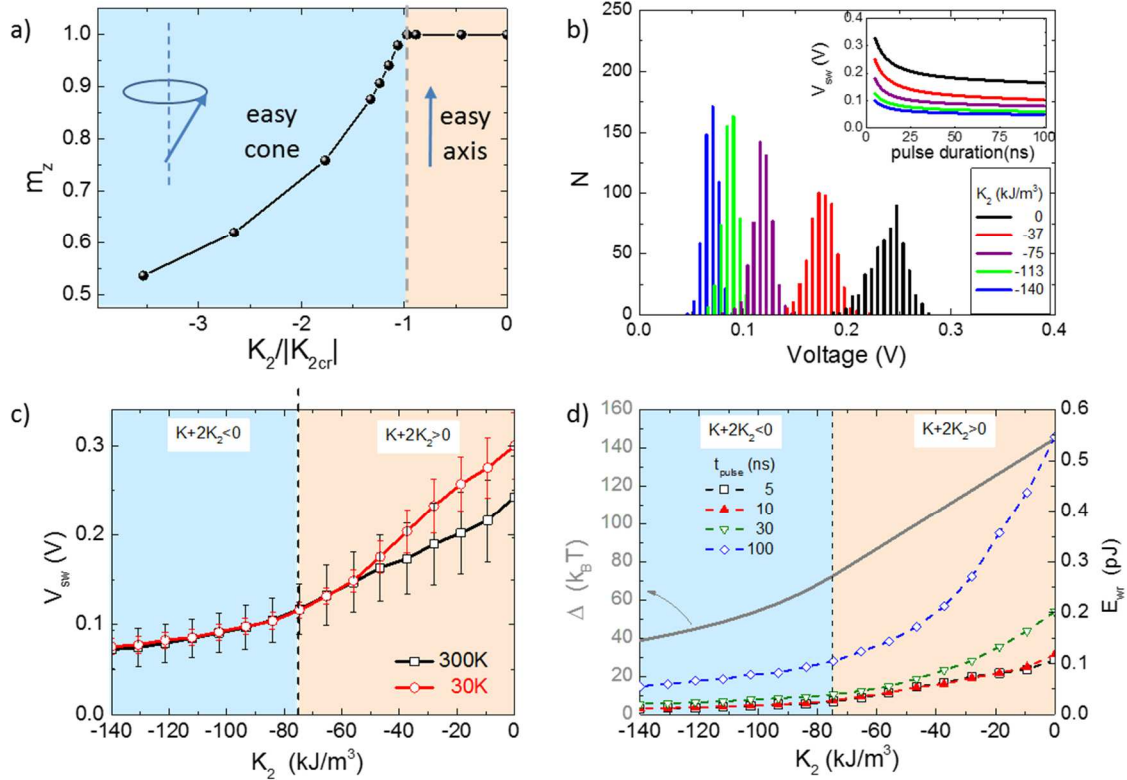


Fig. 4.10 a) Out-of-plane magnetization at equilibrium depending on the K_2 constant. b) The number of switching operations after 500 loops at $T=300$ K for a pulse length of 10 ns and different values of K_2 . Inset: dependence of switching voltage versus writing pulse duration for the same K_2 values. c) Switching voltage versus K_2 for 300 K and 30 K for a pulse duration of 10 ns, the vertical bars are the width of the voltage distribution. d) Dependence of Δ (in $k_B T$ units, 300 K) and writing energy on the constant K_2 for several pulse durations. [Strelkov2017].

4.4 Spin-orbit torque MRAMs

In the race always smaller and faster, the present pMRAMs start to be affected by problem of viability since the stress on the tunnel barrier might damage it irreversibly. As presented above shorter the writing pulse duration higher the amplitude of the switching voltage, meaning thus a large current value passing through the nanopillar which potentially destroys the barrier or reduces considerably its efficiency. This drawback is intrinsic to the geometry of a 2-terminal device: the writing and the reading current paths are the same.

One interesting solution for this practical problem is to separate the writing and the reading as a 3-terminal device does: the writing current is not anymore flowing through the barrier but in a heavy metal underneath line. This concepts called hereafter SOT-MRAM was initiated at Spintec by G. Gaudin, O. Boulle and M. Miron as a spin-orbitronic device. The modelling of such a memory cell was part of the EU grant spOt and partially done by N. Mikuszeit with the experimental observations provide by P. Gambardella's team from ETH Zurich (K. Garello). This study is an extension for the topic of chiral phenomena and magnetic

domain walls presented in chapter 2. The sample is simply cobalt nanodot patterned in a film sandwiched between platinum and an insulating oxide such as AlO_x .

The objectives of the modelling were to provide information about the impact of the antisymmetric exchange (e.g. interfacial DMI) on the magnetization reversal in ultrathin Co Pt/Co/AlO nanodot (Fig. 4.11). From practical point of view we tried to establish the suitable conditions for reliable (deterministic), bipolar and fast switching.

Firstly we studied the mechanism of magnetization reversal at 0K. Initially, the magnetization of the dot is pointing down ($-\text{Oz}$). After a longitudinal ($\parallel\text{Ox}$) static magnetic field is applied ($\mu_0 H_x \sim 100\text{mT}$), much smaller than the longitudinal saturation field value in such a way that the magnetization is still pointing downward but a small magnetization longitudinal component is developed. This equilibrium state is finally excited by the injection of current J_{app} entirely passing through the Pt line generating simultaneously Rashba (*field-like* term) and spin Hall (*damping-like*) torques in the LLG equation (eq.1.34).

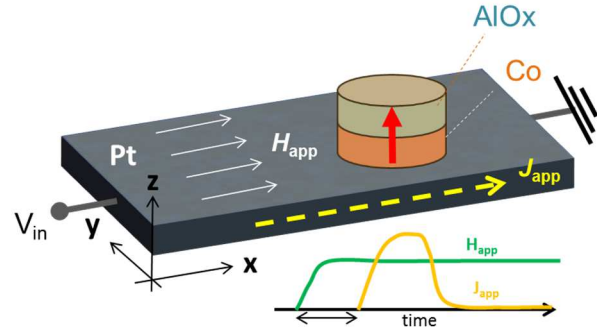


Fig. 4.11 Schematic of Co dot on top of Pt stripe. Definition of coordinates.

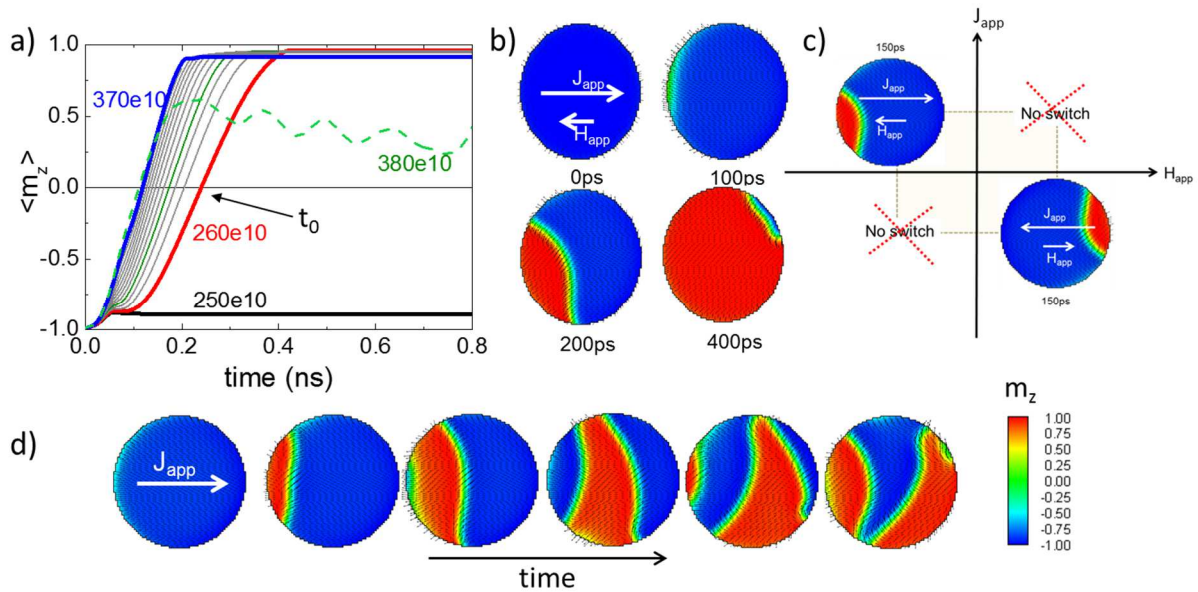


Fig. 4.12 a) Time evolution of the average out-of-plane magnetization for different applied current densities (variations in steps of 10^{11} A/m^2). The minimum current to trigger switching, i.e. the critical current, is highlighted in red. The green curve indicates the threshold of turbulent behavior. b) Snap-shots of the magnetization configuration showing the reversal from down (blue) to up (red) via domain wall nucleation and propagation under an externally applied field of $\mu_0 H_{app} = -0.1 \text{ T}$ and a current density of $2.6 \times 10^{12} \text{ A/m}^2$. c) Illustration of the bipolar character of the switching and the symmetry of the magnetization reversal. d) Snap-shots of the magnetization configuration showing the evolution driven by a current of $3.5 \times 10^{12} \text{ A/m}^2$ without applying any in-plane field. Note the nucleation of reversed domains occurring periodically at the left edge.

Typical simulation results for a 100 nm dot with a DMI constant $D=2\text{mJ/m}^2$ are presented in Fig. 4.12a. Depending on the current amplitude, three regimes are identified:

i) For $J_{app} \leq 2.50 \times 10^{12} \text{A/m}^2$ no magnetization switching is observed. The spin orbit torque leads to a slight tilting of the magnetization toward the plane of the dot, but the magnetization relaxes back to its initial equilibrium state after the current is turned-off.

ii) At intermediate current values ($2.60 \times 10^{12} \text{A/m}^2 \leq J_{app} \leq 3.70 \times 10^{12} \text{A/m}^2$) the magnetization reversal occurs. The time evolution of the magnetization pattern in the dot (Fig.4.12b) reveals that, the magnetization reversal occurs by domain wall nucleation shortly after the pulse injection (100 ps), followed by fast DW propagation. For this polarity of current and applied field the nucleation of the DW always occurs on the left edge of the dot. Once nucleated, the DW propagates fast through the dot and is expelled on the opposed edge. The switching time t_0 , defined by $\langle m_z \rangle(t_0) = 0$, decreases as J_{app} increases; the increase of the slope of $\langle m_z \rangle(t)$ indicates that this is related to a faster DW propagation. As expected the DW has a Néel configuration due to the large chiral DMI (see section 2.3). The simulation highlights that the DW nucleation occurs for all current values on the same edge in a deterministic way. Symmetrically, when reversing the sign of the current, the reversal from the up to the down state occurs on the opposite edge, i.e. the behavior is bipolar (Fig.4.12c).

iii) For higher currents ($J_{app} > 3.70 \times 10^{12} \text{A/m}^2$) the motion of the DW becomes turbulent (oscillatory) and the coherence of the switching is destroyed.

The role of the in-plane applied field is important for the deterministic switching of the magnetization as pointed out in the Fig.4.12d. Without in-plane field reversed domains are continuously nucleated at one edge (left edge) and the control on the final state is lost.

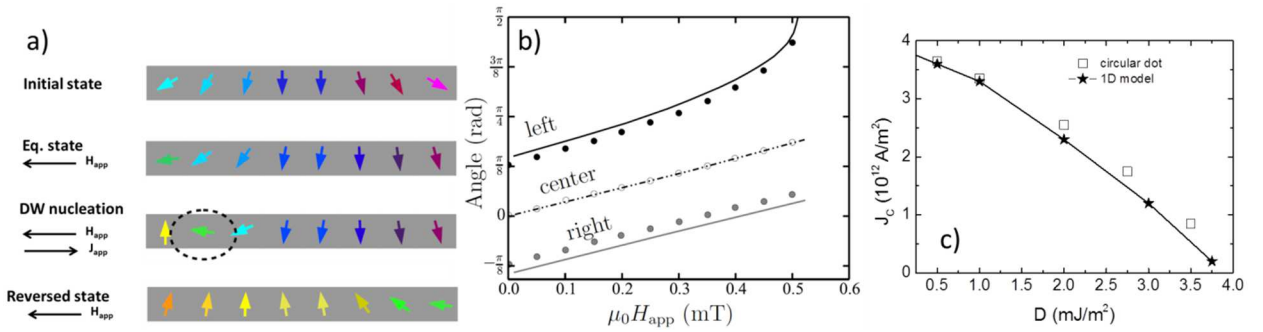


Fig. 4.13 a) Sketch of the magnetization configuration at different stages of the switching process. The current induced damping-like torque drives only the left edge magnetization into instability, resulting in a nucleation at the left edge. b) Angle of the magnetization with respect to the z-direction as a function of an applied magnetic field in the x-direction and zero current (1D model). Due to DMI the magnetization at the edges of the infinite long stripe differs from that in the center. At approximately 0.5T the first edge is fully in-plane. Note that without current and due to symmetry the maximum edge angle is always $\pi/2$. c) Critical current for destabilizing the system as a function of the DMI strength and comparison between 1D model and micromagnetic results [Mikuszei2015].

In parallel with the micromagnetic numerical model a simple analytical model was developed which describes the reversal process in the presence of both DMI and SOT by using a Lagrangian approach. Hence, the magnetization reversal scheme can be explained in a simplified manner by considering the combined effect of DMI, external magnetic field, and SOT, but neglecting small variations of the demagnetizing field. The DMI is too small to induce a spin spiral but results in a magnetization canting at the dot edges. The edge canting can be considered as an additional effective field with spatial variation: on one side this field adds to the in-plane applied field, while it counteracts on the other. This leads to an asymmetric tilting of the magnetization on both edges (Fig.4.13a-b). Upon current injection the *damping-like* torque emerges. Its effect can be interpreted as a rotating magnetic field of the form $\mathbf{H}_{DL} \propto J_{app} \mathbf{m} \times \hat{\mathbf{y}}$. This leads to a rotation of the magnetization toward the film plane on one side

and away from the film plane on the other. Naturally, the current polarity is chosen such that the stronger tilted edge magnetization turns towards the film plane. Above a critical current an instability occurs, leading to domain nucleation and consecutive DW propagation. It is clear that the current J_c , required to introduce the instability, reduces with increasing DMI. This behavior is seen in Fig. 4.13c, where J_c tends to zero when $D \approx 3.8\text{mJ/m}^2$. After expelling the DW on the opposite side, switching has occurred and the more tilted edge appears on the opposite side. As the SOT rotates this side away from the film plane and is not sufficient to rotate the less tilted side into instability, the state is, hence, stable. A good agreement is obtained between micromagnetic simulations for a 100nm diameter dot (circles) and the 1D model. For D tending to zero, the nucleation current tends to the critical current predicted by the macrospin model $J_c = 4.1 \times 10^{12} \text{ A/m}^2$ (supposing coherent rotation of the magnetization during the reversal).

One practical parameter is the switching time. The validation of the reversal mechanism presented above requires a detailed analysis of how the switching time varies with respect to different sample parameters. In Fig.4.14a the switching time is shown as a function of $J_{app} > J_c$. With increasing J_{app} the switching time decreases rapidly as the DW velocity increases. If D is reduced, the DW propagation is slower, resulting in a larger switching time. Fig.4.14b shows J_{app} versus $1/t_0$ for $D = 2 \text{ mJ/m}^2$: a linear scaling is observed, in qualitative agreement with experiment.

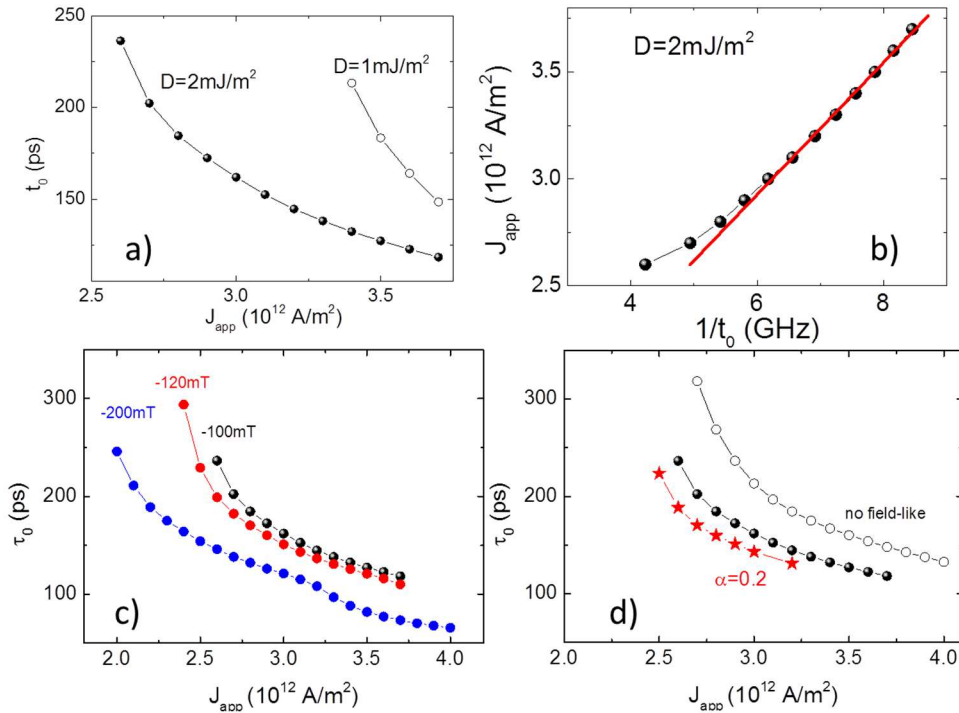


Fig. 4.14 a) Relation between the critical current and the switching time t_0 for two different DMI amplitudes. b) The same data for $D = 2 \text{ mJ/m}^2$, but in a transformed coordinate system J_{app} versus $1/t_0$. c) Switching time as a function of applied current density for different values of the in-plane applied field. d) Impact of the damping parameter and field-like torque on the switching time. The black dots are corresponding to the normal simulation conditions with field-like term and $\alpha=0.5$.

We have studied in detail the influence of the applied field, the damping constant and the amplitude of the *field-like* torque. Variations of these parameters lead to quantitative changes of the nucleation current as well as of the switching time Fig.4.14c-d. In all cases this is mainly attributed to changes in the DW velocity: a lower damping increases the domain wall velocity and so does an in-plane field, as it promotes and stabilizes a Néel type wall. A negative

field like torque also stabilizes the DW, while a positive one destabilizes it, therefore increasing the switching time. The edge nucleation/DW propagation mechanism, however, is not affected.

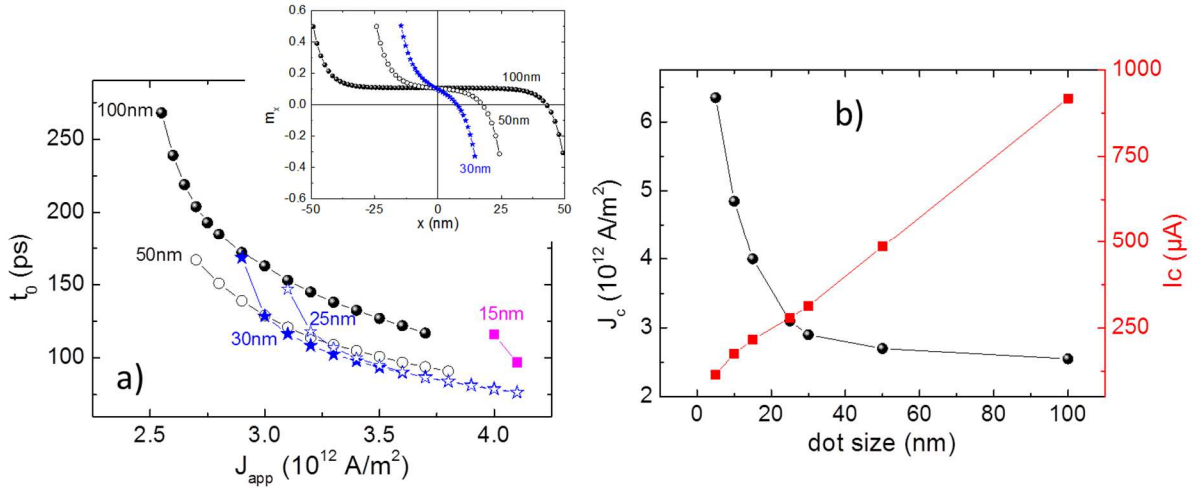


Fig. 4.15 a) The switching time versus current for different dot diameters. Inset: Cross section showing m_x for different dot diameters and a 100mT applied field x -direction. Within approximately 20 nm the canting at the edge decays towards a homogeneous magnetization at the dot center. b) Critical current and current density for different dot sizes. The calculation of the current assumes a 3 nm thick Pt line.

The mechanism of magnetization reversal was found to be robust for a dot of 100nm lateral size and moreover it is a very fast process ~ 150 ps. From practical point of view this switching time, t_0 is a key parameter. Its evolution with current density for several dot sizes is shown in Fig. 4.15a. Upon decreasing the diameter from 100 nm down to 50 nm, a shift to shorter switching times is observed while a slightly higher onset current is found. Similar behavior is found when decreasing the size down to 30 nm and further down to 25 nm. It is, however, important to note that the latter two graphs become identical for larger J_{app} . Reducing the size down to 15 nm results in a dramatic increase of the threshold current density. Moreover, deterministic switching is observed in a narrow current density region only. Overall one has indications for three different size-dependent switching regimes. In the first regime the switching is covered by domain nucleation and propagation of a DW and the decrease of t_0 is mainly caused by a reduced distance for the DW to travel. In the second regime the switching remains governed by DW propagation. The diameter, however, becomes comparable to approximately twice the value of $\xi = 2A/D \approx 10$ nm, the characteristic length scale on which canting of the edge magnetization is observed. In this situation the edge angle due to DMI differs from the ideal infinite case and opposite edges are not completely independent anymore. While this does not cause coherent rotation yet, it affects the DW motion. The coherent regime is reached at diameters in the range of the DW width $\Delta = \pi\sqrt{A/K_{eff}} \cong 14$ nm. This explains the significant change in switching behavior for the 15 nm dot. Note that the switching current at this size is close to the one predicted by macrospin simulation (4.1×10^{12} A/m²).

From practical point a view it is worth mentioning that while the current density strongly increases with decreasing dot diameter, the current in the 3 nm thick Pt stripe decreases almost linearly, as can be seen from Fig. 4.15b. Therefore, the device exhibits favorable scaling behavior and assuming a 1 k Ω resistance for the addressing transistor of a 30 nm dot, switching in about 300 ps, needs only 20 fJ for one switching event, which is comparable with the writing energy for perpendicular spin-transfer torque devices.

The last point addressed by modelling concerns the impact of the thermal fluctuations on the stochastic process of the switching probabilities. This is done by evaluating 100 independent switching events for each parameters set. For each event the switching time t_0 , i.e. the time for $\langle m_z \rangle$ to cross zero is determined and the integrated probability is calculated. A typical result is shown in Fig. 4.16a. The overall switching time in the presence of thermal fluctuations is then defined as the time for which the integrated probability reaches 90%. Naturally, the switching time decreases with increasing current density. Most importantly Fig. 4.16b shows that the switching mechanism by nucleation and propagation is very robust against thermal fluctuations. These thermal fluctuations strongly decrease the threshold current: temperature effectively lowers the nucleation barrier, such that nucleation times get shorter and, consequently, the whole switching becomes faster.

It has to be pointed out that the nucleation still takes place at the same position on the dot edge and the overall process remains bipolar with respect to field and current. This robustness against thermal fluctuations, however, strongly relies on the large damping, as can be seen from Fig. 4.16c. With decreasing α an increasing tendency for oscillations is observed, such that deterministic switching cannot be guaranteed.

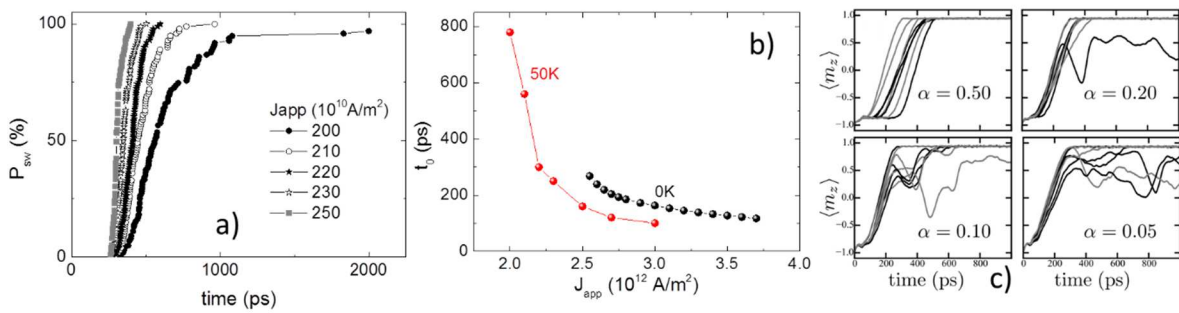


Fig. 4.16 a) Accumulated switching probability as function of time for different current densities at 50 K. b) Switching time as a function of applied current density at 0K and 50K. For the 50K case, the average t_0 is plotted (defined as the time for which the probability of stochastic switching reaches 90%). c) Several switching graphs $\langle m_z \rangle(t)$ for varying damping at 50 K, $J_{app} = 2.6 \times 10^{12} A/m^2$ and $\mu_0 H_{app} = -0.1 T$. For a given α , the variations are only due to thermal fluctuations.

To conclude this switching mechanism via chiral domain nucleation explains the deterministic switching observed experimentally in ultrathin Pt/Co/AlOx even for sub-ns pulses. The switching is mainly induced by the *damping-like* torque, but the *field-like* torque cannot be neglected as it strongly influences the switching time. Our systematic studies show a change in the reversal mechanism for diameters below 30 nm, while the switching remains deterministic and bipolar. However, at 0 K the current densities operational window decreases with decreasing dot diameter. Most importantly, current scalability is maintained. This confirms the potential of SOT-MRAM for scalable fast non-volatile memory application.

Independent of magnetization reversal mechanism, the MRAM operation imposed long data retention, fast and reliable commutation with very small power consumption. The above presented four types of memory cells are trying to address the memory challenges. Improvement is still possible and many questions are still waiting for answers, as presented in the next chapter.

Chapter V: Prospective activities

Short and long term research topics are listed hereafter. There is a continuity of the objectives from my past activity: understanding the mechanisms behind the magnetization dynamics driven by various types of excitation and their use in conceiving/optimizing devices. The strong interaction between the modelling activity and the experimental investigations will allow to preserve the coherence theory/real samples and accelerate the progress in the field of spintronics.

The interest on spintronic devices is continuously growing as confirmed by the number of publications, conferences and patents on this topic. Beyond the traditional applications to data storage and magnetic field sensors, after years of intense research well established concepts as MRAM become products on the market. This transfer from research stage to commercial available products is extremely encouraging for plenty other spintronic concepts. The recent progresses in spin transfer physics allow a widening of the application spectra for spintronic devices, notably toward multifunctional devices relying on their nonvolatile nature, scalability, and compatibility with existing CMOS technologies. The efforts of the spintronic community are reinforced on several directions:

- improvement/optimization of existing concepts to reduce the gap towards the requirements imposed by the applications (e.g. reduction of the emission linewidth for the STNO) to be able to go beyond the proof of concept
- development of novel devices both at concept and design levels (e.g. non-volatile FPGA, logic circuits,..)
- extension towards the IoT products (e.g. wireless sensors network)
- take benefit of the non-volatility of spintronic concepts in energetically very efficient devices (neuromorphic inspired circuits,...)
- combine spintronics with other phenomena (thermal, optical,...) going towards multi-physical based concepts

The future activity in simulation is meant to follow the same trends since, as by the past, the modelling is a tool of investigation strongly connected with the experimental work. Hereafter the future directions for the modelling are presented, most of them being natural evolutions of the previous studies.

5.1 Magnetic random access memories : push further the limits

STT-MRAM, in its latest *perpendicular* implementation (e.g. with the magnetization pointing perpendicular to the wafer surface), is now viewed as the solution of choice for embedded non-volatile memory (e.g. embedded Flash and embedded SRAM) at advanced technology node. Industrials such as *Samsung*, *IBM*, *Global Foundries* and *TSMC* have embarked into extensive development programs and have announced products release in 2018. Others smaller companies are already selling product: e.g. *Everspin*, announced in March 2017 several new applications and customers for its STT-MRAM solutions, while *Spin Transfer Technology* announced in January 2017 that it started to deliver fully functional STT-MRAM samples to customers in North America and Asia. These memories combine CMOS compatibility, high retention time (10 years), large endurance ($>10^{12}$ cycles) and relatively fast write/read time (~ 10 ns).

The challenges now are orientated to push higher the memory speed and the integration density. Results have shown very fast switching (sub-ns) using stacks where the magnetizations

of the storage and the polarizer layers are perpendicular, but this gain in speed comes at the expense of current switching and voltage applied across the tunnel barrier. As a consequence, manufacturers are currently facing important reliability issues due to the accelerated aging of the tunnel barrier when injecting these large current densities. Another important issue is that the read and the write use the same current path. Variability of read/write parameters results in undesired writing while reading as well as a high read power since the tunnel barrier needs to have a very small resistance to accommodate the large writing current densities. Manufacturers are seeking for solutions through optimization of the materials composing the stack, with many interdependent parameters (write/read signal, energy consumption, writing speed, resistance, retention, endurance ...) intrinsic to such two-terminal device.

For perpendicular STT-MRAM, a joint numerical and experimental study allows us to conclude on the existence of a corrective term in the anisotropy (2nd order contribution, section 4.3) with a valuable impact on the switching of the memory cell. However the control of this feature and its efficient handling requests a deeper understanding of its origin. Our first attempts based on the idea of spatial modulation of the interfacial anisotropy (Fig.5.1) are indicative for an existing easy-cone like behavior described by an effective 2nd order contribution to the anisotropy. From our experience the second order correction of the anisotropy seems to be quite general feature of CoFeB based samples

fabricated internally at Spintec or by our partners. Moreover the thin magnetic layers studied for MRAM applications are in same time integrated in devices for other kinds of experiments (e.g. SOT magnetization reversal). Thus the predictions supplied by the micromagnetic modelling on this subject will be actually important for other activities.

Additional investigations are mandatory also to see the impact of anisotropy control by electric field since during the writing voltage pulse the anisotropies of various layers from the nanopillar are susceptible to change.

Large variety of samples have been fabricated and characterized both electrically and magnetically. Most of the observations can be argued in the frame of existing models. However, the experimental observations have revealed special cases of behaviors whose interpretation is far to be understood. Stability voltage-field diagrams of full perpendicular STT-MRAM are showing that the dynamic of the magnetization of the polarizer itself (usually a SAF structure) must be accounted since the shape of the critical lines (Fig. 5.2b) is far from the independent free-layer model predictions (Fig. 5.2c). The model of coupled layers previously developed for oscillators should be extended for the perpendicular geometry (both numerical and analytical level). The main objective is to get insight on the evolution of the stability field-voltage diagrams as a function of various types of couplings or variation of parameters.

It is important to know how various critical lines (Fig. 5.2d) are affecting the diagrams and especially to point out the impact on the operation of memory cell. The coupling between the layers in most of the cases is seen as being detrimental for the properties of the device, affecting the robustness and the stability. However the coupling might be also a parameter of adjustment to reduce the level of the writing voltage and thus optimize the memory point (endurance, consumption). Since the coupling generally might be reduced but not suppressed,

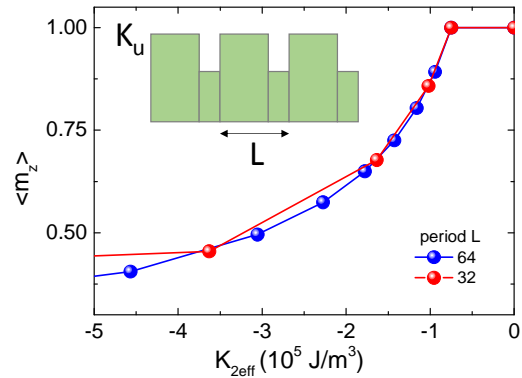


Fig. 5.1 Magnetization tilting generated by a periodic spatial modulation of the 1st order anisotropy constant K_u in a thin film with 2D periodic structure.

finding the suitable balance between detrimental/beneficial impacts is a complete task from modelling point of view.

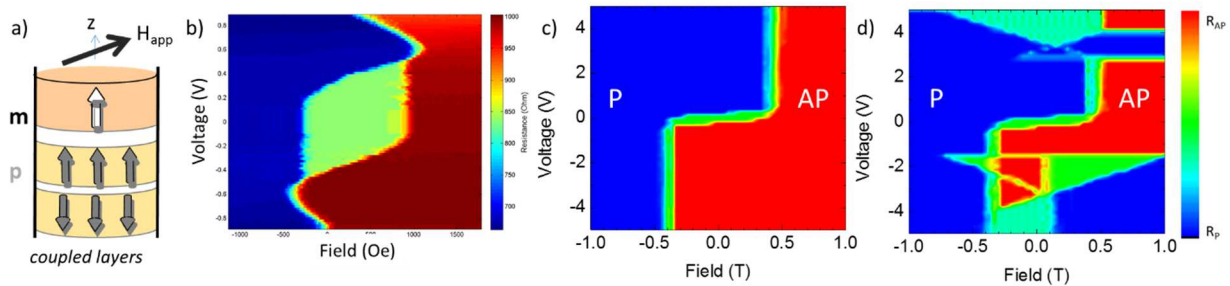


Fig. 5.2 a) Schematics of typical full perpendicular STT-MRAM cells based on spin transfer torque. b) Experimental stability field-voltage diagram (private communication Van Dai Nguyen). Simulated field-voltage diagram of an isolated free layer (c) and mutually coupled 3 layers d) (N. Perrissin). The applied field is longitudinal with the vertical z easy axis.

The ICT industry has long been looking for a non-volatile memory technology that would be fast enough to match processor speed (in the GHz regime), reliable and durable (e.g. infinite endurance) to act as cache, whilst being denser (e.g. a smaller bit cell size) than SRAM and easy to embed to be cost-effective. No technology today combines such a set of properties. The SOT-MRAM proposed in the frame of EU grant spOt (see 4.4) is the only option to offer such promises. The concept of the Spin Orbit Torque MRAM is a three-terminal device allowing to differentiate between the writing and reading path and thus ensuring infinite endurance. The experimental and numerical studies on single cells have demonstrated sub-ns bipolar deterministic switching down to 180ps with a minimum in the write energy observed between 1 and 3 ns. These memories are compatible with technological nodes below 22nm.

Based on these indications, the SOT-MRAM should operate at standard SRAM caches speed. Furthermore it will provide zero standby power, zero leakage and data security thanks to its non-volatile nature, together with a much lower cost per bit and potentially larger memory capacities (e.g. much smaller bit cell size). The SOT-MRAM technology will drastically improve the power consumption, the performances and the cost of the future generations of microprocessors.

Moving from the bit-cell level approach toward very large-scale integration, requires significant work at the memory/system level. More particularly, efficiency, variability and reliability are key issues for an emergent technology to be brought at its level of maturity. As for the STT-MRAM the modelling will be useful tool to reveal the causes of the variability and reliability of the read and write processes. The simulation will focus on the distribution of magnetic parameters (various terms of anisotropy, DMI, amplitude of the *damping-like* SOT vs *field-like* SOT or Oersted field), inhomogeneous thickness, distribution of the dimensions, edge defects. Analytical modelling based on LLG-macrospin equations or nucleation/propagation models (collective coordinate model) and micromagnetic simulations (including the effects of the temperature and nanofabrication defects) will be carried out and compared with experimental results. The outcomes of the modelling should allow to identify possible routes of optimization and improvement of reliability.

The above mentioned studies need input from experiments but also from theory, collaboration internally with M. Chshiev is welcome as support. The confrontation with experiments is mandatory for the calibration of the models but also to extend the design tools developed by our colleagues at Spintec (G. Prenat, G. Di Pendina, F. Duhem).

5.2 Exploring new STNO concepts

The nanopillars used for memory applications are often quite similar to that used for STNO. The understanding of the mechanisms of the spin transfer torque (STT) on the magnetization reversal is extrapolated also to the STNO based on the self-sustained magnetic oscillations in the GHz range. Our studies on the 2nd order anisotropy correction carried for MRAM revealed also the suitable conditions to induce magnetization precession and not only magnetization switching (*Fig.5.3*). Once the easy-cone state is stabilized at zero applied field, the STT drives easily the magnetization motion on the cone. The frequency varies linearly and symmetrically with the applied DC voltage. The preliminary studies converge both numerically (macrospin and micromagnetic simulation) and analytically (extended *c*-model) indicative for a small threshold voltage. The quality of the oscillation must be further investigated, the linewidth of emission peak and the non-linearity parameter before projecting to build experimentally such an oscillator.

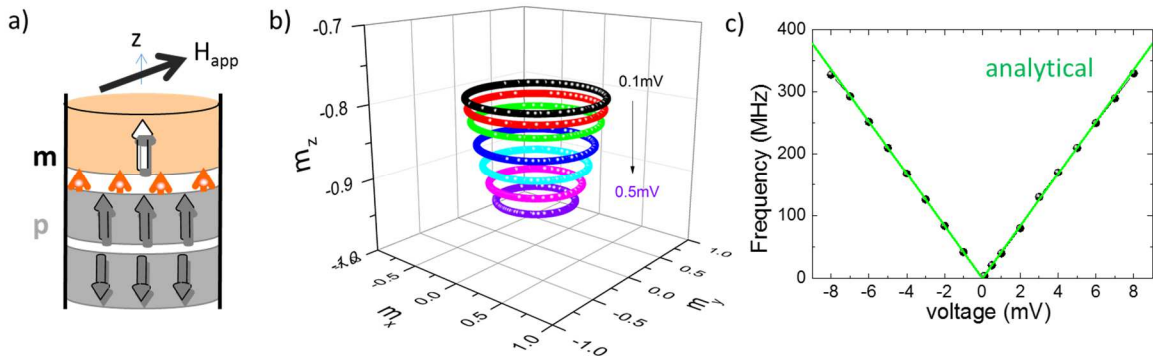


Fig. 5.3 a) Schematics of typical perpendicular nanopillar. The magnetization m of the top layer is intrinsically tilted by a 2nd order anisotropy term. b) Varying the DC applied voltage the magnetization describes steady trajectories on the easy-cone. c) The numerical and analytical predictions indicate a linear dependence of the emission frequency versus applied voltage.

The possibility of exciting the magnetization dynamics by spin orbit torque was addressed in section 2.3 for the magnetic domain walls displacement and section 4.4 SOT-MRAM. We are targeting to explore also the possibility of stabilizing steady oscillation. Preliminary investigations have been done during the PhD of M. Fabre and will be pursued having as objective to find optimum operation conditions (non-linearity, tunability, line-width).

5.3 STNO for intra- and inter-chip communication

Spin torque transfer RF oscillators based on giant magnetoresistance spin-valves or MTJ are very interesting frequency tunable devices which could be used for *RF emission* and *detection* at frequency ranging from 100MHz to 70GHz [Kiselev2003]. The STNOs have been intensively studied in the last decade in order to improve the understanding of the mechanisms of the spin transfer torque (STT) as well as the physics of high frequency nonlinear magnetization dynamics. On one hand, this effect contributes in certain limits to a broadening of the spectral linewidth, deteriorating the quality factor of the STNOs. On the other hand, STNOs appear as model nanoscale systems for studying the effects of synchronization, notably in the regime of large nonlinearities and even their tendency to reach chaotic regimes under the influence of spin transfer forces. Significant progresses were made over these years both in the understanding and performances of these devices. However, they still suffer from insufficient

output power and excess phase noise for applications. To address these issues, various attempts to synchronize oscillators through spin-waves, magnetostatic interactions or by electrical serial or parallel connections were made but with moderate success (up to 3 or 4 oscillators synchronized) [Sani2013]. WIFI communication at 1m distance was demonstrated using double-amplified STNO RF signal and transmission of information via amplitude modulation/demodulation at data rate of 1.48Gbit/s [Choi2014]. These promising results can certainly be improved by using more powerful synchronized STNO with narrower linewidth and parallel multiband emission/detection. In this context, the very large frequency tunability of STNO (e.g. the frequency can be varied from 8 to 12GHz depending on the DC current) makes these devices very interesting for the very broadband technologies required in future wireless communication schemes.

Besides, these STNO can turn out to be very useful for intra-chip or inter-chip RF interconnects. Traditional metal wiring interconnect technology more and more appears as a major bottleneck to the performance improvement of very large-scale integration systems. Non-wiring interconnect solutions are being intensively explored such as optical interconnects or inductive or capacitive coupling. However, these technologies have also their own problems and limitations. In this context, RF interconnects through free space appear to have a strong potential for instance for clock distribution network or vertically stacked die to die communication in 3D integration [Tao2008]. Such concepts were explored with conventional RF transceiver circuits comprising rather large on-chip transmitter and receiver antenna (mm size). Along these lines, these extremely small STNO (<100nm) and spin-transfer diodes (STD) offer totally new opportunities for intra- and inter-chip communication with much reduced sizes and improved performances compared to conventional RF technology.

The evaluation of STNO for intra- and inter-chip communication is part of the EU Advanced Grant **MAGICAL CMOS /Magneto-electronic Integrated Circuits with Multifunctional Capabilities** coordinated by B. Dieny. The objective is to achieve synchronization of large number of STNOs exhibiting very similar properties and being very strongly intercoupled by magnetostatic interactions and/or by direct exchange.

In particular, very closely spaced arrays of STNO (10-20nm edge to edge spacing) and chains of adjacent cylindrical STNO will be investigated (lateral size of nanopillar ~150-50nm). The N synchronized STNO should yield high output power and low phase noise. Single STNO and synchronized assembly of STNOs will also be used as rectifying spin-torque diodes (STD) to detect RF field with sensitivities larger than conventional semiconductor Schottky diodes by exploiting non-linear FMR effects [Miwa2014].

- A first goal will then be to optimize these assemblies of STNO properties and combine them with amplification circuits and RF antenna to realize long distance wireless communication over large distance (~ m).

- A second goal will be to investigate the potentiality of using STNO and STD for short distance RF interconnects in particular for inter-die communication in 3D integration wherein several vertically stacked dies have to inter-communicate. Parallel communication of several STNO operating at different frequencies will be studied.

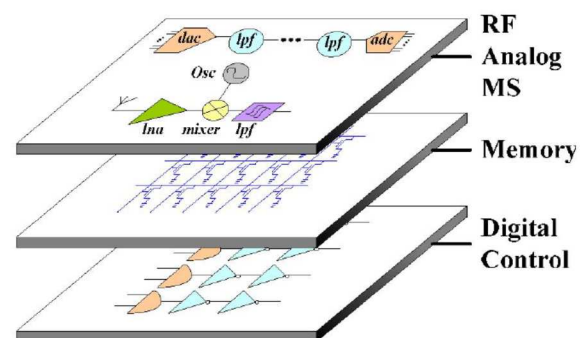


Fig. 5.4 Hybrid Circuit Integration Concept [Tao2008].

The modelling will address the STNOs synchronization in strong coupling regime. The idea is find the suitable conditions in which the assembly of STNOs is able to radiate collectively large RF stray field. The concept is similar to that proposed by Zhu et al. for microwave assisted magnetic recording [Zhu2008]. These STNO will be assembled in arrays and chains of various shapes particularly linear chains of several tens of STNOs. We will in particular use STNO consisting of a perpendicular polarizer associated with an in-plane magnetized free layer for which large angle precession were previously demonstrated [Houssameddine2007]. Very efficient synchronization due to strong favorable magnetostatic interactions occurring at each half precession can be expected in such a chain of SNT0 (Fig. 5.5). Micromagnetic simulations will be performed to study the STT induced magnetization trajectory, optimum STNO arrangements for RF field emission towards specific locations or to maximize output RF voltage, synchronization conditions, output power, linewidth, dynamic rise time, and frequency.

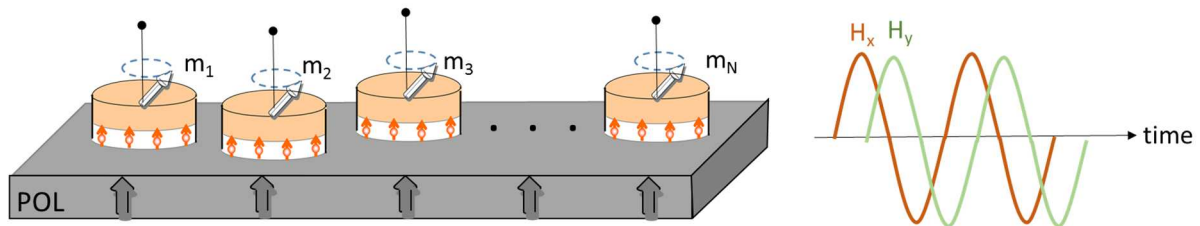


Fig. 5.5 a) Chain of synchronized STNOs aimed at generating a RF stray field in free space. They consist of a perpendicular polarizer ($[Co/Pt]_n/Co$) and an in-plane magnetized free layer separated by a non-magnetic Cu spacer. All the STNO are traversed by a perpendicular DC current which generates a large angle precession of the free layer magnetization by STT.

5.4 Multifunctional standardized stack

The interest for developing smart systems based on interconnected objects (Smart Sensors, Secure Elements for the Internet of Things...) is growing fast. It is assumed that 50 billion objects will be connected in 2020. The main components of IoT devices are autonomous battery-operated smart embedded systems comprising communication circuits, sensors, computing/processing devices as well as integrated memories. Consequently, the key requirements for IoT devices are ultra-low power, high processing capabilities, wireless communication, and autonomy. These smart connected devices embedded RF circuits for communications, digital circuits for data processing, memory for data storage as well as analog circuits such as sensors, filters, converters, not to mention cameras, GPS systems etc. In battery operated *Machine to Machine* (M2M) and *Machine to Human* (M2H) operations, the key processing cycle includes the actions sleep, wake-up, sense, store, process, and send. The goal of the GREAT (*heteroGeneous integRated magnetic tEchnology using multifunctional stANDARDized sTack*) project is to co-integrate multiple functions like sensor, RF receivers and logic/memory together within CMOS. The main idea consists on adapting the STT-MTJs magnetic devices to a single baseline technology enabling logic, memory, and analog functions in the same System-on-Chip (SoC) as the enabling technology platform for M2M and M2H IoT. This will lead to a unique STT-MTJ cell technology called Multifunctional Standardized (MTJ) Stack (MSS).

The multifunctional standardized stack (MSS) must allow realizing memory, logic, spin-transfer-oscillator and sensor functionalities without sacrificing on the performances of each function. To achieve this, we intend to use as MSS out-of-plane MTJs as those currently optimized for STT-MRAM in combination with patterned permanent biasing magnets (for instance made of CoCr alloy or NdFeB) on the two sides of the MTJ pillars, as this is done to bias magnetoresistive heads in hard disk drives. The key idea here is to change the size and shape of the permanent magnets and the size of the MTJ so that the value of the magnetic field and the parameters of the MTJ stack are in good agreement to perform the good function.

The micromagnetic modelling should allow to investigate the static and dynamic behaviors of the free layer magnetization of MTJ under magnetic field and spin-polarized current. Different shapes (circular and elliptical with aspect ratio from 1.2 to 3) and sizes (from 20nm to 500nm) will be numerically investigated in order to understand and optimize the switching behavior for memory applications or the excitation spectra (base frequency range, frequency tuning with current and field, output power, rectification, modulation and synchronization capabilities, ...) for RF applications. RF applications will also consider the possibility to excite the pinned layer by current sign reversal. Pinned layer excitations can provide improved properties in terms of phase noise. In a second step, the thermal fluctuation influence on the MTJ properties will be taken into account (e.g. linewidth for RF functions, thermal stability for switching and sensing).

5.5 Memristive magnetic memories for spintronic synapses

Conventional electronic circuits consume much more energy than human brain at similar performances. Consequently, there is a strong interest in developing electronic circuits which mimic the working principle of the brain. These circuits are particularly suited for learning functions, associative functions, pattern recognition etc. For that purpose, it is necessary to develop new electronic components which realize neurons or synaptic functions. Synapses are interconnection elements between neurons able to keep the memory of the history of the current pulses to which that have been submitted. We propose to develop such electronic synapses based on spintronic phenomena and particularly on the tunnel magnetoresistance of MTJ. The resistance of such component must continuously vary between a minimum and maximum value depending on the sequence of current pulses sent though the component [Chua1971]. Such components are called memristor (memory resistor).

Today, in the field of spintronics, a first category of such component was developed based on magnetic domain wall displacements [Locatelli2014]. The team of J. Grollier at UMR-CNRS Thales [Lequeux2016] shown the possibility to have several pinning events of a DW in stripes perpendicularly magnetized and consequently various levels of resistance are accessible. MTJ based neuromorphic circuits were investigated by simulation D. Querlioz at IEF Orsay combining several MTJ cells stochastically written [Vincent2015]. Experimental attempts based on spin orbit-torque are also been recently published [Fukami2016, Border2017] but the size of the Hall crosses is still very large few μm .

Here, we propose a different approached based on the angular orientation of the storage layer magnetization in magnetic tunnel junctions. This type of junctions are already used in a binary way for binary memory functions (MRAM or STT-MRAM). We propose to modify the working principle of these junctions to be able to reach all intermediate states between R_{\min} and R_{\max} thus realizing the memristor function.

The nanopillar has a similar structure with that of the perpendicular STNO [Houssameddine2007] or the precessional STT-MRAM [Vaysset2011] (Fig.5.6a). Our previous studies have shown that by STT the magnetization of the free layer can be switched or driven in steady precessional state. For a memristor application, we need to change progressively the orientation of the magnetization of the free layer with a sequence of voltage pulses. Thus, the free layer material should have isotropic properties in the plane and a damping parameter relatively large. With pulses of few ns the magnetization of the free layer must rotate few degree away from the initial state.

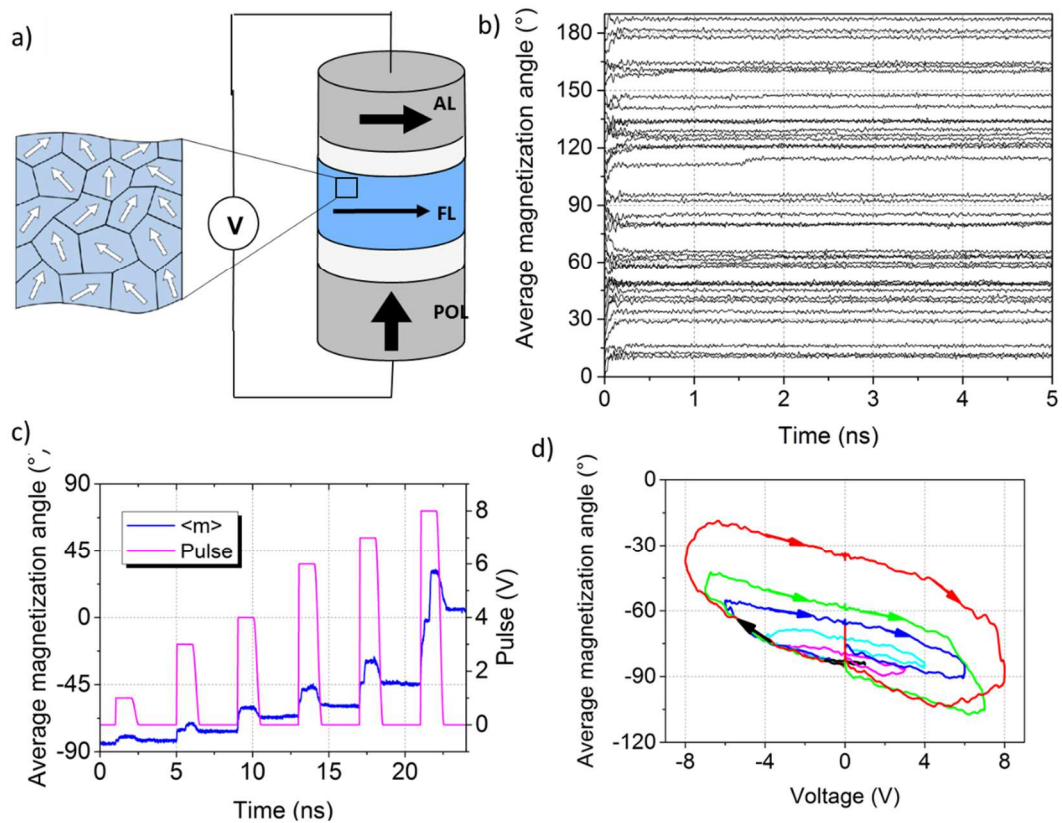


Fig. 5.6 a) Schematic view of the nanopillar with an in-plane magnetized free-layer (FL) with granular structure. b) Various in-plane stable states of a 240nm diameter dot. c) Sequence of voltage pulses allowing to commute between various stable states. D) memristor-like loop obtained upon varying the voltage pulse duration [Mansueto2017]

Our preliminar micromagnetic studies considering a free layer with a granular structure and in-plane randomly distributed anisotropy are the first attempt (Fig.5.6b-d). In a 240nm diameter nano-pillar more than 20 stable states were identified. The injection of 1ns pulses of current with different polarities enabled the commutation between the states and thus a memristor-like behavior is predicted. The topic will be further developed in the next 3 years with the PhD thesis of Marco Mansueto.

5.6 Modelling tools

The realization of the above mentioned future projects is conditioned by the evolution of the numerical tools. The package of numerical tools is in continuous evolution. In 2016 the transition of Micro3D on GPU has been initiated in the frame of the post-doc of Nikita Strelkov. The model is a phenomenological one with several choices of additional terms to be accounted. The flexibility of including distribution of various parameters is key feature of the code being mandatory for the future studies.

The macrospin at first glance is seen as being simple model but drawing diagrams and carrying on statistical analyses is still time consuming. Specific solvers are under development allowing to use the local GPU cards with user friendly interface.

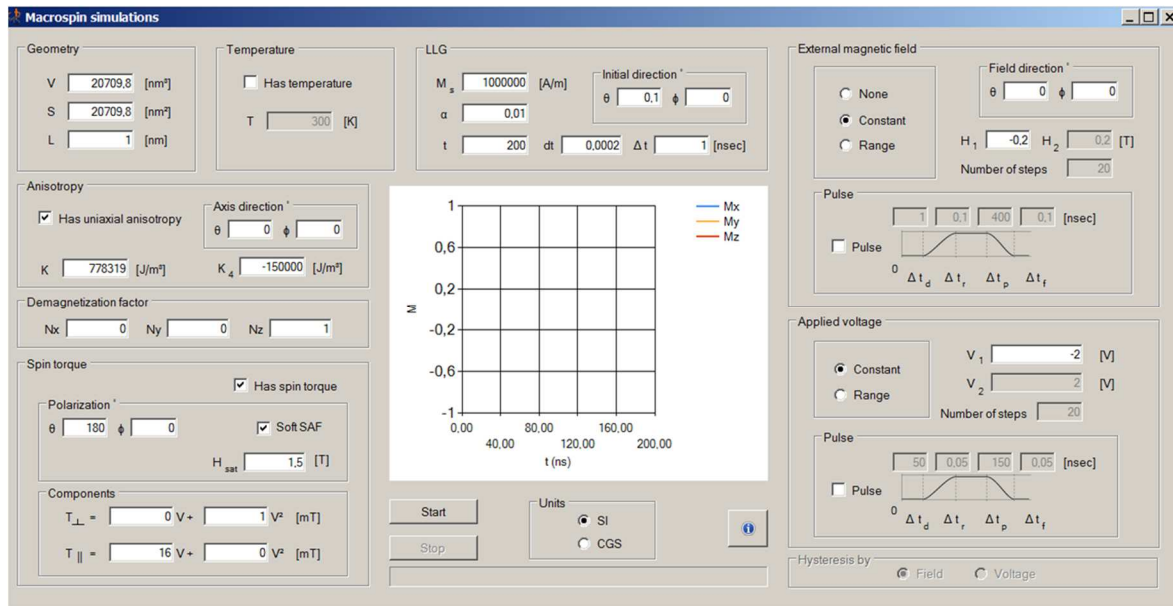


Fig. 5.7 Spintec Macrospin solver interface.

References

- [**Belanovsky2013**] A.D. Belanovsky, N. Locatelli, P.N. Skirdkov, F. Abreu Araujo, K.A. Zvezdin, J. Grollier, V. Cros, A.K. Zvezdin, *Numerical and analytical investigation of the synchronization of dipolarly coupled vortex spin-torque nano-oscillators* Appl. Phys. Lett. **103**, 122405 (2013).
- [**Berger1996**] L. Berger *Emission of spin waves by a magnetic multilayer traversed by a current*, Phys. Rev. B **54**, 9353 (1996).
- [**Bollero2011**] A. Bollero, L. D. Buda-Prejbeanu, V. Baltz, J. Sort, B. Rodmacq and B. Dieny *Magnetic behaviour of systems composed of coupled ferromagnetic bilayers with distinct anisotropy directions* Phys. Rev. B **73**, 144407 (2006).
- [**Border2017**] W. A. Borders, H. Akima, S. Fukami, S. Moriya, S. Kurihara, Y. Horio, S. Sato, and H. Ohno *Analogue spin-orbit torque device for artificial-neural-network-based associative memory Operation* Appl. Phys. Express **10**, 013007 (2017).
- [**Boulle2013**] O. Boulle, S. Rohart, L. D. Buda-Prejbeanu, E. Jué, I.M. Miron, S. Pizzini, J. Vogel, G. Gaudin, A. Thiaville *Domain wall tilting in the presence of the Dzyaloshinskii-Moriya interaction in out-of-plane magnetized magnetic nanotracks* Phys. Rev. Lett. **111**, 217203 (2013).
- [**Boulle2016**] O. Boulle, J. Vogel, H. Yang, S. Pizzini, D. de Souza Chaves, A. Locatelli, T. O. Mendes, A. Sala, L. D. Buda-Prejbeanu, O. Klein, M. Belmeguenai, Y. Roussigné, A. Stashkevich, A. M. Cherifi, L. Aballe, M. Foerster, M. Chshiev, S. Auffret, I.M. Miron, G. Gaudin *Room-temperature chiral magnetic skyrmions in ultrathin magnetic nanostructures* accepted Nature Nanotechnology 11(5) 449 (2016).
- [**Braganca2010**] P. M. Braganca, B. A. Gurney, B. A. Wilson, J. A. Katine, S. Maat, and J. N. Childress, *Nanoscale magnetic field detection using a spin torque oscillator* Nanotechnology **21**, 235202 (2010).
- [**Brown1957**] W. F. Brown, *Criterion for uniform micromagnetization*, Phys. Rev. **105**, 1479 (1957).
- [**Brown1963**] W. F. Brown, *Thermal fluctuations of a single-domain particle*, Phys. Rev. **130**, 1677 (1963).
- [**Buda2002**] L.D. Buda, I.L. Prejbeanu, U. Ebels, K. Ounadjela *Micromagnetic simulations of magnetization in circular cobalt dots* Computational Material Science **24**, 181-185 (2002)
- [**Buschow2003**] K. H. J. Buschow and F. R. de Boer, *Physics of Magnetism and Magnetic Materials*, Kluwer, New York (2003).
- [**Burrowes2010**] C. Burrowes, A. P. Mihai, D. Ravelosona, J.-V. Kim, C. Chappert, L. Vila, A. Marty, Y. Samson, F. Garcia-Sanchez, L. D. Buda-Prejbeanu, I. Tudosa, E. E. Fullerton and J.-P. Attané *Non-adiabatic spin-torques in narrow magnetic domain walls* Nature Physics **6**, 17 (2010).
- [**Choi2014**] H.S. Choi S. Y. Kang, S. J. Cho, I.-Y. Oh, M. Shin, H. Park, C.Jang, B.-C. Min, S.-I. Kim, S.-Y. Park and C. S. Park, *STO-based wireless communications*, Scientific Reports **4**, 5486 (2014).
- [**Chua1971**] L. O. Chua, *Memristor - the missing circuit element* IEEE Trans. Circuit Theory **18**, 507 (1971).
- [**Consolo2010**] G. Consolo, V. Puliafito, G. Finocchio, L. Lopez-Diaz, R. Zivieri, L. Giovanni, F. Nizzoli, G. Valenti, and B. Azzerboni, *Combined Frequency-Amplitude Nonlinear Modulation: Theory and Applications* IEEE Trans. Magn. **46**, 3629 (2010).
- [**DieudonnéPhD**] C. Dieudonné, *Synchronization of a spin-transfer oscillator to a RF current: Mechanisms and characterization at room temperature*, Université Grenoble Alpes (2015)
- [**Ebels2001**] U. Ebels, L.D. Buda, K. Ounadjela, P.E. Wigen *Ferromagnetic resonance excitation of two-dimensional wall structures in magnetic stripes domains* Phys. Rev. B **63**(17), 174437 (2001).
- [**Ebels2007**] U. Ebels, B. Dieny, I. Firastrau *Oscillateur à couple de transfert de spin* No WO-2007/051676 (21/02/2007)

[**Ebels2003**] U. Ebels, L.D. Buda, I.L. Prejbeanu, M. Natali *Circular magnetic elements: ground states, reversal and dipolar interactions* NATO-Science Series vol. 91, p. 193-211, éditeurs L.M. Liz-Marzan et M. Giersig Kluwer Academic Plenum Publishers (2003).

[**FDM**] M. R. Scheinfein, LLG Micromagnetics Simulator llgmicro.home.mindspring.com
D. V. Berkov and N. L. Gorn, MicroMagus, www.micromagus.de
J. Oti, MagOasis, www.magoasis.com
A. Vansteenkiste and B. Van de Wiele, mumax.github.io
L. Torres and E. Martinez, GoParallel www.goparallel.net
A. Drews, MicroMagnum, www.micromagnumtis.informatik.uni-hamburg.de

[**FirastrauPhD**] I. Firastrau, *Développement d'un environnement de modélisation micromagnétique ; Couplage macroscopique-microscopique* InP Grenoble (2004).

[**Firastrau2008**] I. Firastrau, D. Gusakova D. Houssameddine, U. Ebels, M.-C. Cyrille, B. Delaet, B. Dieny, O. Redon, J.-Ch. Toussaint, and L. D. Buda-Prejbeanu *Modeling of the perpendicular polarizer-planar free layer spin torque oscillator: Micromagnetic simulations* Phys. Rev. B **78**, 024437 (2008).

[**Fukami2016**] S. Fukami, C. Zhang, S. DuttaGupta, A. Kurenkov and Hideo Ohno *Magnetization switching by spin-orbit torque in an antiferromagnet-ferromagnet bilayer system* Nature Mater. **15**, 535 (2016).

[**Garcia2010**] F. Garcia-Sanchez, H. Szabolcs, A.P. Mihai, L. Vila, A. Marty, J.-P. Attané, J.-Ch. Toussaint, L.D. Buda-Prejbeanu *Effect of crystalline defects on domain wall motion under field and current in nanowires with perpendicular magnetization* Phys. Rev. B **81**, 134408 (2010).

[**Georges2008**] B. Georges, J. Grollier, M. Darques, V. Cross, C. Dernalot, B. Marcillhac, G. Faini and A. Fert *Coupling Efficiency for Phase Locking of a Spin Transfer Nano-Oscillator to a Microwave Current* Phys. Rev. Lett. **101**, 017201 (2008).

[**Gilbert1955**] T.L. Gilbert *A Lagrangian formulation of the gyromagnetic equation of the magnetic field*, Physical Review **100**, 1243 (1955).

[**Gilbert 2004**] T.L. Gilbert *Classics in Magnetism A Phenomenological Theory of Damping in Ferromagnetic Materials*, IEEE Trans. Magn. **40**(6),3443 (2004).

[**Grollier2006**] J. Grollier, V. Cros, and A. Fert *Synchronization of spin-transfer oscillators driven by stimulated microwave currents* Phys. Rev. B **73**, 060409(R) (2006).

[**HemPhD**] J. Hem *Les composants spintroniques pour les applications microondes : De l'oscillateur libre vers une boucle à verrouillage de phase* University of Grenoble Alpes (2017).

[**Hubert1998**] A. Hubert and R. Schafer, *Magnetic Domains*, Springer, New York (1998).

[**Houssameddin2007**] D. Houssameddine, U. Ebels, B. Delaët, B. Rodmacq, I. Firastrau, F. Ponthenier, J.-P. Michel, L.D. Buda-Prejbeanu, M.-C. Cyrille, O. Redon, B. Dieny *Spin-torque oscillator using a perpendicular polarizer and a planar free layer* Nat. Mater. **6**(6) 447-453 (2007)

[**Houssameddine2008**] D. Houssameddine, S. H. Florez, J. a. Katine, J.-P. Michel, U. Ebels, D. Mauri, O. Ozatay, B. Delaet, B. Viala, L. Folks, B. D. Terris, and M.-C. Cyrille. *Spin transfer induced coherent microwave emission with large power from nanoscale MgO tunnel junctions* Appl. Phys. Lett. **93**, 022505, (2008)

[**Jabeur2014**] K. Jabeur, G.Prenat, G.Di Pendina, L.D.Buda-Prejbeanu, B.Dieny *Compact model of a magnetic tunnel junction based on spin orbit torque* IEEE Trans. Magn. **50**, 4100208 (2014)

[**Kittel1948**] C. Kittel *On the Theory of Ferromagnetic Resonance Absorption*, Phys. Rev **73**, 155 (1948).

[**Kiselev2003**] S. I. Kiselev, J. C. Sankey, I. N. Krivorotov, N. C. Emley, R. J. Schoelkopf, R. A. Buhrman, D. C. Ralph *Microwave oscillations of a nanomagnet driven by a spin-polarized current*, Nature **425**, 380 (2003).

- [**Landau1935**] L. D. Landau and E. M. Lifshitz, *On the theory of the dispersion of magnetic permeability in ferromagnetic bodies*, Phys. Z. Sowjet. **8**, 153 (1935).
- [**Lequeux2016**] S. Lequeux, J. Sampaio, V. Cros, K. Yakushiji, A. Fukushima, R. Matsumoto, H. Kubota, S. Yuasa and J. Grollier *A magnetic synapse: multilevel spin-torque memristor with perpendicular anisotropy*, Scientific Reports **6**, 31510 (2016).
- [**Li2001**] S.P. Li, D. Peyrade, M. Natali, Y. Chen, U. Ebels, L.D. Buda, K. Ounadjela *Flux closure structures in cobalt rings* Phys. Rev. Lett. **86**, 1102 (2001).
- [**Liu2012**] L. Liu, C.-F. Pai, Y. Li, H. W. Tseng, D. C. Ralph, and R. A. Buhrman, *Spin-torque switching with the giant spin Hall effect of tantalum*, Science **336**, 555 (2012).
- [**Locatelli2014**] N. Locatelli, V. Cros and J. Grollier *Spin-torque building blocks* Nature Mater. **13**, 11 (2014).
- [**Manchon2008**] A. Manchon, S. Pizzini, J. Vogel, V. Uhlir, L. Lombard, C. Ducruet, S. Auffret, B. Rodmacq, B. Dieny, M. Hochstrasser, and G. Panaccioneless *X-ray analysis of the magnetic influence of oxygen in Pt/Co/AlO_x/Pt/Co/AlO_x trilayers* J. Appl. Phys. **103**, 07A912 (2008).
- [**Mihai2011**] A.P. Mihai, F. Garcia Sanchez, L. Vila, A. Marty, L.D. Buda-Prejbeanu, J.C. Pillet, C. Beigné, D. Ravelosona, C. Mannequin, J-C. Toussaint, J.P. Attané *Stochastic domain-wall depinning under current in FePt spin valves and single layers* Phys. Rev. B **84**, 014411 (2011).
- [**Mikuszeit2015**] N. Mikuszeit, O. Boule, I. M. Miron, K. Garello, P. Gambardella, G. Gaudin and L. D. Buda-Prejbeanu, *Spin-orbit torque driven chiral magnetization reversal in ultrathin nanostructures* Phys. Rev. B **92**, 144424 (2015).
- [**Miron2011**] I. M. Miron, K. Garello, G. Gaudin, P.-J. Zermatten, M.V. Costache, S. Auffret, S. Bandiera, B. Rodmacq, A. Schuhl, and P. Gambardella, *Perpendicular switching of a single ferromagnetic layer induced by in-plane current injection*, Nature **476**, 189 (2011).
- [**Mistral2008**] Q. Mistral, M. van Kampen, G. Hrkac, Joo-Von Kim, T. Devolder, P. Crozat, C. Chappert, L. Lagae, T. Schrefl *Current-Driven Vortex Oscillations in Metallic Nanocontacts* Phys. Rev. Lett. **100**, 257201 (2008).
- [**Miwa2014**] S. Miwa, S. Ishibashi, H. Tomita, T. Nozaki, E. Tamura, K. Ando, N. Mizuochi, T. Saruya, H. Kubota, K. Yakushiji, T. Taniguchi, H. Imamura, A. Fukushima, S. Yuasa and Y. Suzuki, *Highly sensitive nanoscale spin-torque diode* Nature Mater. **13**, 50 (2014).
- [**Monso2002**] C S. Monso, B. Rodmacq, S. Auffret, G. Casali, F. Fettar, B. Gilles, B. Dieny, and P. Boyer *Crossover from in-plane to perpendicular anisotropy in Pt/CoFe/AlO_x sandwiches as a function of Al oxidation: a very accurate control of the oxidation of tunnel barriers* Appl. Phys. Lett. **80**, 4157 (2002).
- [**Moore2011**] I.M. Miron, T. Moore, H. Szabolcs, L.D. Buda-Prejbeanu, S. Auffret, B. Rodmacq, S. Pizzini, J. Vogel, M. Bonfim, A. Schuhl, G. Gaudin *Fast current-induced domain wall motion controlled by the Rashba effect* Nature Mater. **10**, 419 (2011).
- [**Muduli2010**] P. K. Muduli, Ye. Pogoryelov, S. Bonetti, G. Consolo, F. Mancoff, and J. Akerman, *Nonlinear frequency and amplitude modulation of a nanocontact-based spin-torque oscillator* Phys. Rev. B **81**, 140408 (2010).
- [**Natali2002**] M. Natali, I.L. Prejbeanu, A. Lebib, L.D. Buda, K. Ounadjela, Y. Chen *Magnetic vortex avalanches in arrays of interacting cobalt dots* Phys. Rev. Lett. **88**, 157203 (2002).
- [**Papusoi2009**] C. Papusoi, B. Delaet, B. Rodmacq, D. Houssameddine, J.-P. Michel, U. Ebels, R.C. Sousa, L.D. Buda-Prejbeanu, B. Dieny *100 ps precessional spin-transfer switching of a planar magnetic random access memory cell with perpendicular spin polarizer* Appl. Phys. Lett. **95**, 072506 (2009).

- [Pizzini2014]** S. Pizzini, J. Vogel, S. Rohart, L.D. Buda-Prejbeanu, E. Jué, O. Boulle, I.M. Miron, C.K. Safeer, S. Auffret, G. Gaudin, and A. Thiaville *Chirality-induced asymmetric magnetic nucleation in Pt/Co/AlO_x ultrathin microstructures* Phys. Rev. Lett. **113**, 047203 (2014)
- [Prejbeanu2000]** I.L. Prejbeanu, L.D. Buda, U. Ebels, K. Ounadjela *Observation of asymmetric Bloch walls in epitaxial Co films with strong in-plane uniaxial anisotropy* Appl. Phys. Lett. **77**, 3066 (2000).
- [Prejbeanu2002]** I.L. Prejbeanu, M. Viret, L.D. Buda, U. Ebels, K. Ounadjela *Magnetotransport measurements as a tool to probe the micromagnetic configuration in epitaxial Co wires* J. Magn. Magn. Mater. **240**, 27 (2002)
- [Pribiag2007]** V. S. Pribiag, I. N. Krivorotov, G. D. Fuchs, P. M. Braganca, O. Ozatay, J. C. Sankey, D. C. Ralph & R. A. Buhrman *Magnetic vortex oscillator driven by d.c. spin-polarized current* Nat. Phys. **3**, 498 (2007).
- [Purbawati2016]** A. Purbawati, F. Garcia-Sanchez, L.D. Buda-Prejbeanu, U. Ebels *Enhanced modulation rates via field modulation in spin torque nano-oscillators* submitted Appl. Phys. Lett. **102**, 122402 (2016).
- [PubawatiPhD]** A. Purbawati *Frequency modulation of spin torque nano-oscillators (STNOs) for wireless communication applications* University of Grenoble Alpes (2017).
- [Pufall2005]** M. R. Pufall, W. H. Rippard, S. Kaka, T. J. Silva, and S. E. Russek, *Frequency modulation of spin-transfer oscillators* Appl. Phys. Lett. **86**, 082506 (2005).
- [Quinsat2010]** M. Quinsat, D. Gusakova, J. F. Sierra, J.-P. Michel, D. Houssameddine, B. Delaet, M.-C. Cyrille, U. Ebels, B. Dieny, L. D. Buda-Prejbeanu, J.A. Katine, D. Maury, A. Zeltser, M. Prigent, J.-C. Nallatamby, R. Sommet *Amplitude and Phase Noise of MgO based Magnetic Tunnel Junction Oscillators* Appl. Phys. Lett. **97**, 182507 (2010).
- [Quisant2014]** M. Quinsat, F. Garcia-Sanchez, A. S. Jenkins, A. Zeltser, J. A. Katine, A. N. Slavin, L. D. Buda-Prejbeanu, B. Dieny, M.-C. Cyrille, U. Ebels *Modulation bandwidth of spin torque oscillators under current modulation* Appl. Phys. Lett. **105**, 152401 (2014).
- [Rippard2005]** W. H. Rippard, M. R. Pufall, S. Kaka, T. J. Silva, S. E. Russek, and J. A. Katine, *Injection locking and phase control of spin transfer nano-oscillators* Phys. Rev. Lett **95**, 067203 (2005).
- [Rodmacq2003]** B. Rodmacq, S. Auffret, B. Dieny, S. Monso, and P. Boyer *Crossovers from in-plane to perpendicular anisotropy in magnetic tunnel junctions as a function of the barrier degree of oxidation* J. Appl. Phys. **93**, 7513 (2003).
- [Romera2015]** M. Romera, E. Montebancho F. Garcia-Sanchez, B. Delaët, L. D. Buda-Prejbeanu and U. Ebels *Non-linear mode interaction between spin torque driven and damped modes in spin torque nano-oscillator* Appl. Phys. Lett. **106**, 192405 (2015).
- [Romera2016]** M. Romera, B. Lacoste, U. Ebels, L. D. Buda-Prejbeanu *Spin torque driven dynamics of a coupled two layer structure: interplay between conservative and dissipative coupling* Phys. Rev. B **94**, 094432 (2016)
- [Ryu2013]** K. Ryu, L. Thomas, S. Yang, and S. Parkin *Chiral spin torque at magnetic domain walls* Nat. Nanotechnol. **8**, 527 (2013).
- [Safeer2015]** C.K. Safeer, E. Jué, A. Lopez, L.D. Buda-Prejbeanu, S. Auffret, S. Pizzini, O. Boulle, I.M. Miron, G. Gaudin *Spin-orbit torque magnetization switching controlled by geometry* Nature Nanotechnology **11**, 143 (2015).
- [Sani2013]** S. Sani, J. Persson, S.M. Mohseni, Y. Pogoryelov, P.K. Muduli, A. Eklund, G. Malm, M. Kall, A. Dmitriev & J. Åkerman, *Mutually synchronized bottom-up multi-nanocontact spin-torque oscillators* Nature Communications **4**, 2731 (2013).
- [Slavin2009]** A. Slavin and V. S. Tiberkevich, *Nonlinear Auto-Oscillator Theory of Microwave Generation by Spin-Polarized Current*, IEEE Trans. Magn. **45**, 1875 (2009).

- [**Slonczewski1996**] J. C. Slonczewski, *Current-driven excitation of magnetic multilayers*, J. Magn. Magn. Mater. **159**, L1 (1996).
- [**Stoner 1948**] E. C. Stoner and E. P. Wohlfarth, *A mechanism of magnetic hysteresis in heterogeneous alloys*, Philosophical Transactions of the Royal Society of London. Series A, Mathematical and Physical Sciences **240**, 599 (1948).
- [**Strelkov2017**] N. Strelkov, A. Timofeev, R. Sousa, M. Chshiev, L. D. Buda-Prejbeanu and B. Dieny *Stability phase diagram of perpendicular magnetic tunnel junction in non-collinear geometry* Phys. Rev B **95**, 184409 (2017).
- [**Tao2008**] C.Tao, P. Teemu, T. Esa, H. Tenhunen, *RF transceiver circuit technology based wireless interconnects for Inter- and Intra-chip communication system*, 10th Electronics Packaging Technology Conference, 1409 (2008).
- [**Tiberkevich2008**] V. S Tiberkevich and A. N. Slavin, J.-V. Kim, *Microwave power generated by a spin transfer oscillator in the presence of noise*, IEEE Trans. Magn. **44**, 1916 (2008).
- [**Thiaville2005**] A. Thiaville, Y. Nakatani, J. Miltat, and Y. Suzuki, *Micromagnetic understanding of current-driven domain wall motion in patterned nanowires*, Europhys. Lett. **69**, 990 (2005).
- [**Thiaville2012**] A. Thiaville, S. Rohart, E. Jué, V. Cros, and A. Fert, *Dynamics of Dzyaloshinskii domain walls in ultrathin magnetic films* Europhys. Lett. **100**, 57 002 (2012).
- [**Timopheev2015**] A. A. Timopheev, R. Sousa, M. Chshiev, L. D. Buda-Prejbeanu, and B. Dieny *Respective influence of in-plane and out-of-plane spin-transfer torques in magnetization switching of perpendicular magnetic tunnel junctions* Phys. Rev. B **92**, 104430 (2015).
- [**VayssetPhD**] A. Vaysset *Micromagnetic modelling of spin transfer driven magnetization dynamics in nanopillars* University of Grenoble (2013).
- [**Vaysset2011**] A. Vaysset, C. Papisoi, L. D. Buda-Prejbeanu, S. Bandiera, M.M. Marins de Castro, Y. Dahmane, J.C. Toussaint, U. Ebels, B.Rodmacq, S. Auffret, R. Sousa, L.Vila, and B. Dieny *Improved coherence of ultrafast spin-transfer-driven precessional switching with synthetic antiferromagnet perpendicular polarizer* Appl. Phys. Lett. **98** (1) 242511 (2011).
- [**Urazhdin2010**] S. Urazhdin, V. S. Tiberkevich, A. N. Slavin, *Parametric Excitation of a Magnetic Nanocontact by a Microwave Field* Phys. Rev. Lett. **105**, 237204 (2010).
- [**Vincent2015**] A.F. Vincent, J. Larroque, N. Locatelli, N. Ben Romdhane, O. Bichler, C. Gamrat, W. S. Zhao, J. O. Klein, S. Galdin-Retailleau, D. Querlioz *Spin-transfer torque magnetic memory as a stochastic memristive synapse for neuromorphic systems*. IEEE Trans Biomed Circuits Syst. **9**, 16 (2015).
- [**Watson2001**] B. Watson, *FSK: Signals and Demodulation* (WJ Communications, San Jose, CA,(2001).
- [**Weiss1907**] P. Weiss, *L'hypothèse du champ moléculaire et la propriété ferromagnétique*, J. Phys. **6**, 661 (1907).
- [**Zhu2008**] J.G.Zhu, X. Zhu, Y.Tang, *Microwave Assisted Magnetic Recording*, IEEE Trans.Magn. **44**, 125 (2008).
- [**μMAG**] <http://www.ctcms.nist.gov/~rdm/toc.html>
- [**US6532164B2**] O. Redon, B. Dieny, and B. Rodmacq, *Magnetic spin polarization and magnetization rotation device with memory and writing process, using such a device* (2003).
- [**US8063709B2**] I. Firastrau, U. Ebels, B. Dieny *Spin-transfer torque oscillator* (2007).